

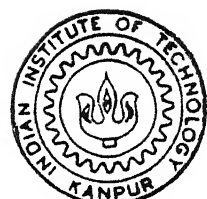
# IMAGE PROCESSING APPLICATIONS IN PHOTOELASTIC ANALYSIS

by

**KELKAR ASHISH ANAND**

ME  
1994  
M  
ANA  
IMA

TH  
me/1994/m  
R  
K 279 i



DEPARTMENT OF MECHANICAL ENGINEERING  
INDIAN INSTITUTE OF TECHNOLOGY KANPUR

February 1994

## CERTIFICATE

This is to certify that the thesis entitled, " IMAGE PROCESSING APPLICATIONS IN PHOTOLELASTIC ANALYSIS " by Kelkar Ashish Anand is a record of the work carried out under my supervision and has not been submitted elsewhere for a degree.



28/2/94

(K.Ramesh)

Asst. Professor

Mechanical Engg. Dept.

Indian Institute of Technology

Kanpur - 208016

TH  
620-112-05  
K 2002

25 MAY 1994 /ME  
REGISTRATION  
\_\_\_\_\_  
See No. A. 117553

ME - 1994 - M - ANA - IMA

## ACKNOWLEDGEMENTS

I wish to express my deep sense of gratitude and indebtedness towards Dr K.Ramesh for their inspiring guidance, invaluable suggestions and constructive criticism. He was always a constant source of encouragement throughout my thesis work.

I express my thanks to the ESA laboratory staff for extending their assistance in carrying out the experimental work.

I also extend my thanks to all my friends: Ashish Jadhav, Shevade, Shivaji, Bhise, and all my junior friends who made my stay at IITK a lively and pleasant one.

I fondly recollect the immense love and care by my parents and their inspiring support.

Kelkar Ashish Anand.

## LIST OF CONTENTS

Chapter	Page
Abstract .....	i
List of symbols .....	ii
List of figures .....	iii
1 INTRODUCTION .....	1
1.1 Introduction .....	1
1.2 Present Work .....	2
1.3 Thesis Layout .....	4
2 AUTOMATIC FRINGE RECOGNITION BY FRINGE TRACING.....	6
2.1 Introduction .....	6
2.2 System Configuration .....	6
2.3 Fringe skeleton extraction .....	8
2.3.1 Algorithm of Ramesh and Pramod .....	9
2.4 Need for fringe tracing algorithm .....	10
2.5 Simple fringe tracing algorithm .....	14
2.5.1 Performance of the images generated using computer graphics .....	15
2.5.2 Performance on the fringe skeleton identified using algorithm of Ramesh and Pramod .....	17
2.5.3 Performance for actual photoelastic fringe pattern images .....	17
2.6 Fringe tracing algorithm with direction scan .....	19
2.6.1 Performance of the images generated using computer graphics .....	19
2.6.2 Performance on the fringe skeleton	

identified using algorithm of Ramesh and Pramod .....	21
 2.7 Complex fringe tracing algorithm .....	22
2.7.1 Performance of the images generated using computer graphics .....	25
2.7.2 Performance on the fringe skeleton identified using algorithm of Ramesh and Pramod .....	25
2.7.3 Performance for actual photoelastic fringe pattern images .....	27
 2.8 Closure .....	27
 3. A NEW METHODOLOGY FOR AUTOMATING THE FRINGE ORDERING .....	32
3.1 Introduction .....	32
3.2 Fringe ordering in Photoelasticity .....	33
3.2.1 Guidelines to determine at which point shear is zero .....	33
3.2.2 Numbering of fringes in the general case .....	34
3.3 New methodology fo automation of fringe ordering .....	37
3.4 Use of two dimensional intensity plots for determining the stress gradient direction .....	38
3.5 Three dimensional intensity plots for various types of fringe fields .....	41
3.6 Automation of ordering for special class of fringe patterns .....	49
3.7 Automation of circular disc under diametral compression .....	50
3.8 Interactive fringe ordering for the mixed mode crack-tip fringe pattern .....	53
3.9 Closure .....	56
 4. EVALUATION OF STRESS INTENSITY FACTORS USING	

A HIGHER ORDER THEORY .....	58
4.1 Introduction .....	58
4.2 Developments in the description of the stress field equations in the neighborhood of a crack tip .....	59
4.2.1 Single Parameter Stress field Equation .....	59
4.2.2 Two Parameter Stress field Equation .....	60
4.2.3 Multi Parameter Stress field Equations .....	61
4.4 Mixed Mode Stress Field Equations .....	64
4.5 Developments in S.I.F evaluation methodology .....	65
4.6 Evaluation of Stress Intensity Factors using Least Square technique .....	68
4.7 Performance for a mode I crack Problem .....	72
4.8 Closure .....	77
5. EVALUATION OF STRESS FIELD PARAMETERS IN THE NEIGHBORHOOD OF A CRACK LOCATED IN THE TENSILE FILLET OF A SPUR GEAR .....	79
5.1 Introduction .....	79
5.2 Experimental Details .....	80
5.3 Selection of the crack location .....	82
5.4 Fringe Ordering .....	82
5.5 S.I.F. evaluation for the crack .....	87
5.5.1 Data Processing .....	87
5.6 Experimental Results .....	89
5.7 Closure .....	91
6. CONCLUSIONS AND SUGGESTIONS FOR FURTHER WORK .....	94
APPENDIX - 1 .....	97
APPENDIX - 2 .....	111
APPENDIX - 3 .....	112
REFERENCES .....	116

## ABSTRACT

Photoelasticity gives the information of  $(\sigma_1 - \sigma_2)$  in the form of fringes. Fringe ordering is one of the most difficult steps in processing the fringe patterns from any optical technique. Automated ordering of the fringes remains as one of the most challenging tasks even today. In this thesis, a new methodology is evolved for automatic fringe ordering using the technique of D.I.P. The new methodology has three steps (1) fringe skeletonisation (2) fringe tracing and (3) fringe gradient identification. Fringe skeleton is obtained using the algorithm of Ramesh and Pramod. Fringe tracing algorithm is newly developed and it identifies the pixels forming a continuous fringe. The algorithm uses a 3 X 3 mask and a tree structure for tracing out the fringes. Intensity variation over the fringe field is used to identify the fringe gradient direction. It is established in this thesis that the intensity variation over the fringe field is not trivial. Complete automation of the procedure has been implemented on a PC based system for a class of fringe patterns such as those occurring in circular disc under diametral compression. A semi-automatic procedure has been implemented for the fringe field occurring in the neighborhood of a crack.

Most of the practical structures of engineering importance have finite dimensions and the cracks in them may be located in zones of stress concentration and the cracks may be large enough so that the crack-tip may be closer to a boundary. Multi parameter stress field equations are needed to evaluate the stress field. Among the multi-parameter stress field equations, the equations proposed by Atluri and Kobayashi are the simplest. Several typographical errors in the reported equations are corrected in this thesis. Using these equations and following the methodology of Sanford, an overdeterministic least square method is developed to extract the stress field parameters from the isochromatic fringes. The application of this methodology to a practical problem of the mixed mode analysis of a crack at the tensile fillet of a spur gear is discussed. Results show that proper choice of the number of parameters can model the stress field in the vicinity, as well as the far field, accurately.

## LIST OF SYMBOLS

$x, y, z$	Cartesian co-ordinates.
$\theta_x, \theta_y, \theta_z$	Angle of rotation about the X, Y and Z axes respectively.
$F_\sigma$	Material fringe constant.
$t$	Model thickness.
$K_I, K_{II}$	Mode I and Mode II Stress Intensity Factors.
$\sigma_x, \sigma_y, \tau_{xy}$	Rectangular stress components.
$\sigma_1, \sigma_2$	Principal Stress components.
$\sigma_{\infty}$	Far field stress term.
$A_I$	Mode I S.I.F parameters from the Atluri and Kobayashi series solution..
$A_{II}$	Mode II S.I.F parameters from the Atluri and Kobayashi series solution.
$[g]$	Matrix containing the error in fringe order.
$[b]$	Matrix containing partial derivatives of the "g" function with respect to the respective parameters.
$[\Delta A]$	Matrix containing the delta values of the parameters.

## LIST OF FIGURES

	Page
Fig. 2.1 PC based Image Processing System.	7
Fig. 2.2 Algorithm of Ramesh and Pramod for fringe thinning.	11
Fig. 2.3 Fringe skeleton extracted by algorithm of Ramesh and Pramod superimposed on the test image.	13
Fig. 2.4 Hierarchy of search directions for the 3 X 3 mask.	
Fig. 2.5 Performance of a 3 X 3 mask for image generated using computer graphics.	16
Fig. 2.6 Performance of a 3 X 3 mask for a pair of intersecting lines.	18
Fig. 2.7 Performance of a 3 X 3 mask with direction scan for image generated using computer graphics.	20
Fig. 2.8 Performance of a 3 X 3 mask with direction scan for a pair of intersecting lines.	22
Fig. 2.9 Performance of a 3 X 3 mask with direction scan for the case of the interlaced pixels.	23
Fig. 2.10 Working of a complex fringe tracing algorithm for a tree image.	26
Fig. 2.11 Comparative performance of the 3 algorithms for actual photoelastic fringe pattern skeleton.	29
Fig. 2.12 Magnified image of a discontinuity in the fringe pixels.	30

Fig. 3.1	Appearance of zero-order isochromatics in the neighborhood of square corners.	36
Fig. 3.2	Isochromatic fringes in a ring under diametral compression illustrating the presence of peaks, valleys, saddle and isotropic points.	36
Fig. 3.3	Variation in intensity along various scan directions for the fringe pattern of a circular disk under diametral compression.	39
Fig. 3.4	Variation in intensity for a crack tip fringe pattern.	39
Fig. 3.5	Variation in intensity for a crack tip fringe pattern.	40
Fig. 3.6	Variation in intensity along various scan lines for an annular ring under diametral compression.	42
Fig. 3.7	Magnified view of the intensity variation across a sink point in the annular ring.	42
Fig. 3.9	3-dimensional plot of variation in intensity over a circular disk under diametral compression.	45
Fig. 3.10	Magnified view of the high stress gradient zone at the contact point for the circular disk under diametral compression	45
Fig. 3.11	3-dimensional intensity profile for the crack tip fringe pattern.	46
Fig. 3.12	3-dimensional intensity profile for the crack tip fringe pattern with a frontal loop.	46
Fig. 3.13	3-dimensional intensity profile for annular ring under diametral compression.	47

Fig. 3.14 3-dimensional plot of the magnified view of the sink point.	47
Fig. 3.15 3-dimensional plot of the magnified view of the saddle point.	48
Fig. 3.16 Selection of scan path for the circular disk under diametral compression.	51
Fig. 3.17 Selection of scan path for the crack tip fringe pattern.	54
Fig. 4.1. Isochromatic fringe pattern observed in an Modified Compact Tension specimen. Isochromatics cross the X axis for larger a/w values.	62
Fig. 4.2 Singular non singular and far field region around a crack tip.	67
Fig. 4.3 Isochromatic fringe pattern obtained for an annular ring subjected to internal pressure with cracks emanating from the outer boundary.	73
Fig. 4.4 Reconstructed fringe pattern for the mode I problem using different number of terms of the Atluri's stress field series solution.	75
Fig. 4.5 Graph of cumulative percentage error v/s number of terms of the series solution.	76
Fig. 4.6 Graph showing variation of mode I parameters for series solution using different number of terms.	78
Fig. 5.1.a Loading frame Setup.	81
Fig. 5.1.b Closeup view of the gear loading frame.	81

Fig. 5.2 Isochromatic Fringe pattern of a gear tooth under  
under monochromatic and white  
light.

83

Fig. 5.3 Isochromatic fringe patterns of the spur gear  
tooth with a crack at its tensile fillet, for  
increasing load, under monochromatic and white  
light source.

86

Fig. 5.4 Reconstructed fringe pattern with the data points  
echoed back for the leastsquare analysis using  
increasing number of terms of the series solution.

90

## CHAPTER 1

### INTRODUCTION

#### 1.1 Introduction

When a ray of polarised light is incident on the surface of a model made of birefringent material, it splits up into two components, one of which obeys the Snell's law the other (extraordinary component) violates the Snell's law and moves at a slower speed. This leads to a phase lag between the two rays as they emerge out of the model, creating a retardation pattern.

It has been found out experimentally that this phase lag is directly proportional to the difference of the principal stress and the stress-optic law relates this as,

$$\frac{N F_\sigma}{t} = (\sigma_1 - \sigma_2) \quad (1.1)$$

where  $F_\sigma$  (N/mm/fringe) is the material fringe constant, N is the fringe order and t is the model thickness. The contours corresponding to  $(\sigma_1 - \sigma_2)$  are known as isochromatics.

If a plane polarised light is used, then one observes two sets of contours namely isochromatics (contours of maximum shear stress) and isoclinics (contours of principal stress orientation). If a circularly polarised light is used, then one observes only isochromatics.

An experiment in photoelasticity involves the following steps :

1. Image acquisition.
2. Fringe extraction and ordering
3. Data collection and its analysis.

The collection of data involves the determination of the fringe order and the positional coordinates of various data points from the fringe field.

## 1.2 Present work

One of the main advantages of a technique like Photoelasticity is that one gets the information related to the stress field rather than a point information as obtained in strain gauge. The instrumentation in strain gauge has developed to an extent that one can directly read the values from the meter as strains. On the other hand, one obtains the result in Photoelasticity in the form of fringes. Though the fringes must appear as lines theoretically, they appear as broad bands in view of the limited resolution of the recording medium. The breadth of the band is related to the local stress gradient.

In order to obtain quantitative information, one has to identify first the exact fringe location and then find the fringe order. With the development of Digital Image Processing, now sophisticated algorithms are available to extract the fringe skeletons precisely.

Though the fringe skeleton can be extracted, there is no algorithm available for automatic fringe ordering. Fringe ordering is one of the most difficult steps in processing the fringe patterns from any optical technique. One needs prior knowledge to do this and automated ordering of the fringes remains as one of the most challenging tasks even today.

In this thesis, a new methodology is evolved for automating the fringe ordering in photoelastic experiment. Using the fringe thinning algorithm by Ramesh and Pramod [1] the fringe skeleton is extracted. An algorithm is developed and implemented for fringe recognition and tracing. Complete automation of the procedure is achieved for certain class of problems.

The present work is a step towards complete automation for a Photoelastic experiment. A comprehensive software can be developed as an extension which will be able to interpret the fringe patterns and give the results directly in the form of stresses for the photoelastic experiment.

This will make the photoelastic technique accessible to a much broader spectrum of users. Combined with the inherent advantages of photoelasticity, i.e. the availability of the whole field information, this technique would therefore lead to wider application of photoelasticity in the industry.

The use of Fracture Mechanics principles to design structures is gaining importance in the recent years and one of the important parameter to be evaluated is the Stress Intensity Factor (S.I.F). The S.I.F can be evaluated by analysing the isochromatic fringe field in the neighborhood of the crack-tip. One must use appropriate equations, which closely model the stress field for data reduction.

Most of the practical structures of engineering importance have finite dimensions and the cracks in them may be located in zones of stress concentration and the cracks may be large enough so that the crack-tip may be closer to a boundary. The basic stress field equations of fracture mechanics are developed for cracks lying in a body of infinite dimensions(i.e., the crack-tips are far away from the boundaries) subjected to an uniform stress field. When these equations are attempted to be applied for solving real life problems, one gets erroneous results. The recognition of this fact has lead the researchers to account for this effect and multi-parameter stress field equations have been developed in the past two decades.

Among the various stress field equations, the use of equations proposed by Atluri and Kobayashi [2] is selected for their compactness and ease of programming. Though the equations proposed by Atluri and Kobayashi are recent ones and elegant to use, unfortunately there were several typographical errors in the reported equation. The errors were identified when the reconstructed fringe field did not have symmetry in the case of Mode II. These errors are corrected in the present thesis. Following the lines of Sanford [3] an overdeterministic scheme is evolved to solve for the mixed mode parameters. The program is validated by solving a Mode-I crack problem. Use of the above methodology for solving the problem of finding the stress field in the neighborhood of a crack in the tensile fillet of a spur gear is discussed towards the end.

### 1.3 Thesis layout

Chapter 2 deals with the new methodology for automatically tracing the fringes. The fringe thinning algorithm scans the image along particular directions and marks all the fringe points, however it cannot recognize a particular fringe as a continuous one since, in the computer representation, the fringes are just a group of points without any particular ordering. The first step towards automatic fringe ordering lies in the computer recognition of the fringes. Starting with a simple 3 X 3 mask, its performance is evaluated for various test images and also for an actual fringe pattern. Improvements are made in this and finally a complex fringe tracing algorithm is presented which improves upon the shortcomings of the previous algorithms.

Various aspects involved in the fringe ordering procedure in photoelasticity are discussed in Chapter 3. The importance of the intensity variation in the fringe field to identify fringe gradient direction in photoelasticity is established. An algorithm is presented for complete automation of the fringe ordering procedure for a circular disk under diametral compression and an interactive approach is proposed for automation of the fringe ordering for the mixed mode crack problem.

Chapter 4 deals with the least square procedure for the analysis of the data collected to evaluate the crack-tip stress field parameters from the photoelastic experiment. The need for considering the higher order terms to model the stress field in the neighborhood of long cracks is established. Using the Atluri's series solution [2], an example problem of Mode I crack is analysed and the fringe field is reconstructed using computer graphics for comparison with the experimental patterns. The typographical errors of the reported equations in the original reference[2] are also brought out.

In Chapter 5 application of the above procedure to mixed mode problem is discussed. The problem of evaluating the stress field parameters in the neighborhood of a crack at the tensile fillet of a spur gear is studied.

One of the major tasks completed in the course of the present investigation is the conversion of various software modules developed around Professional Image Processing ( PIP ) system over the last four years to the newly acquired MVP-AT system. Software modules for image acquisition, image filtering and cleaning, fringe skeletonisation using the algorithm of Ramesh and Pramod [1] have been implemented. Appendix section lists out the prominent modifications required for this.

## CHAPTER 2

### AUTOMATED FRINGE RECOGNITION BY FRINGE TRACING

#### 2.1 Introduction

The photoelastic fringes generally appear in the form of bands and not as thin lines. Identification of actual fringe skeleton is an important task. The accuracy in the data collection is subject to human judgment in the conventional analysis.

However, with the development of Digital Image Processing, now sophisticated algorithms are available to extract the fringe skeletons precisely. The fringe thinning algorithm scans the image along particular directions and marks all the fringe points, however it cannot recognize a particular fringe as a continuous one since, in the computer representation, the fringes are just a group of points without any particular ordering. The first step towards automatic fringe ordering lies in the fringe recognition algorithm. In this chapter, a fringe tracing algorithm is proposed and its performance is accessed for various test images and actual photoelastic fringe patterns.

#### 2.2 System Configuration

The image processing system used consists of a CCD camera (TM 560 PULNIX) that has a pixel resolution of 512 X 512 pixels and digitizes the image at video rates.

The camera is connected to a PC-386 based colour image-processing system equipped with an image processing card (MVP-AT, Matrox corporation) connected to a high resolution video monitor as shown in Fig.2.1 The system has in addition to PC memory, four frame buffers, each of 512 X 512 pixels X 8 bits, to store the image being processed and the intermediate results.

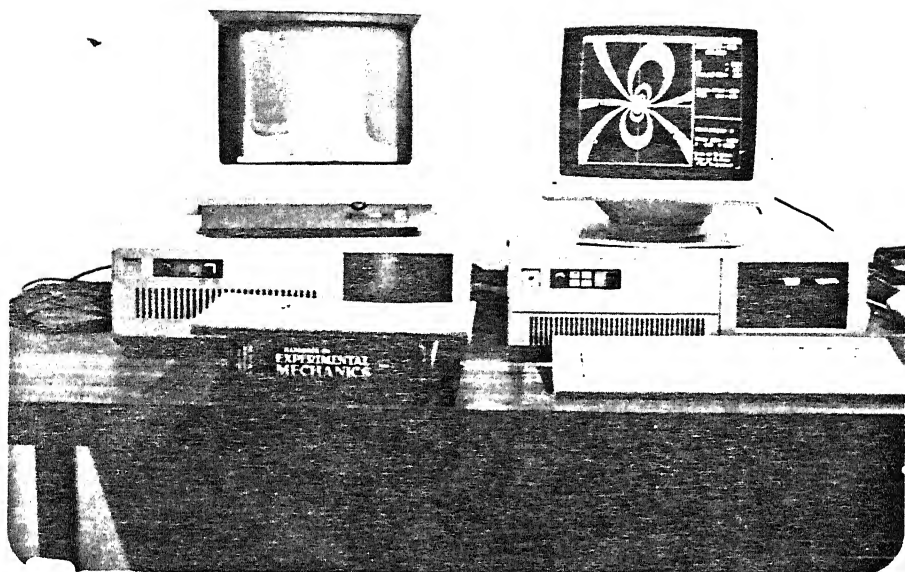


**Fig. 2.1 PC based Image Processing System.**

### 2.3 Fringe Skeleton Extraction

In Digital Image Processing (D.I.P), the image is identified as an assembly of picture elements abbreviated as pixels. Depending on the intensity of light transmitted/reflected each pixel is assigned a number between 0 (pitch dark) and 255 (pure white). Now the image is available as a matrix of numbers which can be handled by a digital computer for further processing. Due to the nature of formation of fringes, the intensity of pixels in the fringe band does not remain constant but there exists a variation. Though the variation is not resolvable to a fine degree by a human eye, the present day CCD cameras can easily recognise it and quantise it for further processing.

The various DIP algorithms reported in the literature can be classified into two categories[4]. In the first category the fringe field is identified as a binary image and the fringe skeletons are obtained using algorithms that were primarily developed for optical character recognition. The algorithms of Müller and Saackel [5], Seguchi et.al. [6] and the recent one of Chen and Taylor [7] come under this category. In the other category, intensity variation within a fringe is used in one way or other in devising algorithms for fringe skeleton determination. The algorithms of Yatagai et.al. [4], Gillies [9], Umezaki et.al. [10], and Ramesh and Pramod [1] come under this category.

Utilisation of intensity variation, within a fringe, to detect fringe skeleton was first reported by Yatagai et.al. [8]. They were essentially concerned with the detection of fringe maxima (in most systems 0 is pitch black and 255 is pure white) to identify fringe skeletons from the bright bands. Umezaki et.al. [10] reported another algorithm for fringe skeleton detection using fringe minima as a criterion and concentrated in extracting fringe skeletons from dark bands.

### 2.3.1 Algorithm of Ramesh and Pramod [1]

Ramesh et.al. [11] showed for the first time that fringe edge detection followed by fringe skeleton identification using a minimum intensity criterion greatly minimises the noise reported in other algorithms.

However, the algorithm is limited to processing either horizontal or vertical fringes. Ramesh and Pramod [1] improved the earlier algorithm of Ramesh et.al [11] to process fringes of any orientation. In this algorithm, fringe edges are detected first and any further detailed computation is done only within the fringe band. It is shown in reference 11 that a very simple method of global thresholding is sufficient to detect fringe edges. If there is intensity variation in the image, one can use either dynamic thresholding[11] or divide the image into convenient segments(tiles) and use appropriate global threshold for each of the segments[11] to detect fringe edges.

Once the edges are determined, the image is scanned row-wise (0 deg. scan), diagonal-wise (45 deg. scan), column-wise (90 deg. scan) and cross-diagonal-wise (135 deg. scan). For each scan direction, the pixel having minimum intensity between the edges is selected as skeleton point. There may be situations wherein more than one pixel may have the same minimum intensity forming a band. If the band is of odd number of pixels, the center pixel is identified as the skeleton point and if it is of even number of pixels then two pixels at the center are identified. Thus at the end of initial processing, one gets four images of fringe skeletons corresponding to each scan direction. It, is to be noted that these scans are done globally and are not for each individual pixel as it is done by Yatagai et.al.[8] and Umezaki et.al.[10]. Noise points which are scan direction dependent, appear in each of the above scans.

Further, the fringe skeleton is not continuous in one scan. The discontinuity is also scan direction dependent.

A novel approach with definite steps to retain which of the detected minimum intensity points as fringe points is reported by Ramesh and Pramod [1] and the scheme is shown in Fig.2.2.

1. The 0 deg. and 90 deg. scans are logically 'OR'ed to get a complete fringe skeleton. This image contains the noise due to both 0 deg. and 90 deg. scans.
2. The 45 deg. and 135 deg. scans are logically 'OR'ed to get a complete fringe skeleton. This image contains the noise due to both 45 deg. and 135 deg. scans.
3. Results of steps 1 and 2 are logically 'AND'ed to get the complete fringe skeleton free of noise.

The procedure of identification of minimum intensity point in the above algorithm is developed with the premise that within a fringe, only one minimum intensity band can occur. The minimum intensity point is located directly without any intermediate storing of pixel values. However situations occur, particularly in the case of a saddle point, there can be more than one minimum intensity band along a scan direction within the fringe. In the improved version of the algorithm by Ramesh and Rajeev Singh [12] the gray level values along the scan direction within the fringe edges are first stored. The fringe skeleton points are then identified by using the minimum intensity criteria. By this approach, fringe skeleton points would not be missed from any number of bands. The above algorithm was originally implemented on the PIP system. One of the major tasks completed in the course of present work was to translate the program code from the PIP to the MVP-AT. The details are given in Appendix-1.

#### 2.4. Need for a fringe tracing algorithm

The fringe thinning algorithm based on the local minimum intensity point identification gives a fringe skeleton free of noise and discontinuities. The fringe skeleton has a thickness upto two pixels and has the intensity value of 250 i.e. (pure white). The skeleton is superimposed on the original image for clarity.

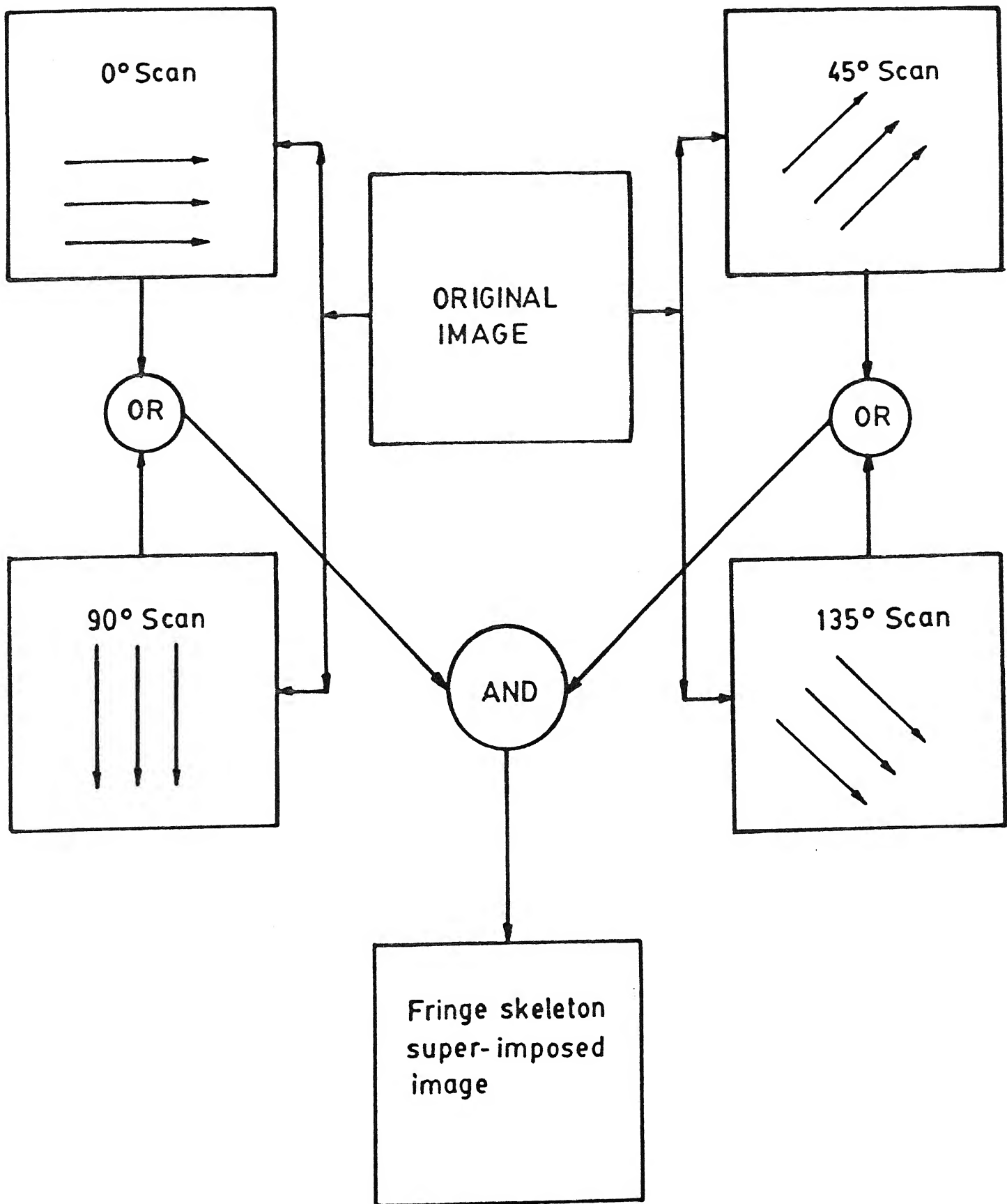


Fig. 2.2 Algorithm of Ramesh and Pramod for fringe thinning.

The fringe tracing algorithm has to perform the task of identifying pixels forming a particular fringe. The basic methodology is, if a fringe point is selected, the algorithm must be in a position to identify all contiguous points forming a fringe. To achieve this, an algorithm is proposed which basically uses a 3 X 3 mask to search for the next fringe point. The intensity of the identified point is changed from 250 to some other value indicating the fringe order. For example 1 corresponds to fringe order 1, 2 corresponds to the fringe order 2 and so on. The performance of the algorithm is tested for various class of test images. Following three classes of images were used in the present investigation.

#### 1. Simple geometric shapes generated using computer graphics.

The methodology of image generation ensures continuous fringes of one pixel width. The images are selected to bring out the performance of the algorithm for all geometric properties of the fringes e.g. An ellipse is used to evaluate the performance for loops, the triangle and the rectangle are selected to test the performance for sharply bent fringes and a cross, to test the performance when the fringe has several branches a situation simulating a saddle point.

#### 2. Fringe skeletons extracted by the algorithm of Ramesh and Pramod [1] on test images.

The test image used for the purpose of present investigation is an image of concentric circles ( ellipse - visually ). Figure. 2.3 shows the fringe skeleton superimposed image. Though the final fringe skeleton is elliptic in nature, there is a difference between drawing an ellipse using the graphics utility and one extracted as a skeleton. The basic difference is brought out later in this chapter.

#### 3. Fringe skeleton extracted by the algorithm of Ramesh and Pramod [1] on actual experimental fringe pattern.

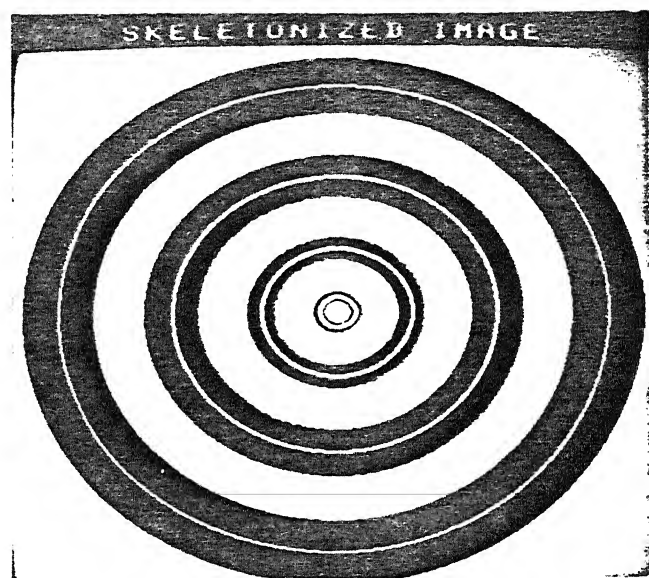


**Fig. 2.3 Fringe skeleton extracted by algorithm of Ramesh and Pramod superimposed on the test image.**

From analysing the results of the algorithm on the above class of images, the basic  $3 \times 3$  mask used is improved upon. In the following paragraphs the details of the simple algorithm initially used and its improvements culminating in a complex fringe tracing algorithm is presented.

## 2.5 Simple fringe tracing algorithm

This algorithm uses a  $(3 \times 3)$  mask as shown in Fig.2.4. The number represents the sequence in which the pixels are scanned from its local neighborhood for the fringe pixel. This mask has been selected giving priority to the pixels in the immediate neighborhood. The sequence of steps involved in tracing a fringe contour is summarised below.

1. Starting from a point  $P(x,y)$  on a fringe (fringe order  $N$ ), the algorithm searches for the presence of a fringe skeleton pixel (having intensity value equal to 250) in its immediate neighborhood in the order shown in Fig.2.4.
2. If such a point is located, then further search is stopped and the  $x$  and the  $y$  coordinates are set to the new values  $(x',y')$ .
3. The pixel intensity of the point  $P(x',y')$  is then changed from 250 to the intensity value numerically equal to the order of the fringe which can be recognized by the program.
4. The steps 1, 2 and 3 are repeated for the new pixel location  $P(x',y')$ .

These steps are repeated till the end of the fringe is reached which is indicated by the absence of a fringe point among any of the neighborhood pixels within the mask. Having completed scanning along a particular direction, the  $X$  and  $Y$  coordinates are set to their initial value and scanning is repeated in the other direction thus tracing out the remaining part of the fringe.

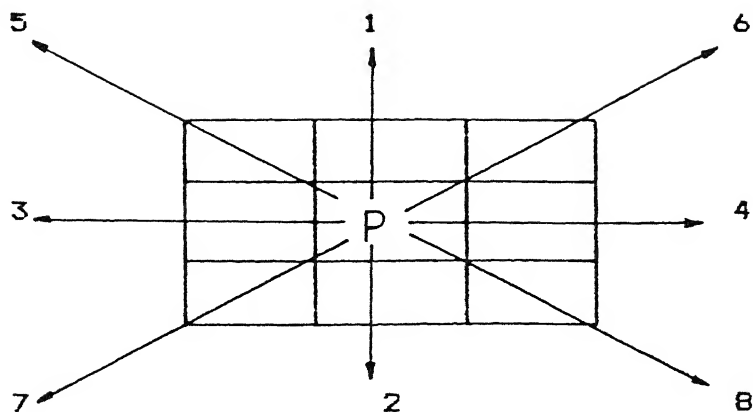


Fig. 2.4 Hierarchy of search directions for the  $3 \times 3$  mask.

### 2.5.1 Performance for the images generated using computer graphics

The mask performs satisfactorily for the rectangle. The mask is able to trace out the complete segments constituting the rectangle.

In the case of the triangle, when the mask reaches near the vertex pixel it recognizes two pixels as lying on the fringe as shown in Fig.2.5a.

The vertex pixel is skipped and the pixel on the next segment (direction 2) is selected as it has a priority over the direction 3, during the search operation Fig.2.5a.

The mask is then advanced to this pixel. In the present position, fringe pixels exists in its immediate neighborhood one along direction 5 and the other along direction 8 (Fig.2.5b). The pixel along direction 5 alone is identified by the algorithm in view of the hierarchy of search used in the mask. Hence, the mask moves along that direction. In this position, all the neighboring fringe pixels are marked as shown in Fig.2.5c. The search routine terminates.

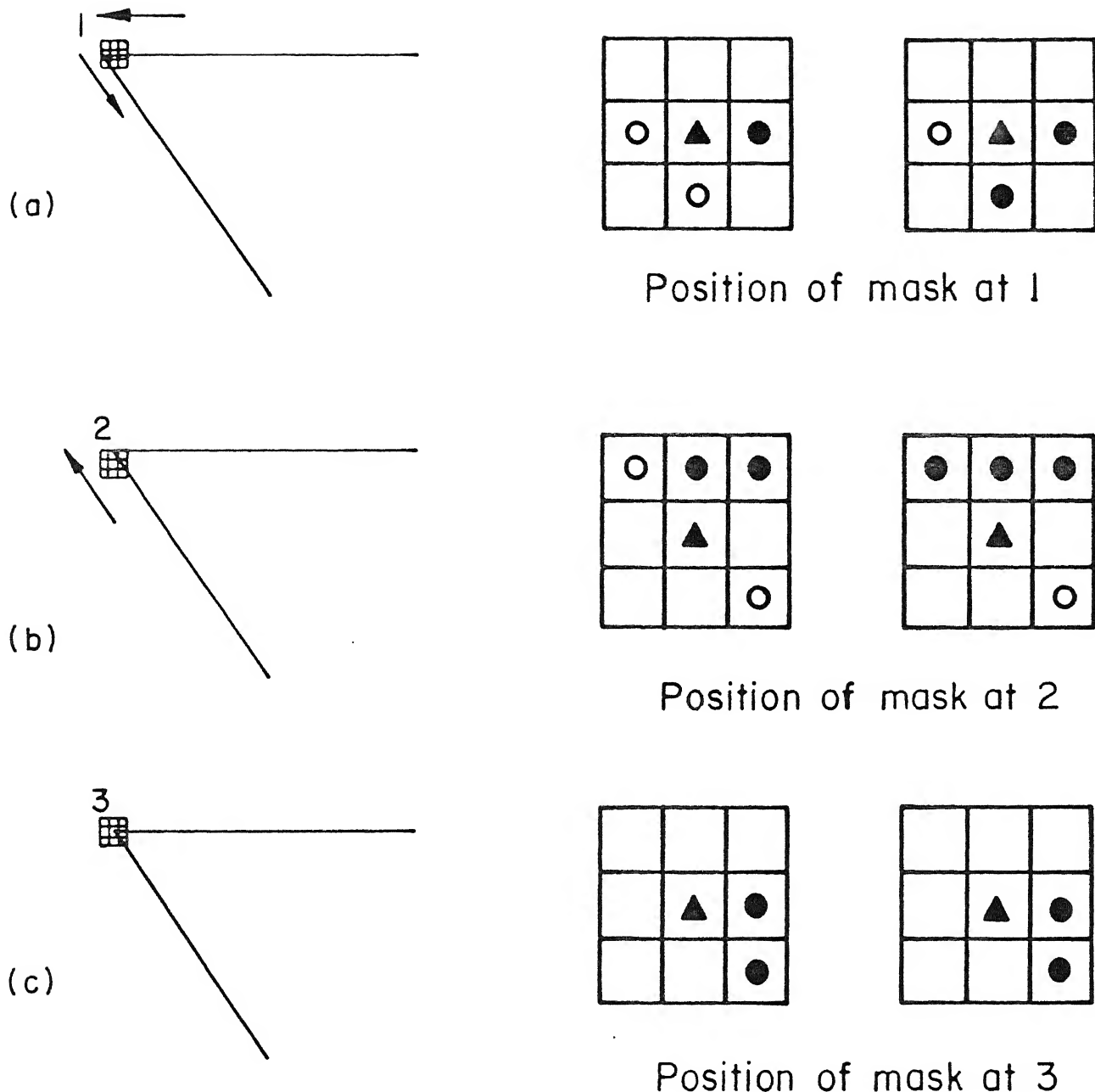


Fig. 2.5 Performance of a  $3 \times 3$  mask for image generated using computer graphics.

It can be seen that the mask is unable to trace out the whole fringe. If the mask is again setup at a point on the unmarked segment, then it traces out the remaining portion of the fringe. However, an approach like this makes the algorithm interactive rather than stand alone.

In the case of a theoretically generated ellipse the algorithm gives a satisfactory performance.

For a pair of intersecting lines, if initially a point is selected as shown in Fig.2.6a, the line is traced in accordance with the hierarchy set in the mask. On reaching the intersection point three fringe pixels exist along direction 6, 7 and 8 as shown in Fig.2.6b. The mask then moves only along direction 6 as shown in Fig.2.6c. Thus, deviating from the original segment. The portion AOC is traced out and the portion BOD remains unmarked.

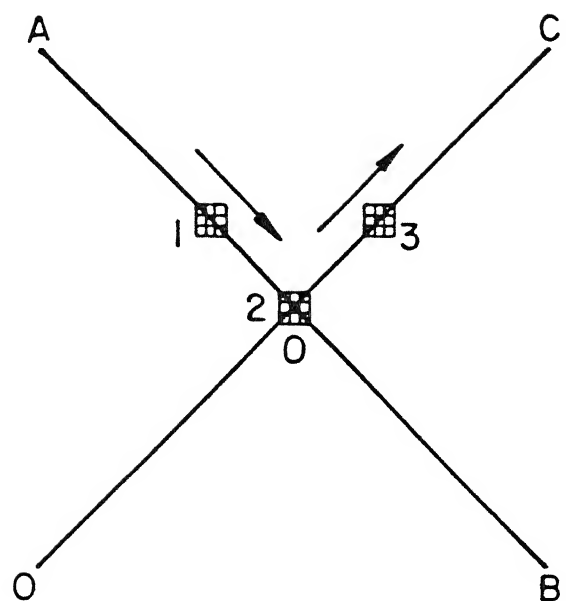
#### 2.5.2 Performance on fringe skeleton identified using the algorithm of Ramesh and Pramod [1]

The entire fringe is scanned and the overall performance of the algorithm is satisfactory.

#### 2.5.3 Performance for actual photoelastic fringe pattern images

The algorithm does not perform satisfactorily and is unable to trace out some fringes completely.

From the foregoing examples, it is seen that there are several situations wherein more than one fringe point pixel exists in the neighborhood. Ideally, all these fringe points need to be checked further. Some may be just noise points. If they are just noise points, a direction scan priority criteria may help in tracing the fringe. To achieve this, the direction of the fringe point for the previous pixel is to be stored and the existence of the next fringe point is to be checked along that direction first.



(a)

●		
	▲	
		○

Position of mask at 1

(b)

●		○
	▲	
○		○

Position of mask at 2

(c)

		○
	▲	
●		

●		
	▲	
●		

Position of mask at 3

Fig. 2.6 Performance of a  $3 \times 3$  mask for a pair of intersecting lines.

## 2.6 Fringe tracing algorithm with direction scan

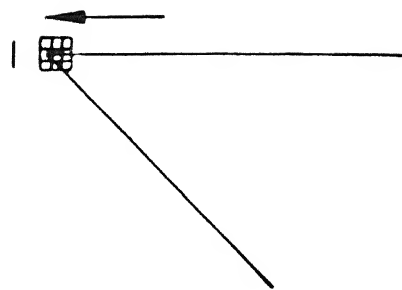
1. The (3 X 3) mask is set up at the initial point and the next fringe point location is determined and the point is marked.
2. The direction of the fringe point from the current coordinates is then stored.
3. The new coordinates are then set along this direction and the existence of a fringe point is then checked.
4. If the fringe point is not found along that direction, only then the mask is setup and the next fringe point and the new direction are determined, otherwise the search is continued in the same direction.

This algorithm works more efficiently in case of near linear fringes. The number of logical checks required, for such cases reduces from an average of four pixel point search to one pixel. Also, more priority is assigned for the previous scan direction rather than the priority for the positive Y direction which occurs in the mask.

### 2.6.1 Performance for the images generated using computer graphics

The algorithm performs well for the rectangle as well as the triangle. All the segments are traced out.

In the case of the acute angle (Fig.2.7a) the horizontal segment is traced out till the vertex point is reached. Though the fringe pixel is also found in direction 2, since the previous scan direction is 3, it gets priority and mask traces out the complete segment in that direction. The fringe point is then located along the direction 8 and the tracing continues as indicated in Fig.2.7b. Thus the drawback of the simple fringe tracing algorithm is overcome with this modification.

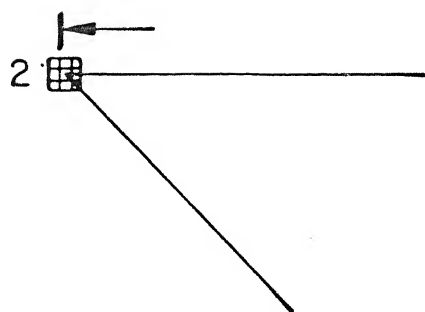


(a)

O	▲	●
	O	

●	▲	●
	O	

Position of mask at 1

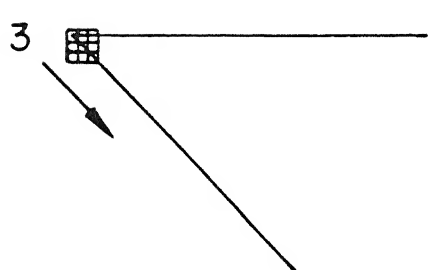


(b)

	▲	●
	O	

	▲	●
		●

Position of mask at 2



(c)

●	●	●
	▲	
	O	

●	●	●
	▲	
		●

Position of mask at 3

Fig. 2.7 Performance of a  $3 \times 3$  mask with direction scan  
for image generated using computer graphics.

The algorithm performs well in the case of the theoretically generated ellipse.

This algorithm gives a much better performance in cases of intersecting lines. As shown in Fig.2.8b, since priority is given to the previous direction (direction 5 in this case), the correct part of the segment is traced out and as the mask does not deviate from the required path. However, the line segment COD will not be traced and it requires improvement to enable it to scan and trace all the branches.

#### 2.6.2 Performance on fringe skeleton identified using the algorithm of Ramesh and Pramod [1]

The algorithm does not give a satisfactory performance with this image. The fringe is not traced out completely. This has been identified due to the problem of interlacing of pixels as shown in Fig.2.9.

A curved segment on the screen, observed under magnification shows the inclined segments like steps of a staircase. For a theoretically generated ellipse the best fit pixels are calculated corresponding to the position of the actual line segment. Hence they are represented by continuous (though staircase effect is evident), non interlaced pixels. At any point on the segment, only one fringe pixel exists in the neighborhood and the algorithm works satisfactorily.

However, in the case of the actual fringe skeleton extracted, there occur more than one pixel representing the curve occur. This is because the pixel positions are located purely on the basis of the minimum intensity criteria. This leads to the mask straying in the wrong direction and causes the failure of the algorithm. As shown in Fig.2.9, the algorithm using the direction scan moves along direction 8 till the fringe pixel 4. At this stage, the fringe pixels exist along directions 1 and 4, pixel 5.

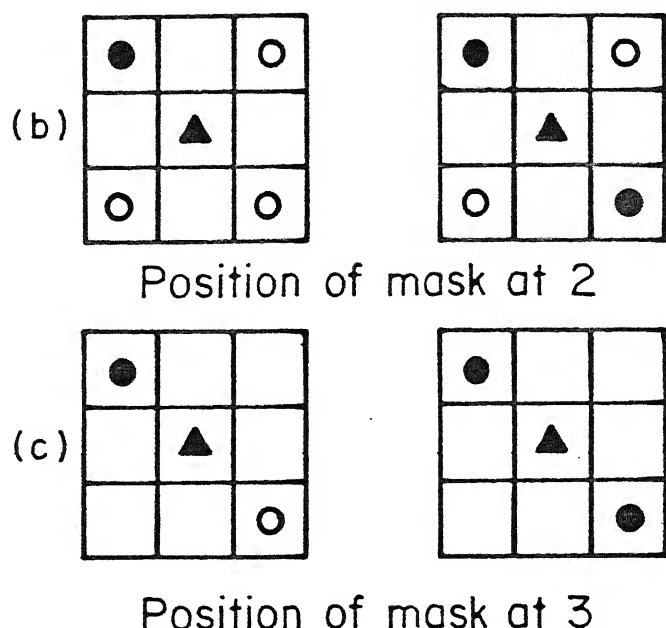
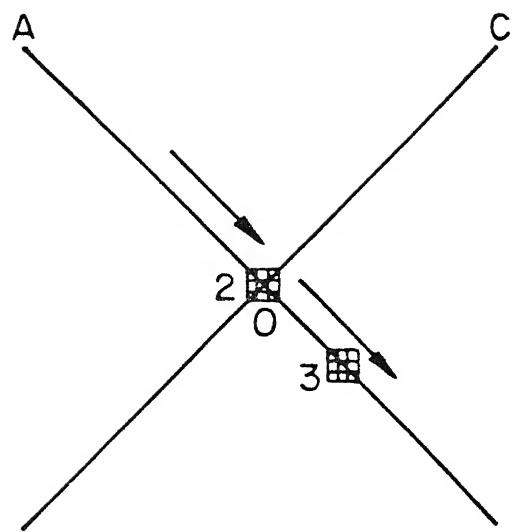
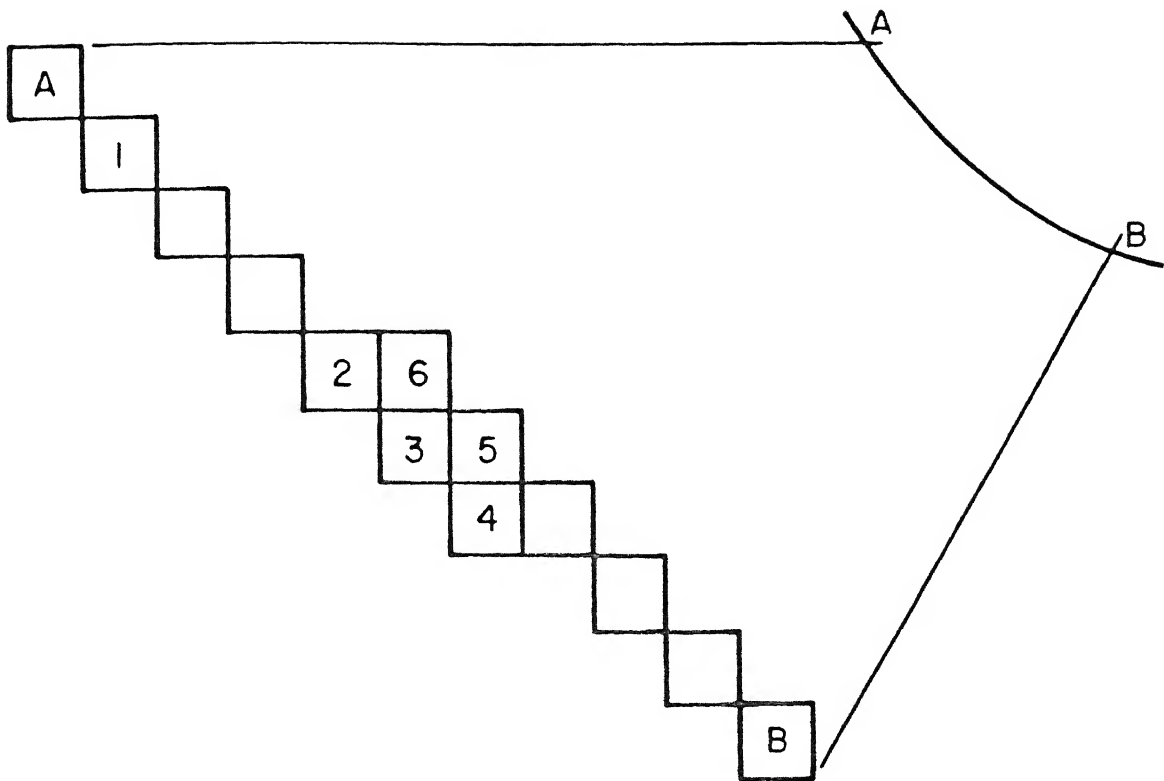


Fig. 2.8 Performance of a  $3 \times 3$  mask with direction scan on a pair of intersecting lines.



Actual magnified pixel representation of a curved segment on the screen

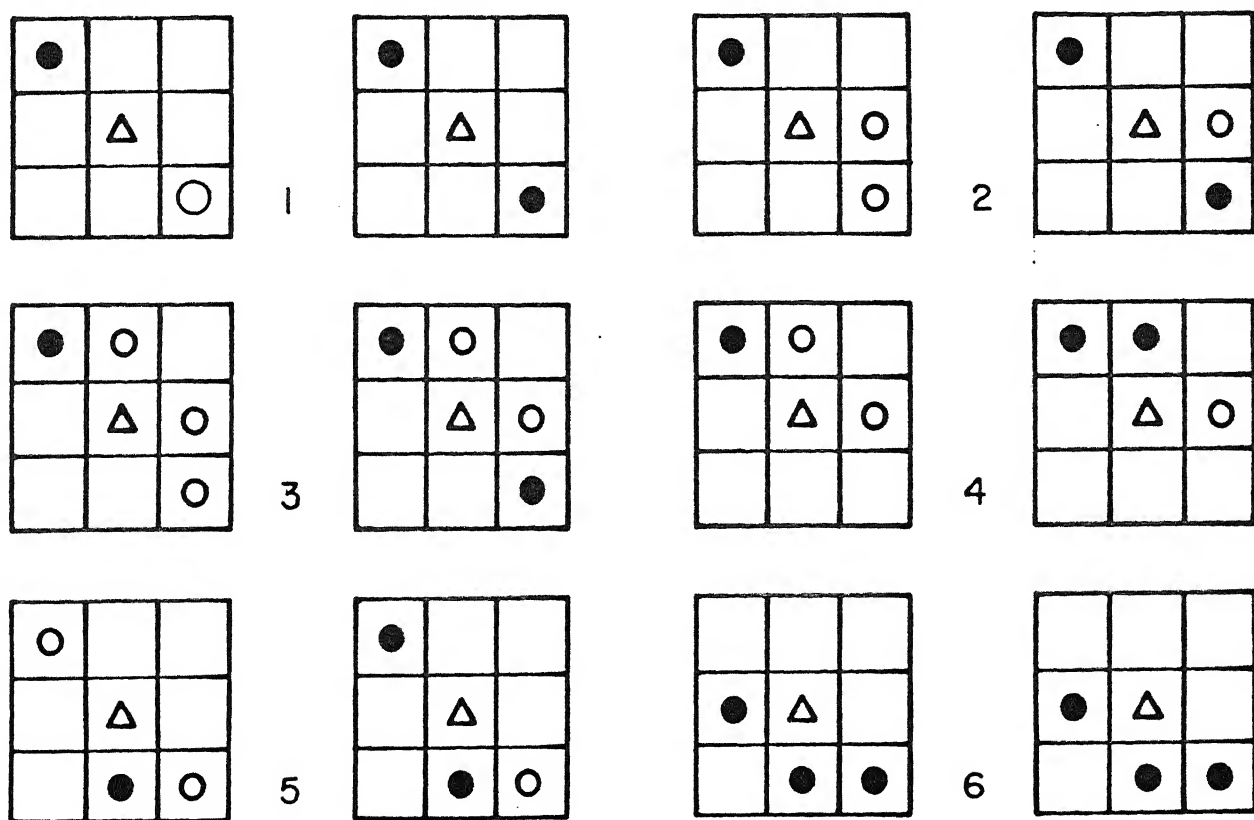


Fig.2.9 Performance of a  $3 \times 3$  mask with direction scan for the case of the interlaced pixels.

In the view of the basic hierarchy of the search the mask moves along direction 1 and traces back along the second line of the pixels i.e. pixel 6 and thus deviates from the intended path.

This problem of the mask straying from the expected path also occurs in the case of the actual photoelastic fringe pattern. However it performs better than the simple 3 X 3 mask.

The next algorithm corrects the defect caused due to interlacing of the fringe pixels and proposes a more generalized approach for fringe tracing.

#### **2.7 Complex fringe tracing Algorithm :**

1. This algorithm also uses a 3X3 mask, with a difference that every pixel in the mask is scanned before a decision is made as to which direction the search should proceed. In this way all the branch points on the fringe are determined.
2. If more than one fringe points are located within the mask, such points are stored to an array and the search continues in the direction as specified by the mask. Thus by the time the end point of the fringe is reached, all the branch nodes are stored in an array.
3. When the end point of the fringe is encountered, the last point on the array is read, and the mask is set at this point and that part of the fringe is now traced. On encountering any additional branch points, they are stored to the array and the procedure is repeated till all those parts of the fringe are traced out.
4. The count of the node points is decremented after the search is over. The mask is set at the previous branch point and the tracing continuous. Thus it can be seen that the branches are traced out in a reverse order i.e. the first node point being the last to be traced and so on.

### 2.7.1 Performance for the images generated using computer graphics

In order to test the correctness of implementation, a tree image as shown in Fig.2.10. is generated using the graphics utility. The tree has explicit multiple branches from its nodes. The interlaced curve representation is thus a subset of this class of images and the performance of the algorithm is expected to be same for the tree image and the multiple branch points in an actual image. The node points are actually the ones which determine the next trace direction.

The Fig.2.10 shows the performance of this algorithm for a tree structure. Starting from the lowermost branch, it reaches node 0 first , stores the coordinates on the array, then continues along one path and reaches node point 1 whose coordinates are again stored. The scanning continues till the end of the fringe is reached. Now the mask is setup at node 1 now the node is removed from the memory and the other branch is traced till the node 2 is reached. This node is now stored as the last value and tracing is continued till the end of the fringe. The mask is now set to node 2. The node 2 is then removed from the array and remaining branch is traced out. This procedure is repeated for the remaining branches as they are called from the array and traced out one by one.

The procedure also works well for the other types of theoretically generated images i.e. the ellipse , rectangle and the pair of intersecting lines. In the case of intersecting lines, the complete image is traced correctly.

### 2.7.2 Performance on fringe skeleton identified using the algorithm of Ramesh and Pramod [1]

The algorithm completely traces out the fringe skeleton in this case.

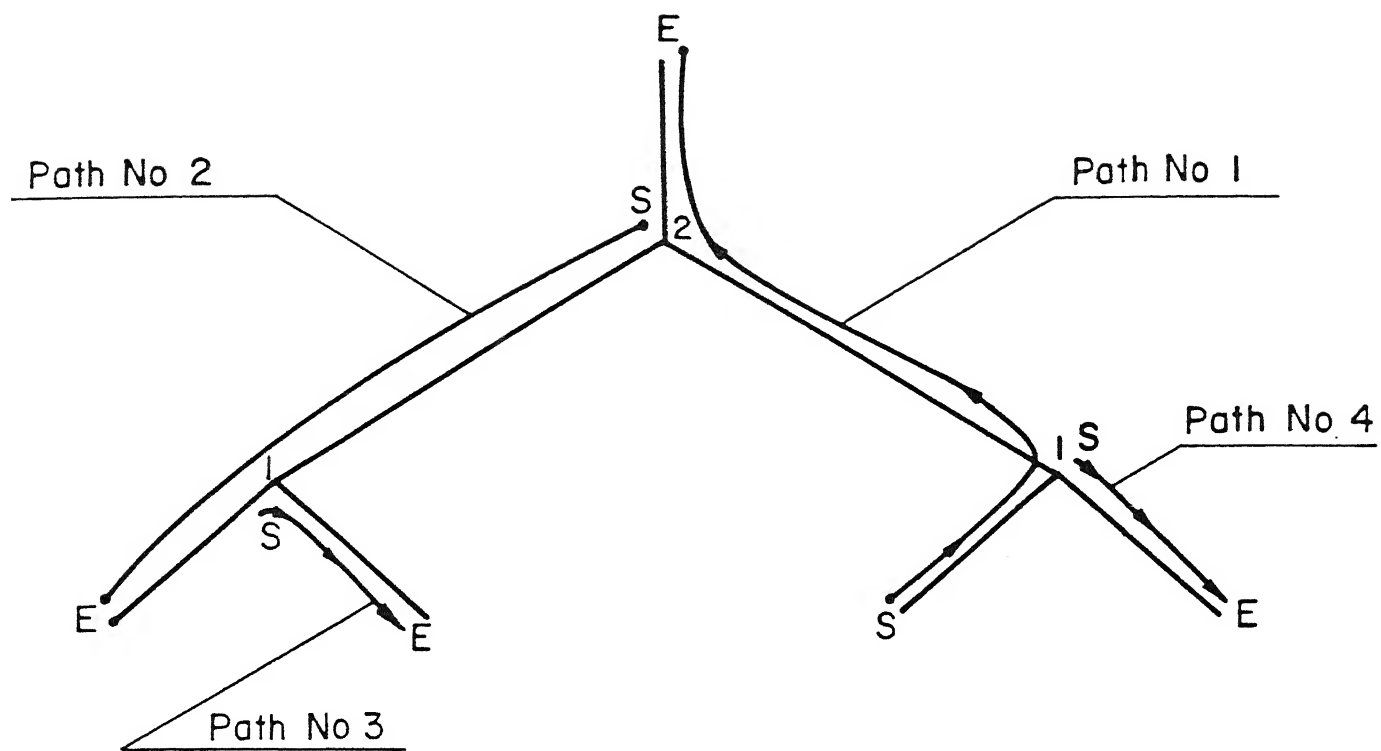


Fig. 2.10 Working of a complex fringe tracing algorithm for a tree image.

The sections of the fringe having more than one pixel thickness (due to interlacing) are of same class as the fringe branches of the tree image. All such points are stored on the array. When the mask fails to find a fringe pixel ( it may be an end point or a discontinuity ) it returns to the last branch and continues tracing. The entire fringe is marked in this fashion.

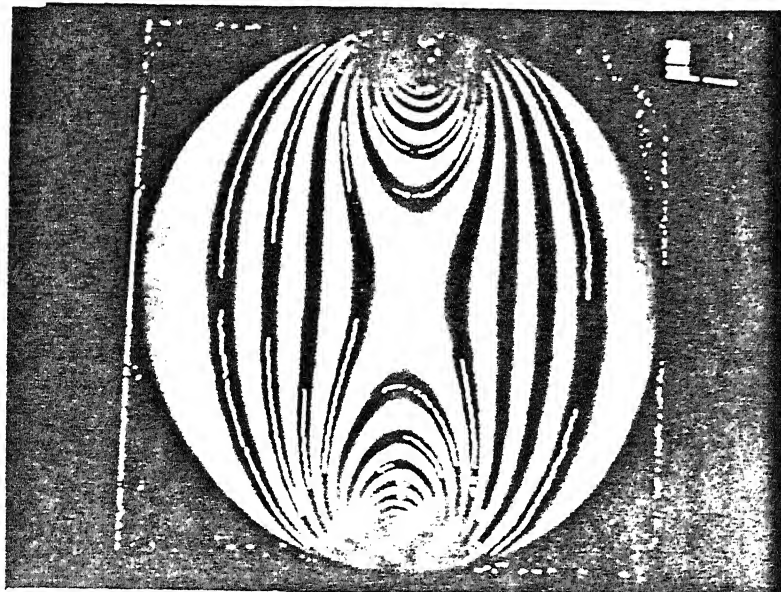
### 2.7.3. Performance on fringe skeleton identified using the algorithm of Ramesh and Pramod [1]

The algorithm works well for the actual fringe pattern images. The mask returns to all the branch points and traces out the fringe points. A comparative performance of the previously mentioned algorithms for the image of a circular disk under diametral compression is shown in Fig.2.11. Though the complex fringe tracing algorithm is comparatively better, there are situations wherein the algorithm has not traced the complete fringe. On close scrutiny it was found to be due to fringe discontinuity at these locations as shown in Fig.2.12.

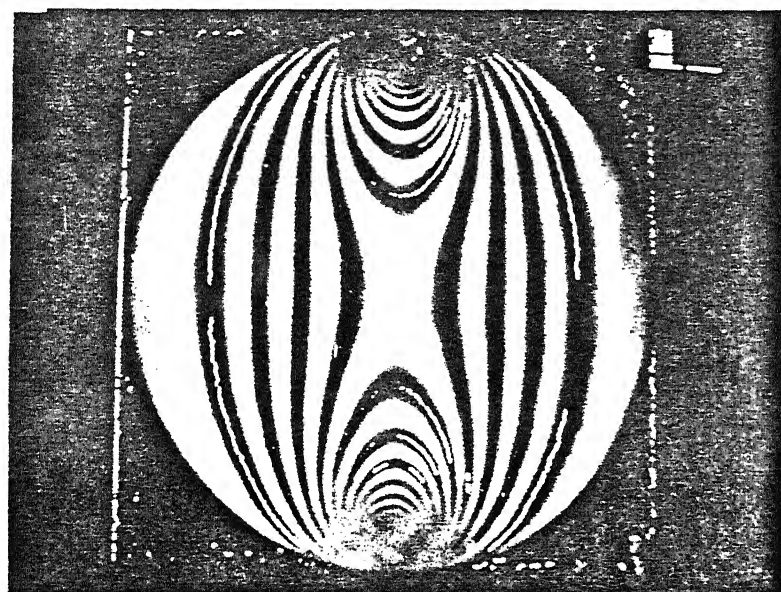
## 2.8 Closure

The relative performance of various algorithms show that the simple 3 X 3 mask alone is not sufficient for the actual fringe pattern images. The algorithm has also failed to trace completely the fringe even for some test images.

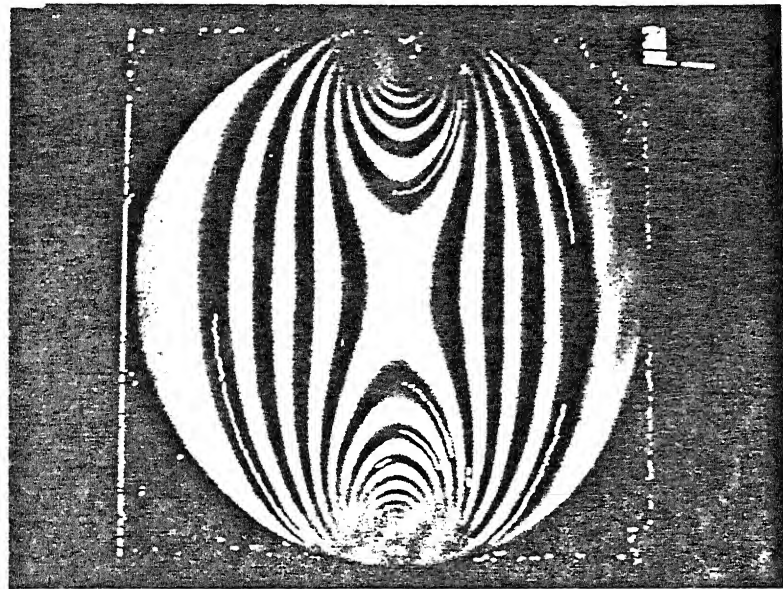
The 3 X 3 mask with the directional scan, is computationally efficient and performs very well for the nearly straight line fringes. Complete fringes are traced out. However in the case of the curved fringes, if there is interlacing effect, the mask shows deviation and is unable to trace out the entire fringe. However the user can restart the mask by giving a point on the unmarked part of the fringe interactively which eventually makes the procedure semi-automatic.



Performance of the 3 X 3 mask for an actual Photoelastic fringe pattern image.



Performance of the 3 X 3 mask with the direction scan for an actual Photoelastic fringe pattern image.



Performance of the complex fringe tracing algorithm for an actual Photoelastic fringe pattern image.

Fig. 2.11 Comparative performance of the 3 algorithms for actual photoelastic fringe pattern skeleton.

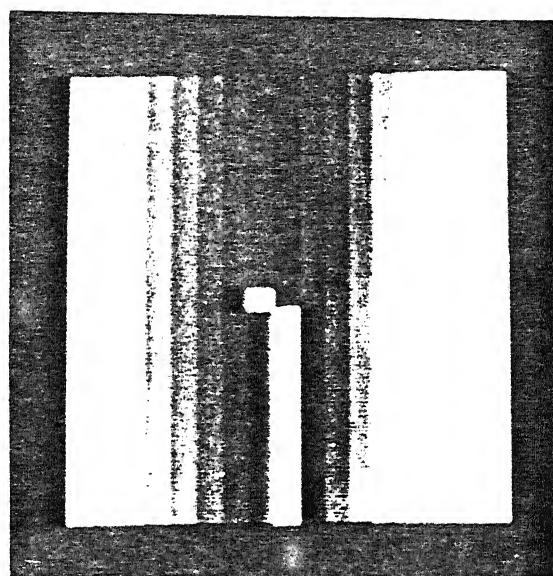


Fig. 2.12 Magnified image of a discontinuity in the fringe pixels.

The complex fringe tracing algorithm works the best for actual fringe patterns. This algorithm is slightly less efficient than the directional scan algorithm but successfully traces out the complete fringes. This algorithm can be used for a wide variety of path tracing problems. In actual implementation, the algorithm returns to all the branch points and scans for a fringe point even if that point is previously scanned by the other path. This drawback can be overcome by first determining if that branch is required to be scanned, after the end of the main branch is encountered.

The algorithm stops at a discontinuity. In principle this drawback can be overcome by evolving a suitable criteria to check if no pixels are found at a particular stage whether it is actually a fringe end or a discontinuity. In view of lack of time it has not been possible to implement this feature.

The next chapter discusses a new methodology for fringe ordering. The basic scheme, helps to order fringes along a particular scan direction. The procedure for fringe ordering discussed in the next chapter if coupled with fringe tracing discussed in this chapter can help to order the fringes in the entire field.

## CHAPTER 3

### A NEW METHODOLOGY FOR AUTOMATING THE FRINGE ORDERING

#### 3.1 Introduction

Fringe ordering is one of the crucial steps in the process of determining quantitative information from the fringe field. In general, the ordering of fringes has to be done systematically taking into consideration the physics of the problem and prior training is required to order the fringes. A few general guidelines to order the fringes are presented initially in this chapter.

Automation of the ordering of Photoelastic fringes is one of the challenging tasks even today. Ordering of the fringes becomes easier if in the fringe field a zeroth order fringe exists and the fringe gradient directions are known. Ramesh and Pramod [1] recognized the importance of the intensity data for fringe gradient calculation. They observed that at higher fringe orders, the grey level value of the minimum intensity pixel forming the fringe is higher.

In this chapter, the observation made by Ramesh and Pramod [1] on the intensity variation in the zone of stress concentration is further verified for a large number of images by plotting both 2d and 3d plots of the intensity variation.

A new methodology is proposed to identify the fringe gradient direction using the intensity variation in the fringe field. Fully automated algorithm to order fringes in the case of a circular disk under diametral compression is developed. An interactive approach for processing crack tip fringe patterns is implemented and guidelines for processing a general class of fringe patterns is proposed towards the end.

### 3.2 Fringe ordering in photoelasticity [13]

Experience and intuition have made the numbering of fringes in common cases of experimental stress analysis, and in particular the numbering of isochromatics in photoelasticity, almost a trivial matter. In general, however, the problem is far from trivial. There is no systematic methodology for this purpose.

Basically, most of the considerations can be linked to the fact that within the boundaries of a body the state of stress is uniquely defined and the stress and strains are continuous. Therefore on a line between two points with different values of stress; stresses with intermediate values must occur. Also, the stress tensor is uniquely defined so there can be only one state of stress at any point in the body. From this property, it follows that isochromatic lines of different order do not intersect. Because of continuity, the isochromatic lines are similar to the topological contours that end at the boundary of the pattern or form closed curves. The property of continuity helps in ordering the fringes.

#### 3.2.1 Guidelines to determine points at which shear is zero

When the white light is used, zero-order fringes appear black. This property does not help when monochromatic light source is used. Few of the geometric features which help in identifying the zeroth fringe order are presented below :

##### Square Corners :

Equilibrium requires that square outward corners on free boundaries have zero stresses in all directions. They are therefore points of zero shear. Numbering may start from these points and increase continuously. Uniqueness of the stress field also ensures that in case of having more than one such fringe the fringe ordering can be carried out in any sequence and the fringes will have consistent order.

##### Neighborhood of square corners :

In many cases it has been found that the stress tangential to the free boundary reverses sign in the proximity of the corner.

The point at which this reversal occurs is therefore also a point of zero shear Fig.3.1.

#### Reversal of sign on free boundaries :

When there is enough knowledge of the boundary conditions and of the gross stress distribution in the body, to know that there is a reversal in sign along a free boundary, the point of change of sign must be a point where the shear is zero. The classic case of the circular hole in a plate subjected to uniaxial loading is an example.

#### The Circular disk :

The circular disk subjected to diametral compression is a unique case. All points on the circumference of the disk have zero shear.

#### 3.2.2 Numbering of fringes in the general case

The uniqueness property of the stress values and the knowledge of one or several points at which shear is zero is sometimes not enough to determine unambiguously the order of all the fringes in the field. After giving certain fringe order it must be decided if the neighboring fringe order is one order higher or lower.

#### Time derivatives :

It is necessary sometimes to observe the development or the motion of the fringes, as the load is applied. As the load is increased, the first fringe appears at the point where  $\tau_{\max}$  is a maximum in the field and then moves towards the region of lower  $\tau_{\max}$ . When the applied load changes, all fringes except the zeroth order one move. The point from which the fringes move away when the load increases, is at a higher fringe order than its surrounding and the point towards which the fringes move as the load increases, is at a lower fringe order.

#### Space derivatives :

An isochromatic fringe pattern can be looked at as a topographic representation in three dimensions of the field of  $\tau_{\max}$ :

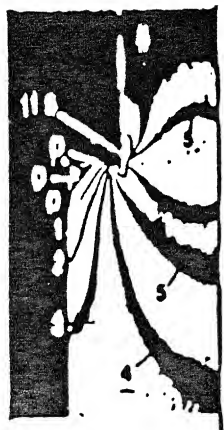
The order of the fringes gives the height, or level of the maximum shear stress field with respect to the plane of reference. In Fig.3.2 certain points have been called "peaks" and "valleys" to help understand the analogy. The peaks are points where  $\tau_{\max}$  is maximum. Valleys are points where  $\tau_{\max}$  is locally minimum. This minimum could be zero (case of the 'isotropic' or singular points) or could be a 'sink' where the stress is a minimum but has a finite value. In the case of the ring shown in Fig.3.2. there are four peaks on the inside boundary, at vertical and horizontal axis, and four valleys also on the inside boundaries, which happen to be of zero order.

Inside the field of the ring, on the horizontal axis, there are two valleys (zero order) and on the vertical axis there are two other valleys at which the order is finite.

Observation of the pattern in the ring shows that sometimes a fringe crosses itself or crosses one of the same order. This is obviously the case in the top half of the fringe pattern in Fig.3.2. for the fringe of order 2.5. The order of this fringes can be called 'transitional' order. The other transitional orders are those identified as about 1 and about 2 in the same figures.

The intersection of two transition order takes place at a point, identified as S in the figure and sometimes called a saddle point. The transitional fringes crossing at point S divide the space in four regions. In two of these regions opposite to each other, the order of the fringes increases as the counting starts from S. In the other two regions the order of the fringes decreases.

Saddle points are characteristically bounded by two isochromatic lines, one representing a shear somewhat greater than the one corresponding to the saddle point, and one with a shear somewhat smaller than the one corresponding to the saddle point. Both of these lines have two branches and the branches alternate with the branches of the other line to form a high-low-high-low pattern. Between the four branches there are asymptotic lines. The order of these lines was called 'transition order.'



a) ISOCHROMATICS



b) ISOSTATICS

Fig. 3.1 Appearance of zero-order isochromatics in the neighborhood of square corners.

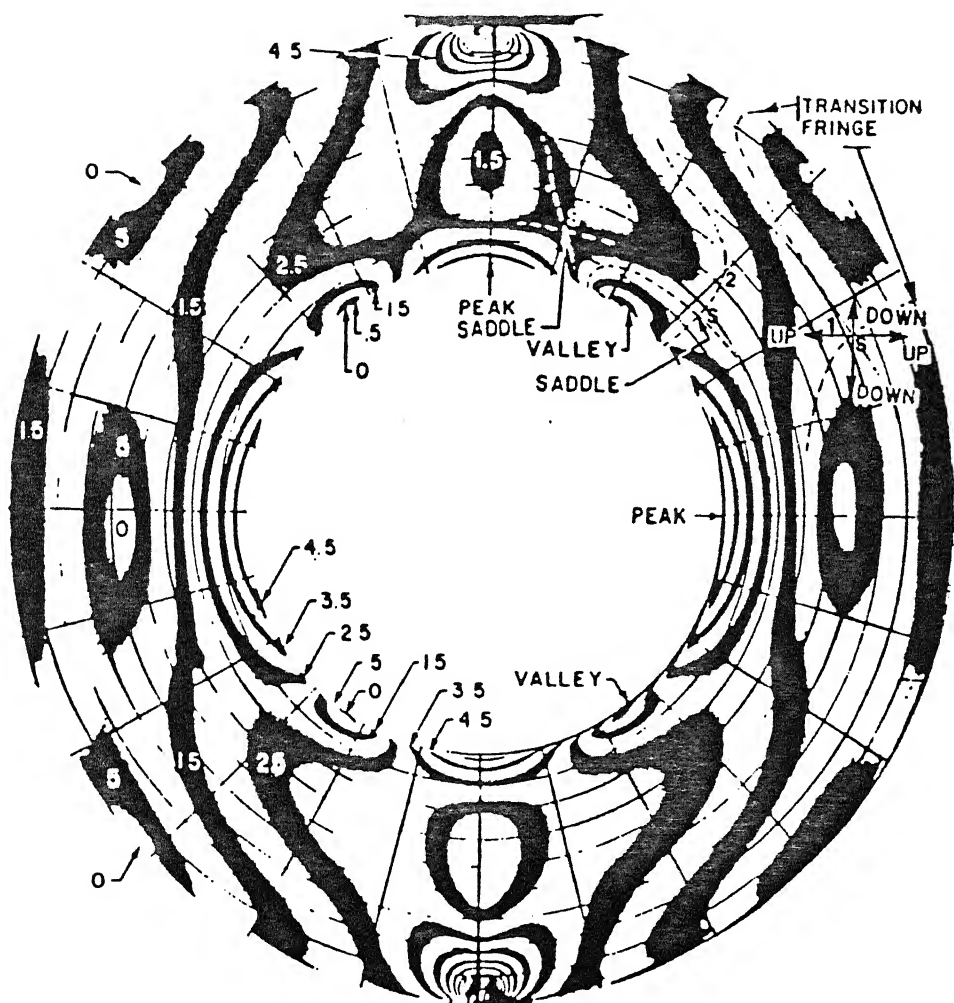


Fig. 3.2 Isochromatic fringes in a ring under diametral compression illustrating the presence of peaks, valleys, saddle and isotropic points.

This property of saddle points permits one to decide whether the order to be assigned to isochromatic fringes should increase or decrease.

### 3.3 New methodology for automation of fringe ordering

Automation of the ordering of Photoelastic fringes is one of the challenging tasks even today. Ordering of the fringes becomes easier if in the fringe field a zeroth order fringe exists and the fringe gradient directions are known.

Identification of the fringe gradient direction is possible through any one or a combination of the following procedures.

- (i) Load the model gradually and study the fringes as they change with the load.
- (ii) Identification of a source and the sink in the fringe field.
- (iii) Use of white light which provides a colour code to identify the gradient as well as the fringe orders.

From the point of view of automating fringe ordering, the procedure (iii) is a costlier option since the cost of a colour image processing system is at least three times the cost of a monochrome image processing system. The procedure (ii) is convenient for manual ordering of the fringes. However, if the information can be presented in a suitable form, it could be used for interactive ordering of fringes and in simple cases even complete automation is possible. Loading the model gradually is not the right choice for automation as one has to handle a large number of images to freeze the loading sequence.

Changing the light source in two dimensional photoelasticity changes the fringe order at the point of interest and the model fringe constant is also correspondingly altered. Except the zeroth fringe order, other fringes shift when the wavelength is changed. Umezaki et al [10] used this phenomena to identify the fringe gradient direction. The use of two different wavelengths has reduced the number of images to be processed to just two.

Ramesh and Pramod [1] recognized the importance of the intensity data for fringe gradient calculation. They observed that at higher fringe orders, the grey level value of the minimum intensity pixel forming the fringe is higher. It is due to the fact that the monochromatic light sources do not have 100% of the same wavelengths. A monochromatic source of sodium vapour ( $5893 \text{ \AA}$ ) has upto 4% of another wavelength of  $5896 \text{ \AA}$  [14]. In the view of this, the minimum intensity position forming the fringe is affected and the effect is pronounced at higher fringe orders. This leads to the umbrella shaped curve of the minima of the intensity values along a particular direction. Use of this phenomena requires only one image to be processed and is definitely advantageous.

### 3.4 Use of two dimensional intensity plots for determining the stress gradient direction

Figure 3.3 shows the plot of intensity variation along different lines in a circular disc under diametral compression. It can be seen that the variation in the minima of the intensity values is more pronounced at the higher stress gradient zones. This is because the monochromatic source used is not 100% of one wavelength as noted earlier. The value of the minimum intensity is higher as the point becomes more stressed. In a sense the model becomes more transparent at stress concentration zones.

The same effect can be observed in the case of the crack image Fig.3.4 and Fig.3.5.

The annular ring under diametral compression shown in Fig. 3.6 provides a most general class of the fringes. This pattern has its unique characteristic fringes in the form of a source, the sink and the saddle points which have a positive fringe gradient in one direction and a negative fringe gradient in the perpendicular direction. If the ordering of the fringes can be automated for this case then one can say without exaggeration that any other fringe field can be automatically ordered.

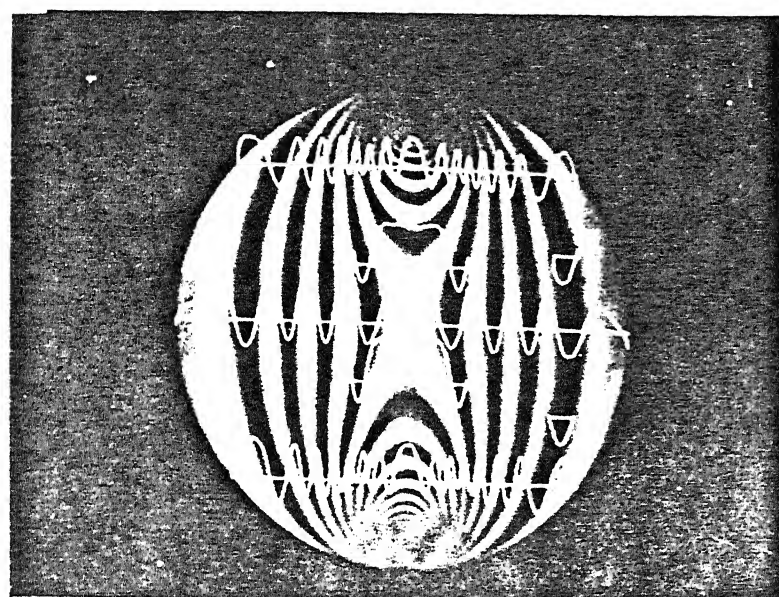


Fig. 3.3 Variation in intensity along various scan directions for the fringe pattern of a circular disk under diametral compression.

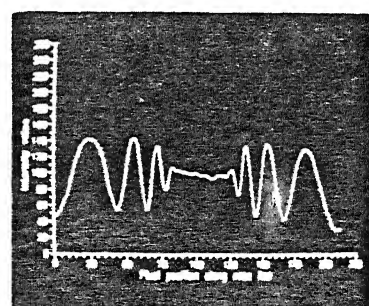
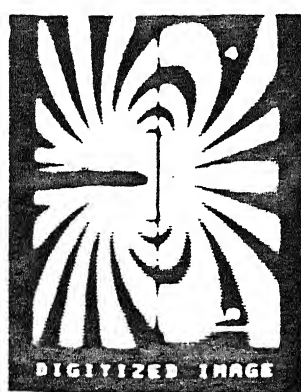


Fig. 3.4 Variation in intensity for a crack tip fringe pattern.

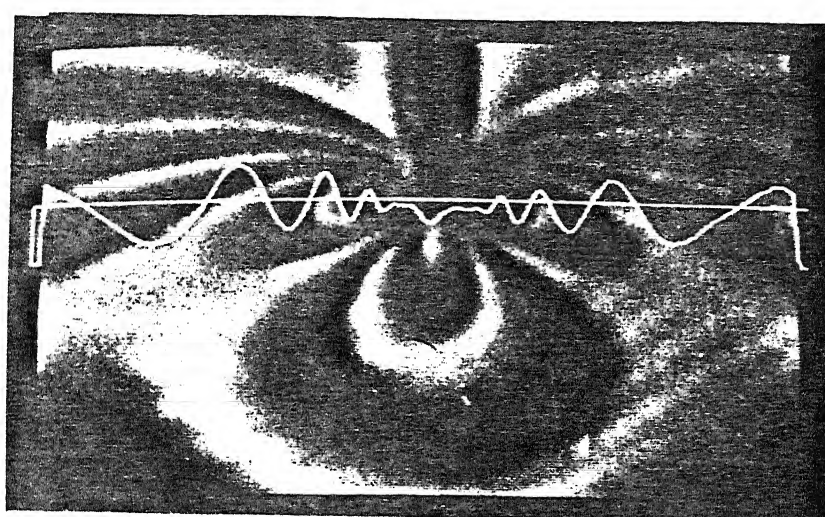


Fig. 3.5 Variation in intensity for a crack tip fringe pattern.

Source and sink can be identified manually if the model is gradually loaded and the fringe movements are observed. Figure 3.6 shows the intensity variation along different scan lines. The figure clearly shows that at higher orders the minimum intensity point forming the fringe skeleton has a higher value than that for the lower fringe orders. This observation again reinforces the fact that fringe gradient direction can be correctly identified in the neighborhood of the source. The question now is, can the intensity variation also indicate the location of a sink in the fringe field ? Figure 3.7 shows the variation in the intensity values along the line segment passing through a sink. It shows that the magnitude of the minimum intensity is lower for the inner fringe than that for its enclosing fringe, thus showing that the inner fringe is at a lower fringe order than the surrounding one, confirming the existence of a sink. This proves that the minimum intensity variation can be used as a criteria for fringe ordering even in the neighborhood of a sink.

### 3.5 Three dimensional intensity plots for various types of fringe fields

The two dimensional display is able to provide intensity information along a particular direction. However to obtain information of the whole field, a three dimensional plot of the intensity profile is drawn.

Figure.3.8 shows the screen origin and the area of interest to be scanned for plotting intensity profile.

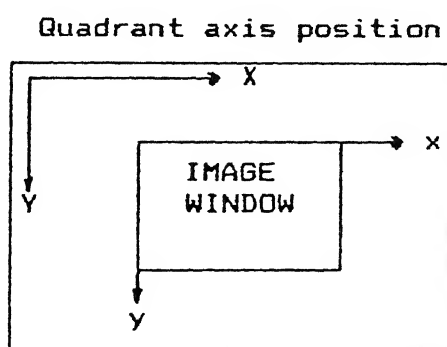


Fig.3.8 The image and the screen coordinate system.

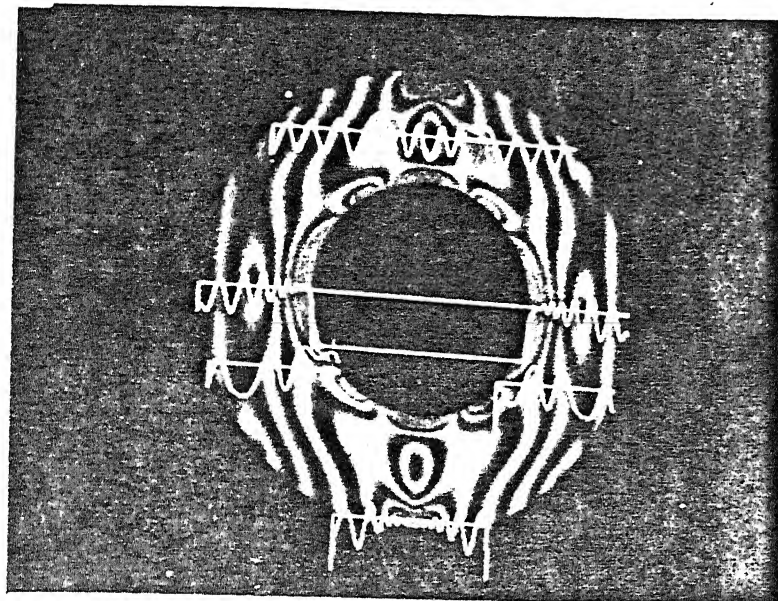


Fig. 3.6 Variation in intensity along various scan lines for an annular ring under diametral compression.

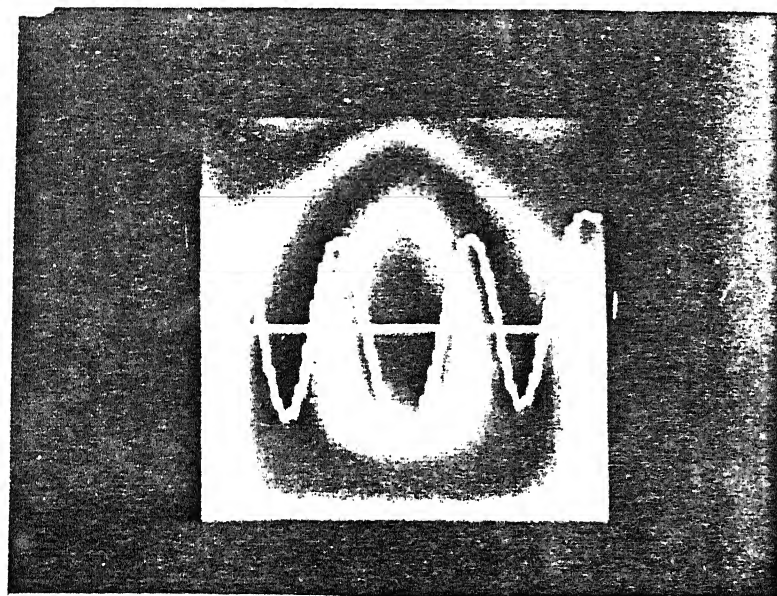


Fig. 3.7 Magnified view of the intensity variation across a sink point in the annular ring.

Coordinate transforms are applied to a fringe pattern image with the X and Y values as the coordinates of the point (in pixels) and the corresponding pixel intensity as the Z coordinate. The image is scanned row wise. For each point the intensity value is read and assigned to the Z coordinate. The rotation transform is then performed and the image is displayed. The actual transform equations are as follows :

1. The origin of the window is translated to the screen origin ( $T_x$ ,  $T_y$ ).

$$\begin{aligned}X_1 &= X - T_x \\Y_1 &= Y - T_y\end{aligned}$$

2. Rotation about the X, Y and Z axis in that order, about the screen origin ( $R_x$ ,  $R_y$ ,  $R_z$ ) is then performed.

$R_x$  i.e. rotation about X axis by  $\theta_x$ .

$$\begin{aligned}X_2 &= X_1 \\Y_2 &= Y_1 \cos\theta_x + Z_1 \sin\theta_x \\Z_2 &= -Y_1 \sin\theta_x + Z_1 \cos\theta_x\end{aligned}$$

$R_y$  i.e. rotation about Y axis by  $\theta_y$ .

$$\begin{aligned}X_3 &= X_2 \cos\theta_y - Z_2 \sin\theta_y \\Y_3 &= Y_2 \\Z_3 &= X_2 \sin\theta_y + Z_2 \cos\theta_y\end{aligned}$$

$R_z$  i.e. rotation about Z axis by  $\theta_z$ .

$$\begin{aligned}X_4 &= X_3 \cos\theta_z + Y_3 \sin\theta_z \\Y_4 &= -X_3 \sin\theta_z + Y_3 \cos\theta_z \\Z_4 &= Z_3\end{aligned}$$

3. The figure is then translated back to the window origin  $(-T_x, -T_y)$ .

$$\begin{aligned} X' &= X_4 + T_x \\ Y' &= Y_4 + T_y \end{aligned}$$

4. The new  $X'$  and  $Y'$  values are plotted, giving a 3d projected view of the fringe pattern.

In general, the rotation angles are so chosen that the final image obtained is aesthetically pleasing. The values of  $\theta_x$ ,  $\theta_y$  and  $\theta_z$  used in the present study was  $10^\circ$ ,  $-10^\circ$  and  $45^\circ$  respectively. Apart from these, a suitable scaling was also required in the  $Z$  axis coordinate. The values used in the present investigation range from 0.65 to 1.75. Further, care needs to be taken while scanning the image. Finer scan was not beneficial and coarser scanning of the order of the 3 to 4 for normal as well as zoomed images, magnified by the order of 3 X 3 to 9 X 9 were found to be effective.

Fig.3.9 shows the 3 dimensional plot of the intensity variation over the circular disk under diametral compression. Fig.3.10 shows the zoomed view of the high stress gradient zone near the loading point. Figure 3.11 and Fig.3.12 show the intensity profile for crack-tip fringe patterns.

Fig.3.13 shows the 3 dimensional intensity plot of the annular ring under diametral compression. Fig.3.14 and Fig.3.15 shows the zoomed view of the sink point and the saddle point. The topographical features help in easy identification of the variation in the fringe order.

The 3D plots have clearly brought out the fact, that there is substantial intensity variations in the fringe field. Use of intensity information has not been paid much attention earlier, in view of the difficulties in recording intensity information. Intensity was monitored at a few selected points or along specified lines using a photo multiplier tube.

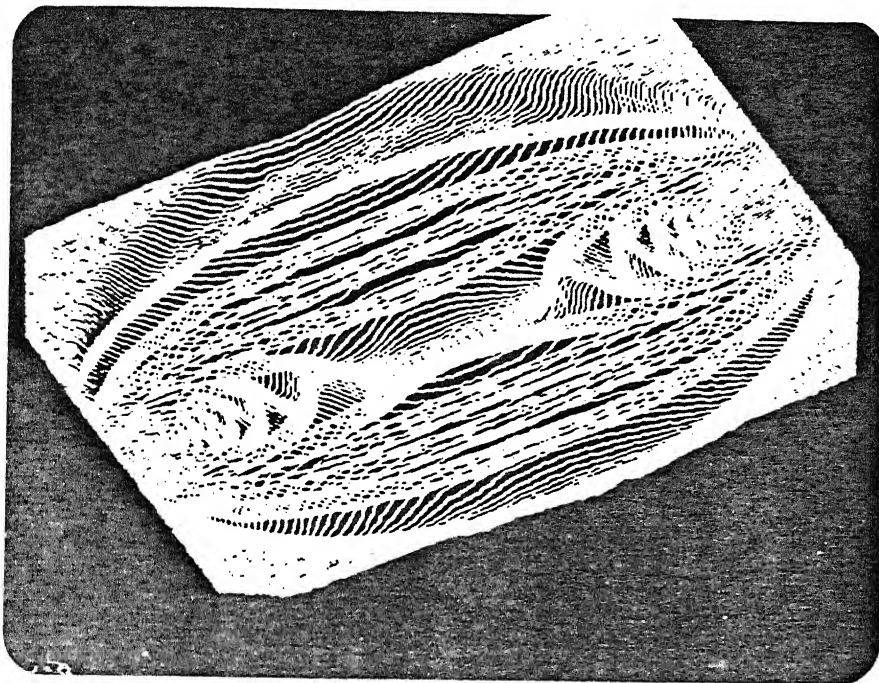


Fig. 3.9 3-dimensional plot of variation in intensity over a circular disk under diametral compression.

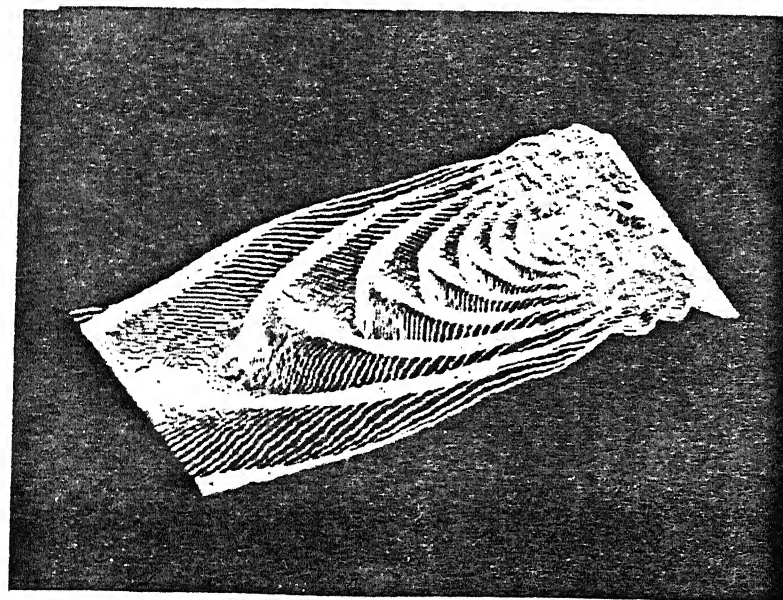


Fig. 3.10 Magnified view of the high stress gradient zone at the contact point for the circular disk under diametral compression

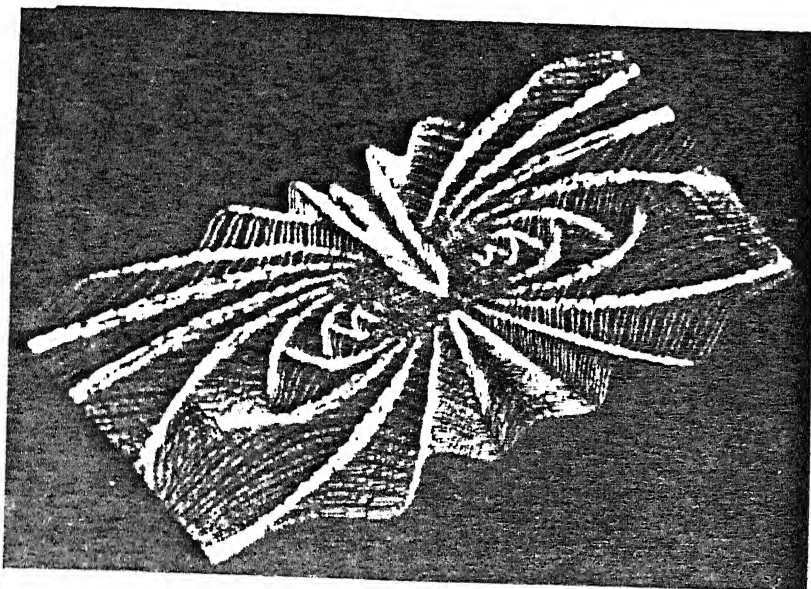


Fig. 3.11 3-dimensional intensity profile for the crack tip fringe pattern.

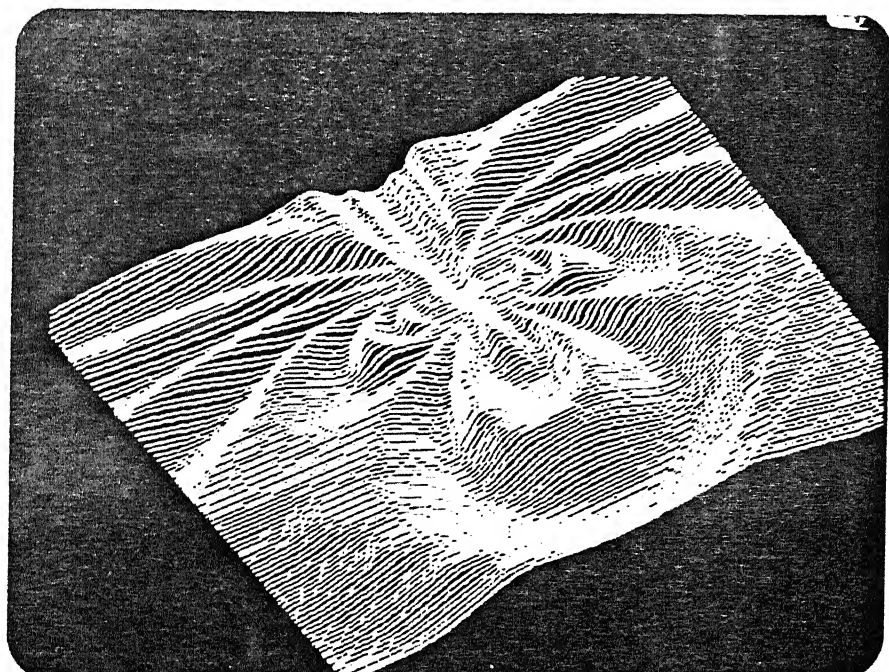


Fig. 3.12 3-dimensional intensity profile for the crack tip fringe pattern with a frontal loop.

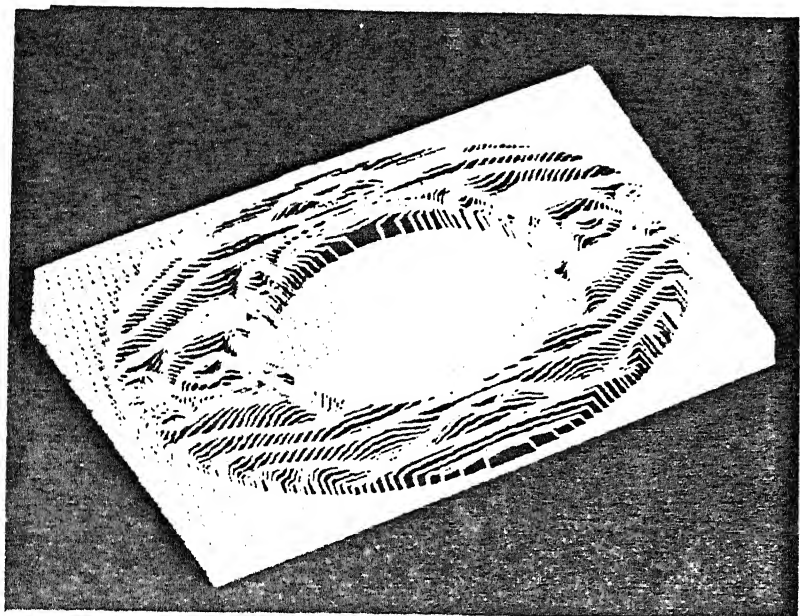


Fig. 3.13 3-dimensional intensity profile for annular ring under diametral compression.

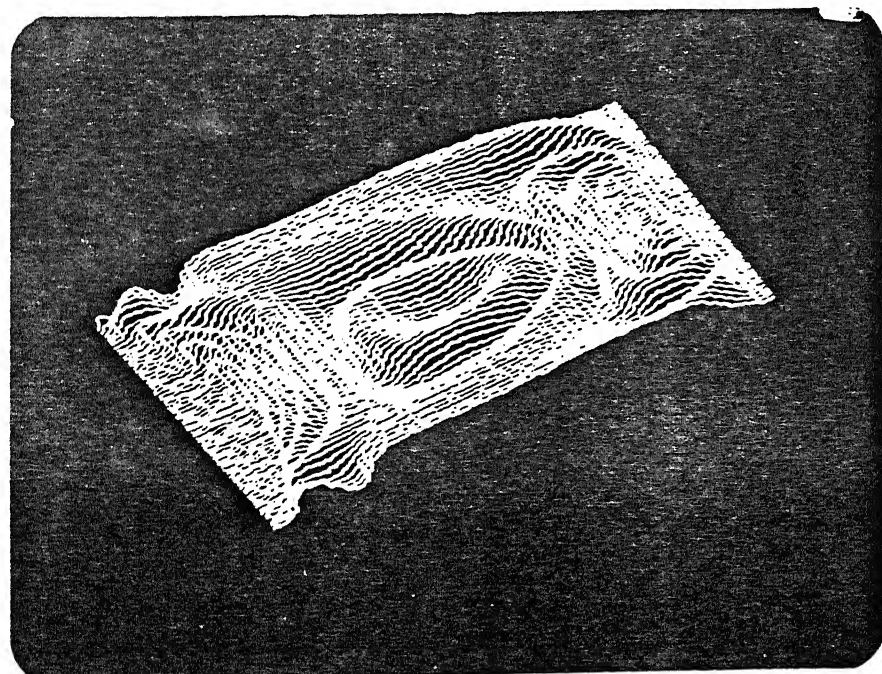


Fig. 3.14 3-dimensional plot of the magnified view of the sink point.

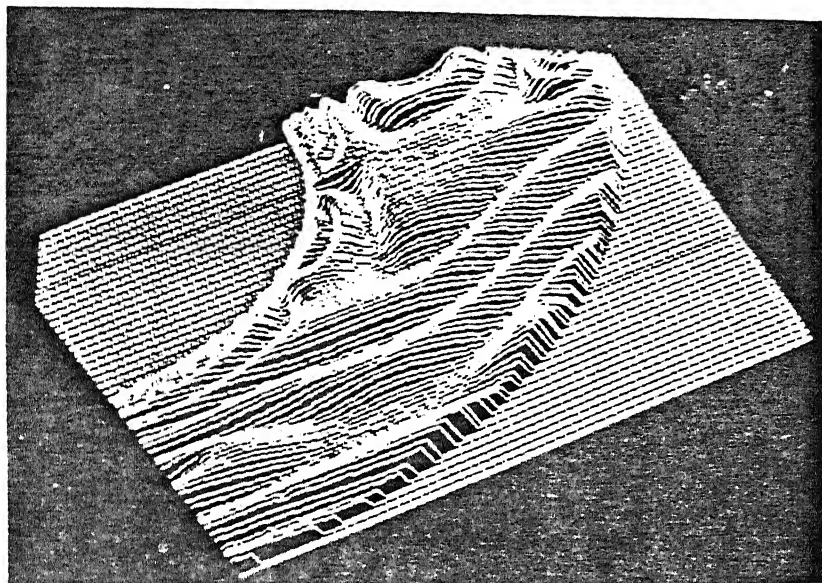


Fig. 3.15 3-dimensional plot of the magnified view of the saddle point.

Collecting intensity data over a field was unthinkable earlier. The modern developments in the technology have given rise to the development of CCD cameras, which can quantize the intensity values over the entire field at video rate. The resolution of the cameras are substantially higher to capture even minute variations in the intensity information. This development has showed promise to use intensity variations for data processing.

### 3.6 Automation of fringe ordering for special class of fringe patterns

It has been established in sections 3.4 and 3.5 that intensity variation in the fringe field could be used to judiciously identify fringe gradient direction. To achieve this, a proper choice of scan direction need to be selected. The problem becomes much simpler, if the nature of the fringe field is known apriori.

Knowing the gradient direction, if fringe order of any point lying in the gradient direction is known, then it is possible to identify fringe orders for any other point. To know the ordering of the fringe field, fringe tracing algorithm must be used to trace out the complete fringes. The new scheme involves the following steps.

1. Fringe thinning to identify fringe skeleton.
2. Fringe ordering along a particular scan direction using,
  - (i) User specified basic information on the model geometry.
  - (ii) Intensity variation over the field to identify the fringe gradient direction either independently or along with step (i).
3. Use of fringe tracing algorithm to order the complete fringe field.

The scan path, has to be found out such that all the fringes within the field are located and scanned in proper order. This fact is very critical to ensure correct ordering of the fringes. This information has to be provided by the user in case of the general class of the images. Knowledge of the model geometry can provide the following information. Location of the crack tip in case of the crack problem, or coordinates of the loading point enables the program to determine the "source".

If the free surface is indicated then gradient direction can be established. For specific class of problems, i.e. the circular disk under diametral compression and the mixed mode fringe pattern, the scan direction have been determined to work for most of the fringe patterns of these classes.

### 3.7. Automation of fringe ordering for a circular disc under diametral compression

Calibration of photoelastic materials is one of the important step in any photoelastic experiment. Many laboratories use circular disk under diametral compression as a model to determine this. Automation of fringe ordering and subsequent analysis of data for such a case is desirable.

Circular disk comes under a special category as noted in Sec. 3.2.1. that the boundary of the disk except the loading points is at zeroth fringe order. The fringe pattern is symmetric about both X and Y axes. The fringe order increases from the free surface, to the loading point. Hence the scan path must, ideally be perpendicular to every fringe and should start from the free surface and go upto the load point Fig.3.16. The positive X and Y axis are a correct choice for the scan paths. The algorithm searches for the fringes from the farthest fringe point on the positive X axis to the centre of the disk and from the centre of the disk, along the positive Y axis till the load point. It must be ensured that the loading points should be more or less oriented along the Y axis. Implementation of the algorithm requires the determination of the centre and the diameter of the disk.

An interactive procedure is implemented to identify the centre and the boundary of the circular disk and a circle is drawn using the graphics command, corresponding to this centre and radius chosen. If the circle lies exactly on the boundary of the disk then these centre and radius values are accepted, otherwise the circle is erased and the procedure is repeated.

1. The image is cleaned and then skeletonised using the algorithm by Ramesh and Pramod [1]. This image is loaded in quadrant 0.

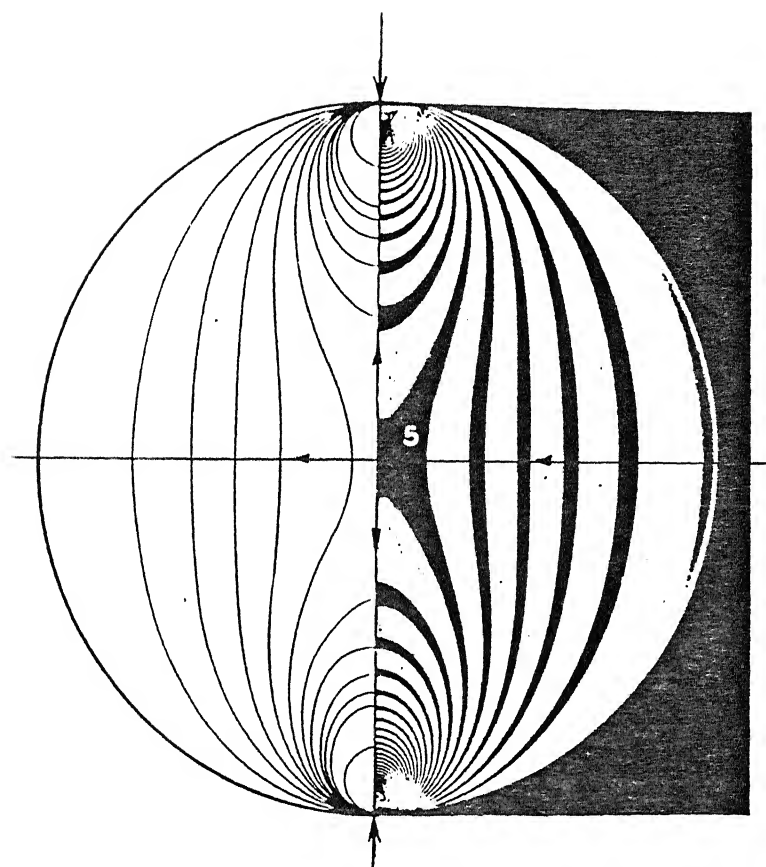


Fig. 3.16 Selection of scan path for the circular disk under diametral compression.

CENTRAL LIBRARY  
I.I.T., KANPUR  
Ref. No. A. 117558

2. Since the boundary of the disk is known, the farthest fringe point on the X axis is known.

3. The i and the j values are initialized to these coordinates and the complex fringe tracing algorithm is used to trace this fringe. The fringe is marked with intensity value equal to its fringe order.

4. On reaching the end point of the fringe, the original i and the j values are read and the pixels are read along the scan path to locate the other fringes.

5. The mask is moved along the X axis, towards the centre of the disk till the next fringe is located. The fringe order is then incremented and this fringe is traced out using the complex fringe tracing algorithm.

Steps 4 and 5 are repeated till the mask reaches the centre of the disk.

6. The previous fringe order is then stored in the memory and the mask continues to scan for the next fringe along the negative X direction, away from the centre. The fringe orders are now known as the fringes are also symmetric about the Y axis.

7. When a fringe point is located, the fringe is traced out in the intensity corresponding to its fringe order and the fringe order is decremented.

This procedure is repeated till the disk boundary is encountered. Now the mask is set at the disk centre and the other part of the scan path is searched.

8. The fringe order stored in the memory is recalled and incremented by one. The mask now scans for a fringe point along the positive Y direction. The fringes are marked as the fringe points are located and the fringe value is incremented by one. This procedure is repeated till the the boundary of the disk is reached.

9. Same procedure is repeated for scanning the fringes along the negative Y direction upto the other loading point, thus ordering all the fringes.

10. The fringe ordering obtained by the above procedure is cross checked by comparing the intensity profile gradient to fringe gradient.

### 3.8. Interactive fringe ordering for the mixed mode crack-tip fringe pattern

Selection of the scan path :

The mixed mode crack fringe patterns are non symmetric. Hence a more complex criteria is required to determine the scan path. The problem is split into two parts determined by the geometry of the fringes. The fringes are in the form of either elliptical loops oriented along the Y direction or near straight fringes ( parts of big loops which go out of the image field ). Apart from these, in some cases frontal loops also exist.

The scan paths are different for each of these classes of fringes. For the elliptical fringes oriented along the Y direction and the linear near vertical fringes , a line parallel to the X axis (the crack axis) and at sufficient distance from the origin on either side is selected, as indicated in Fig.3.17. The distance is decided by the resolution of the fringes close to the crack tip. This value is usually about 2 to 3 times the crack thickness as seen on the screen i.e. 10 to 15 pixels. The line segment is from the negative X extent of the image window upto the crack tip. The scan path is required to extend beyond the crack tip to trace the open loops or the near linear vertical fringes on the positive X axis (Fig.3.17). For the closed and the open frontal loop , the scan path is selected along the Y direction at some distance on the positive X axis, from the crack tip. This scan path is from the positive extent of the Y axis to the crack tip Y coordinate.

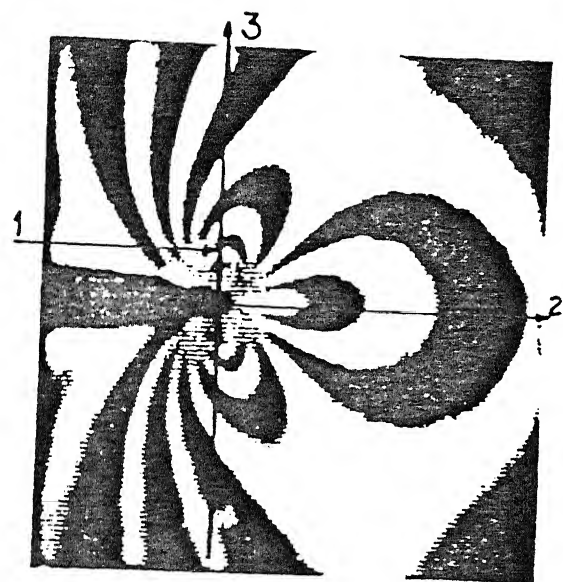


**Fig. 3.17 Selection of scan path for the crack tip fringe pattern.**

In general, one does not have a zeroth fringe order along these directions, hence the user is required to provide the fringe order for one of the points on these fringes.

Algorithm :

1. The image is cleaned and then skeletonised using the algorithm by Ramesh and Pramod [1]. The original image is loaded in quadrant 0. It is to be ensured that the orientation of the crack should be along the positive X axis. The crack tip is to be located by the user, with the help of the cursor.

Scan Path 1 :

2. The scan path is set up from coordinate corresponding to the negative X extent and Y coordinate is 10 pixels above the crack tip.

3. The cursor is displayed and the user is asked to input the fringe order of the first fringe intersecting the scan path.

4. When a fringe point is located, the complex fringe tracing algorithm (section 2.4.4) is used to trace out that fringe then the fringe order is incremented and the scanning continues till the crack tip X coordinate is reached.

Scan path 2 :

5. The knowledge that ahead of the crack tip along the crack axis a sink is present, is used. The second scan path, parallel to the Y axis is set and the user is asked to input the fringe order of the outermost fringe along this path. The pixels along this path are then scanned for the frontal loop and the open fringes.

6. On reaching the fringe pixel the fringe is traced out and the value is decremented by one. This is because of the presence of the sink.

This procedure is repeated till the crack tip Y coordinate is reached.

Scan path 3 :

7. Now the open loops and the near linear fringes are traced. The pixels are scanned along the path parallel to the X axis, from the crack tip to the X window extent.

8. When a previously traced pixel is located the fringe order is set to this value.

9. On encountering a fringe pixel the fringe order is decremented by one and it is traced out.

Thus the complete set of fringes around a crack tip are scanned.

In view of the interactive selection of scan paths the procedure is only a semi-automatic.

### 3.9. Closure

It has been successfully demonstrated in this chapter that intensity variation in the fringe field is not trivial but can yield a very useful information on the fringe gradient directions. Though, fringe ordering for complex image is difficult, a few general guidelines to order them are presented.

While developing the automatic fringe ordering algorithms for circular disk and crack tip images only minimal information need to be input by the user. Further, the information needed was simple, and any one with basic background in Mechanical Engineering will be able to provide this information.

The annular ring image represents one of the most complex fringe pattern. This image is used as a further check to utilize the concept of using intensity variation for fringe gradient identification. Typical intensity variation in the neighborhood of a "source" and a "sink" were obtained. Following the lines of the circular disc and the crack-tip image it is possible to develop a module to identify fringe ordering in an annular ring.

Fringe ordering is only an intermediate step and one needs methodologies to extract field parameters using the fringe data. The next chapter provides a methodology to extract the stress field parameters in the neighborhood of a crack tip from the information of the fringe order and positional coordinates of various points.

## CHAPTER 4

### EVALUATION OF STRESS INTENSITY FACTOR USING A HIGHER ORDER THEORY

#### 4.1 Introduction

One of the important stress field parameters that is to be evaluated in Fracture Mechanics problems is the Stress Intensity Factor(SIF). Photoelasticians recognised way back in 1958 itself[15] the fact that atleast two parameters are needed to characterise the stress field in the close vicinity of the crack-tip. The correct determination of  $K_I$  is possible only if both the parameters namely  $K_I$  and  $\sigma_{ox}$  are determined from the stress field. The ingenuity of Irwin [15] to generate two equations from a single data point from the fringe field, made the evaluation of Mode I SIF and  $\sigma_{ox}$  very simple and did not warrant the use of digital computers.

Sanford [3] proposed an overdeterministic method to evaluate  $K_I$  and  $\sigma_{ox}$  in a least square sense using information from the field rather than a single point as was used by Irwin[15]. The data to be collected included the fringe order and positional co-ordinates of various points in the field. In view of the large volume of data to be collected, there was increasing demand at this stage to automate the data collection process.

Most of the practical structures of engineering importance have finite dimensions and the cracks in them may be located in zones of stress concentration and the cracks may be large enough so that the crack-tip may be closer to a boundary. The basic stress field equations of fracture mechanics are developed for cracks lying in a body of infinite dimensions (i.e., the crack-tips are far away from the boundaries) subjected to an uniform stress field. When these equations are attempted to be applied for solving real life problems, one gets erroneous results.

The recognition of this fact has lead the researchers to account for this effect and multi-parameter stress field equations have been developed in the past two decades.

Among the muti-parameter stress field equations, the simplicity equations proposed by Atluri and Kobayashi[2] are the simplest one and their equivalence with other equations is brought out in Ref.11. Using these equations and following the methodology of Sanford[3], an overdeterministic least square method is developed to extract the stress field parameters from the isochromatic fringes.

#### 4.2. Developments in the description of the stress field equations in the neighborhood of a crack-tip

##### 4.2.1 Single Parameter Stress Field Equation

The Westergaard [16] complex stress function technique for solving opening mode crack problems has played an important role in the development of linear elastic fracture mechanics. Westergaard in his paper gave the stress functions for the cases of a central crack and a series of equally spaced straight cracks of length  $2a$  in an infinite plate with a biaxial field of tension  $\sigma$ . Westergaard originally reported that his stress function models the stress field for the case of a crack/tracks in an uniaxial stress field. However, it has been shown by later investigators that Westergaard's solution is valid only for a biaxial field. Irwin[17] in 1957 following the semi-inverse procedure suggested by Westergaard added three additional examples. They are

(1) Single crack along the x-axis extending from  $-a$  to  $a$  with a wedge action applied to produce a pair of "splitting force" of magnitude  $P$  located at  $x = b$ .

(2) The situation of above example with an additional pair of forces of magnitudes  $P$  at  $x = -b$ .

(3) Example(1) repeated along the x-axis at intervals  $\ell$  and with the wedge action centered so that  $b$  is zero.

Irwin[17] showed that in all the above five cases the stress distribution near the end of the crack can be expressed independent of the type of loading if the region of interest is very close to the crack-tip (i.e.  $r/a$  and  $r/(a-b)$  may be neglected in comparison to unity) and introduced the concept of Stress Intensity Factor(SIF). The expressions thus obtained are known as classical Westergaard equations and for a Mode I loading situation they are given as,

$$\begin{bmatrix} \sigma_x \\ \sigma_y \\ \tau_{xy} \end{bmatrix} = \frac{K_I}{\sqrt{2\pi r}} \cos \frac{\theta}{2} \begin{bmatrix} 1 - \sin \frac{\theta}{2} \sin \frac{3\theta}{2} \\ 1 + \sin \frac{\theta}{2} \sin \frac{3\theta}{2} \\ \sin \frac{\theta}{2} \cos \frac{3\theta}{2} \end{bmatrix} \quad (4.1)$$

#### 4.2.2. Two Parameter Stress Field Equation

Irwin [17] observed that when an extending crack moves across a plate of finite width, the crack may attain sufficient length so that the stress-field equations obtained from the consideration of a crack in an infinite body may not be accurate. He reported that correction needs to be applied for a finite body and introduced a constant stress term  $\sigma_{ox}$  to the  $\sigma_x$  term. Thus, the modified Westergaard equations become,

$$\begin{bmatrix} \sigma_x \\ \sigma_y \\ \tau_{xy} \end{bmatrix} = \frac{K_I}{\sqrt{2\pi r}} \cos \frac{\theta}{2} \begin{bmatrix} 1 - \sin \frac{\theta}{2} \sin \frac{3\theta}{2} \\ 1 + \sin \frac{\theta}{2} \sin \frac{3\theta}{2} \\ \sin \frac{\theta}{2} \cos \frac{3\theta}{2} \end{bmatrix} + \begin{bmatrix} -\sigma_{ox} \\ 0 \\ 0 \end{bmatrix} \quad (4.2)$$

In a discussion of the paper by Wells and Post[18], Irwin[15] in 1958 reported a method to evaluate,  $K_I$  as well as  $\sigma_{ox}$  stress term from the isochromatic fringe patterns. Using these values he theoretically plotted the contours of maximum shear stress (isochromatic fringes) and showed that the prominent tilt seen in the experiment is well represented.

On the otherhand if one uses classical Westergaard's equations one gets the fringes symmetric with respect to both x and y axis. This situation occurs in the experiment in a region very close to the crack-tip. In a sense the use of the second term has helped in enlarging the zone of data collection.

Sih [19] in 1966 starting from the Goursat-Kolosov complex representation of the plane problem showed that the symmetry condition  $\tau_{xy} = 0$  on  $y = 0$  could be satisfied by a less restrictive assumption than employed by Westergaard. He obtained near-field stress equations which included a constant term to  $\alpha_x$  term. Later Eftis and Liebowitz [20] in 1972 showed that Westergaard's stress function can be related to the Goursat-Kolosov complex representation. They confirmed that Sih's equations are the same as Irwin's modification to the Westergaard equations.

#### 4.2.3. Multi Parameter Stress Field Equations

Sanford in 1979 [3] observed for the first time that when the crack length increases in an Modified Compact Tension (MCT) specimen, several isochromatics cross the crack-axis (Fig.4.1). Sanford reported that this phenomenon is due to the finite dimensions of the specimen. In order to account for finite bodies, Tada, Paris and Irwin [21] introduced a series form of Westergaard stress function. Sanford [22] observed that the modified Westergaard functions predict only a constant fringe order along the crack-axis. However, for cracks approaching a boundary, several fringe orders cross the crack-axis. This counter-example raises questions about the validity of the modified Westergaard equations.

Starting from this standpoint, Sanford reported that an additional stress function  $Y(z)$  should be added to the series form of Westergaard stress function  $Z(z)$  where  $z$  is  $x+iy$  and  $i$  is  $\sqrt{-1}$ . He showed that the condition  $\tau_{xy} = 0$  on  $y = 0$  can be achieved by a less restrictive assumption than used by Westergaard.

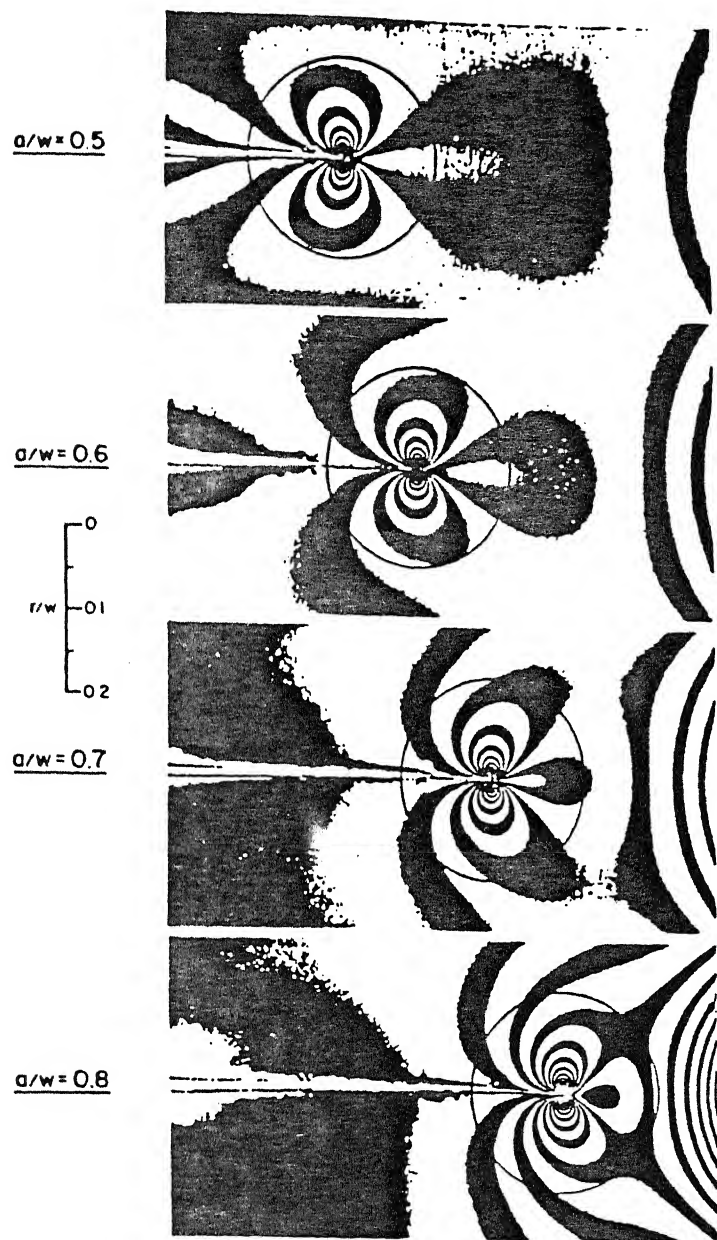


Fig. 4.1. Isochromatic fringe pattern observed in an Modified Compact Tension specimen. Isochromatics cross the X axis for larger  $a/w$  values.

He selected the additional stress function  $Y(z)$  such that it satisfies the condition  $\text{Im}(Y(z)) = 0$  on  $y = 0$ . He expressed the stress function  $Y(z)$  in a series form. With this additional stress function, Sanford and his co-workers[22] showed that crack-tip stress fields can be better characterized. In all the papers reported by Sanford and his co-workers[22] the stress field is represented only in terms of complex stress functions and they are,

$$\begin{bmatrix} \sigma_x \\ \sigma_y \\ \tau_{xy} \end{bmatrix} = \begin{bmatrix} \text{Re}(Z) - y \text{Im}(Z') - y \text{Im}(Y') + 2 \text{Re}(Y) \\ \text{Re}(Z) + y \text{Im}(Z') + y \text{Im}(Y') \\ -y \text{Re}(Z') - y \text{Re}(Y') - \text{Im}(Y) \end{bmatrix} \quad (4.3)$$

where  $Z'$  and  $Y'$  are the first derivatives of  $Z$  and  $Y$  respectively with respect to  $z$ .

For a single-ended crack, with the origin of co-ordinates at the crack tip and the negative  $x$ -axis coinciding with the crack faces, the functions  $Z(z)$  and  $Y(z)$  can be expressed as;

$$Z(z) = \sum_{j=0}^J C_{2j} z^{j-\frac{1}{2}} \quad (4.4)$$

$$Y(z) = \sum_{j=0}^J C_{2j+1} z^j \quad (4.5)$$

where  $C_{2j}$  and  $C_{2j+1}$  are real coefficients.

(Note : In the literature series coefficients of  $Z(z)$  are denoted by  $A_j$  and for  $Y(z)$  as  $B_m$ . However replacing them by  $C_{2j}$  and  $C_{2j+1}$ , it is simpler to collect powers of  $r$  in the series solution of stresses)

One can obtain stress field equations in terms of  $r, \theta$  by substituting Eq.(4.4) and Eq.(4.5) in Eq.(4.3) and expressing  $z$  in terms of  $r$  and  $\theta$ . However, the resulting equations are lengthy and can be found in reference 22.

Equation (4.3) is known as the Generalised Westergaard equation. The classical Westergaard equations are obtained by making  $Y(z)$  zero and Irwin's modified equations are obtained if the function  $Y(z)$  is taken to be a real constant.

Atluri and Kobayashi [2] in 1987 have reported the stress-field in series form explicitly. The stress field equations reported by them are compact and is elegant to use for devising least square algorithms for evaluating stress field parameters. The stress field for the mode I case is described as follows:

$$\begin{bmatrix} \sigma_x \\ \sigma_y \\ \tau_{xy} \end{bmatrix} = \sum_{n=1}^{\infty} \frac{n}{2} A_{In} r^{(n-2)/2} \begin{bmatrix} (2+(-1)^{n+\frac{n}{2}} \cos(\frac{n}{2}-1)\theta - (\frac{n}{2}-1) \cos(\frac{n}{2}-3)\theta) \\ (2-(-1)^{n-\frac{n}{2}} \cos(\frac{n}{2}-1)\theta + (\frac{n}{2}-1) \cos(\frac{n}{2}-3)\theta) \\ -((-1)^{n+\frac{n}{2}} \sin(\frac{n}{2}-1)\theta + (\frac{n}{2}-1) \sin(\frac{n}{2}-3)\theta) \end{bmatrix} \quad (4.6)$$

where  $A_{I1} = K_I / \sqrt{2\pi r}$ . (Note: In the original reference it is reported as  $K_I \sqrt{2\pi r}$  which is a typographical error) and  $4 A_{I2} = -\sigma_{ox}$ .

These equations have been applied to a practical mode I problem to test their validity and is discussed latter.

#### 4.5 Mixed Mode stress field equations :

Atluri and Kobayashi[2] also reported the stress-field equations for the mixed mode case. They are described as follows :

$$\begin{bmatrix} \sigma_x \\ \sigma_y \\ T_{xy} \end{bmatrix} = \sum_{n=1}^{\infty} \frac{n}{2} A_{In} r^{(n-2)/2} \begin{bmatrix} \left\{ 2 + (-1)^{n+\frac{n}{2}} \cos(\frac{n}{2}-1)\theta - (\frac{n}{2}-1) \cos(\frac{n}{2}-3)\theta \right\} \\ \left\{ 2 - (-1)^{n-\frac{n}{2}} \cos(\frac{n}{2}-1)\theta + (\frac{n}{2}-1) \cos(\frac{n}{2}-3)\theta \right\} \\ - \left\{ (-1)^{n+\frac{n}{2}} \sin(\frac{n}{2}-1)\theta + (\frac{n}{2}-1) \sin(\frac{n}{2}-3)\theta \right\} \end{bmatrix}$$
  

$$- \sum_{n=1}^{\infty} \frac{n}{2} A_{IIIn} r^{(n-2)/2} \begin{bmatrix} \left\{ 2 - (-1)^{n+\frac{n}{2}} \sin(\frac{n}{2}-1)\theta - (\frac{n}{2}-1) \sin(\frac{n}{2}-3)\theta \right\} \\ \left\{ 2 + (-1)^{n-\frac{n}{2}} \sin(\frac{n}{2}-1)\theta + (\frac{n}{2}-1) \sin(\frac{n}{2}-3)\theta \right\} \\ - \left\{ (-1)^{n-\frac{n}{2}} \cos(\frac{n}{2}-1)\theta - (\frac{n}{2}-1) \cos(\frac{n}{2}-3)\theta \right\} \end{bmatrix}$$

(4.7)

where  $A_{Ii} = K_I / \sqrt{2\pi r}$  and  $A_{IIi} = K_{II} / \sqrt{2\pi r}$ . (Note: In the original reference there was a typographical error in the  $\sigma_y$  term of the mode II series. The first term was a 'sin' term and the second term was denoted as a cos term. It was found in the course of present investigation that the second term must also be a 'sin' term. This was made possible with the help of graphics software which showed symmetry in fringes only when the term was changed to 'sin'. It was also counter checked by comparing the first term of the series solution to the singular solution reported in the literature.)

#### 4.6. Developments in SIF evaluation methodology

The Irwin's method for SIF extraction from photoelastic patterns was the accepted method for analysis for many years. In this method the positional co-ordinates and fringe order for a specific point that satisfies the criteria  $\partial\tau_m / \partial\theta = 0$  are used for evaluating  $K_I$  and  $\sigma_{ox}$ . Kobayashi and Bradley [23] modified the formulation, but fundamentally, the approach was unaltered. Since then several investigators reported various methods and Etheridge and Dally [24] reported a review on the relative accuracy of the various two-parameter methods. The review brought out the fact that the zone of data collection has to be very small of the order of  $r/a < 0.03$ .

Though photoelasticity gives whole field information, the previous reluctance to use information from the entire field stemmed primarily from practical limitations on data reduction. The positional co-ordinates of each data point used had to be measured manually and the results are calculated with the aid of a hand-held calculator or with a main-frame computer. This approach generally required manual data entry. With the introduction of small microcomputers and digitising tablets and the more recent PC based image processing, the drudgery of data reduction is removed [25].

Improvements in data collection methodology have lead to the development of several techniques to process the data from the field rather than restricting the analysis to a point (as in Irwin's method) or a few points along a specified line. Among the several methods [26] the over-deterministic approach of Sanford and Dally [27] has come to stay as the most useful technique for evaluating the SIF and  $\sigma_{ox}$ .

All the approaches described above share a common feature, namely that the analysis procedure used to extract the SIF from the full field fringe patterns relied on the near-field equations of fracture mechanics. In principle, the accuracy of these methods should improve as the region of data acquisition is reduced to smaller regions around the crack-tip. However, it is generally recognised and has been independently verified by several researchers [28,29] that the plane-stress assumption ceases to be valid in a small region at the crack-tip. In this region the stress field is three dimensional and experimental observations are influenced by stress gradients through the thickness. In addition, the stress field is altered by localized crack-tip blunting. On the other hand, if this region is excluded from the analysis, the region of data acquisition may not lie fully within the domain in which the inverse-square root singularity dominates the fringe pattern (Fig.4.2).

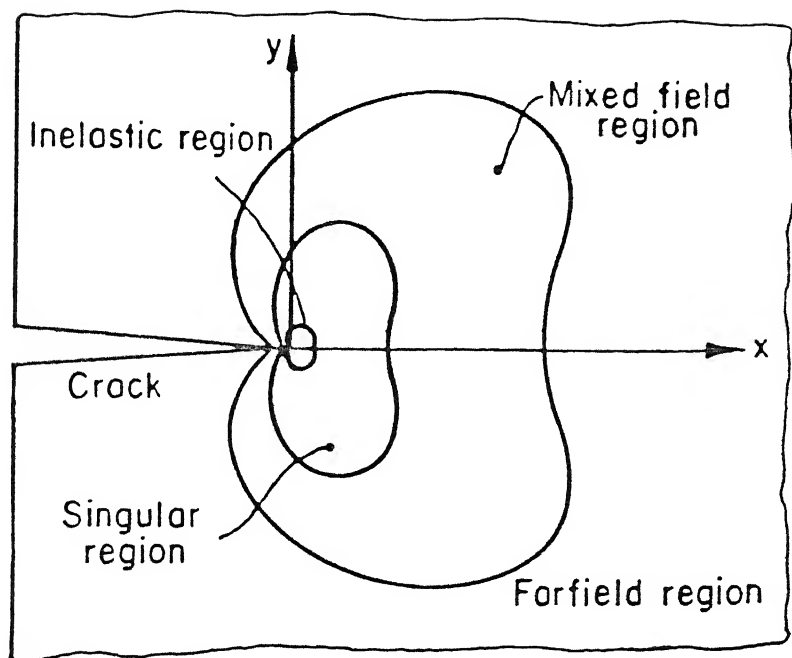


Fig. 4.2 Singular non singular and far field region around a crack tip.

The size and shape of the singularity dominated zone is an important factor to be determined and such studies[30,31] emphasized the fact that the singularity dominated zone is very small and indicated the use of a multi-parameter stress field equations for data reduction. The zone of data collection in such a case can be larger and one can collect data from the mixed field zone also (Fig.4.2).

#### 4.7. Evaluation of stress intensity factors using least square technique

Stress-optic law relates the fringe order N and the principal stress as

$$\frac{N F_\sigma}{t} = (\sigma_1 - \sigma_2) \quad (4.8)$$

where  $F_\sigma$  is the material fringe value and t is the model thickness. For a plane stress problem the principal stresses are,

$$\sigma_1, \sigma_2 = \frac{\sigma_x + \sigma_y}{2} \pm \sqrt{\frac{(\sigma_x - \sigma_y)^2}{4} + (\tau_{xy})^2} \quad (4.9)$$

Substituting Eq.(9) in Eq.(8), a function g is defined for the  $m^{th}$  data point as follows

$$g_m = \left\{ \frac{\sigma_x + \sigma_y}{2} \right\}_m^2 + (\tau_{xy})_m^2 - \left\{ \frac{N_m F_\sigma}{2t} \right\}^2 \quad (4.10)$$

If Eq.(4.7) is substituted in Eq.(4.10), then the Eq.(4.10) is non-linear in terms of the unknown  $A_{11}, A_{12}, \dots, A_{1k}, A_{III1}, A_{III2}, \dots, A_{III\ell}$ , where k is the number of mode I parameters and  $\ell$  is the number of mode II parameters considered.

If initial estimates are made for  $A_{11}, A_{12}, \dots, A_{Ik}, A_{III_1}, A_{III_2}, \dots, A_{III_l}$  and substituted in Eq.(4.10) it is possible that  $g_m \neq 0$  since the estimates may not be accurate. To correct the estimates, a series of iterative equations based on a Taylor series expansion of  $g_m$  is written as,

$$\begin{aligned} (g_m)_{i+1} &= (g_m)_i + \left(\frac{\partial g_m}{\partial A_{11}}\right)_i (\Delta A_{11})_i + \left(\frac{\partial g_m}{\partial A_{12}}\right)_i (\Delta A_{12})_i + \dots + \left(\frac{\partial g_m}{\partial A_{Ik}}\right)_i (\Delta A_{Ik})_i \\ &\quad + \left(\frac{\partial g_m}{\partial A_{III_1}}\right)_i (\Delta A_{III_1})_i + \left(\frac{\partial g_m}{\partial A_{III_2}}\right)_i (\Delta A_{III_2})_i + \dots + \left(\frac{\partial g_m}{\partial A_{III_l}}\right)_i (\Delta A_{III_l})_i \end{aligned} \quad (4.11)$$

where the subscript ' $i$ ' refers to the  $i^{\text{th}}$  iteration step and  $(\Delta A_{11})_i, (\Delta A_{12})_i, \dots, (\Delta A_{Ik})_i, (\Delta A_{III_1})_i, (\Delta A_{III_2})_i, \dots, (\Delta A_{III_l})_i$  denote the corrections to the previous estimates of  $(A_{11})_i, (A_{12})_i, \dots, (A_{Ik})_i, (A_{III_1})_i, (A_{III_2})_i, \dots, (A_{III_l})_i$ .

Corrections are determined such that  $(g_m)_{i+1} = 0$  and thus Eq.(11) gives

$$\begin{aligned} -(g_m)_i &= \left(\frac{\partial g_m}{\partial A_{11}}\right)_i (\Delta A_{11})_i + \left(\frac{\partial g_m}{\partial A_{12}}\right)_i (\Delta A_{12})_i + \dots + \left(\frac{\partial g_m}{\partial A_{Ik}}\right)_i (\Delta A_{Ik})_i + \\ &\quad \left(\frac{\partial g_m}{\partial A_{III_1}}\right)_i (\Delta A_{III_1})_i + \left(\frac{\partial g_m}{\partial A_{III_2}}\right)_i (\Delta A_{III_2})_i + \dots + \left(\frac{\partial g_m}{\partial A_{III_l}}\right)_i (\Delta A_{III_l})_i \end{aligned} \quad (4.12)$$

Applying this iteration scheme to  $M$  ( $M > k + l$ ) data points results in an overdetermined set of linear equations in terms of the unknown corrections  $(\Delta A_{11})_i, (\Delta A_{12})_i, \dots, (\Delta A_{Ik})_i, (\Delta A_{III_1})_i, (\Delta A_{III_2})_i, \dots, (\Delta A_{III_l})_i$  given in the matrix form by,

$$(g)_i = -[b]_i \{ \Delta A \}_i \quad (4.13)$$

$$\{g\}_i = \begin{bmatrix} g_1 \\ g_2 \\ \vdots \\ g_k \\ \vdots \\ g_{k+l} \end{bmatrix}_i \quad (4.14)$$

and

$$[b]_i = \begin{bmatrix} \partial g_1 / \partial A_{I1} & \partial g_1 / \partial A_{I2} & \dots & \partial g_1 / \partial A_{Ik} & \partial g_1 / \partial A_{II1} & \partial g_1 / \partial A_{II2} & \dots & \partial g_1 / \partial A_{IIIl} \\ \partial g_2 / \partial A_{I1} & \partial g_2 / \partial A_{I2} & \dots & \partial g_2 / \partial A_{Ik} & \partial g_2 / \partial A_{II1} & \partial g_2 / \partial A_{II2} & \dots & \partial g_2 / \partial A_{IIIl} \\ \vdots & \vdots & & \vdots & \vdots & \vdots & & \vdots \\ \vdots & \vdots & & \vdots & \vdots & \vdots & & \vdots \\ \partial g_M / \partial A_{I1} & \partial g_M / \partial A_{I2} & \dots & \partial g_M / \partial A_{Ik} & \partial g_M / \partial A_{II1} & \partial g_M / \partial A_{II2} & \dots & \partial g_M / \partial A_{IIIl} \end{bmatrix}_i \quad (4.15)$$

and

$$\{\Delta A\}_i = \begin{bmatrix} \Delta A_{I1} \\ \Delta A_{I2} \\ \vdots \\ \Delta A_{Ik} \\ \Delta A_{II1} \\ \Delta A_{II2} \\ \vdots \\ \Delta A_{IIIl} \end{bmatrix}_i \quad (4.16)$$

In forming the Eq.(4.13) one needs to calculate  $(\partial g_i / \partial A_{I1}), (\partial g_i / \partial A_{I2}) \dots$  etc. and at first it appears that it may be difficult to do it. However, one can determine them very easily as follows. A typical derivative for the  $m^{\text{th}}$  data point with respect to  $A_{In}$  is obtained by taking the derivative of Eq.(4.11).

$$\frac{\partial g_m}{\partial A_{In}} = \frac{1}{2} (\sigma_x - \sigma_y)_m \left\{ \frac{\partial \sigma_x}{\partial A_{In}} - \frac{\partial \sigma_y}{\partial A_{In}} \right\}_m + 2 \left( \tau_{xy} \frac{\partial \tau_{xy}}{\partial A_{In}} \right)_m \quad (4.17)$$

Since,  $A_{In}$  is a linear coefficient, the term  $\frac{\partial \sigma_x}{\partial A_{In}}$  etc, in Eq.(4.17) are simply the terms shown in the column vector of Eq.(4.7) multiplied by  $(\frac{n}{2} r^{(n-2)/2})$ . Thus,  $\frac{\partial g_m}{\partial A_{In}}$  can be determined in a closed form way.

Now  $\{\Delta A\}_t$  can be determined in a least square sense from Eq.(4.13) as,

$$\{\Delta A\}_t = [c]_t^{-1} \{d\}_t \quad (4.18)$$

where

$$[c]_t = [b]_t^T [b]_t$$

$$\{d\}_t = [b]_t^T \{g\}_t \quad (4.19)$$

The solution to the Eq.(4.19) gives  $(\Delta A_{I1})_t, (\Delta A_{I2})_t, \dots, (\Delta A_{Ik})_t, (\Delta A_{II1})_t, (\Delta A_{II2})_t, \dots, (\Delta A_{IIl})_t$  which are used to improve the estimates of  $(A_{I1})_t, (A_{I2})_t, \dots, (A_{Ik})_t, (A_{II1})_t, (A_{II2})_t, \dots, (A_{IIl})_t$  for the next iteration by

$$\begin{aligned} (A_{I1})_{t+1} &= (A_{I1})_t + (\Delta A_{I1})_t \\ (A_{I2})_{t+1} &= (A_{I2})_t + (\Delta A_{I2})_t \\ &\vdots &&\vdots \\ &\vdots &&\vdots \\ (A_{Ik})_{t+1} &= (A_{Ik})_t + (\Delta A_{Ik})_t \\ (A_{II1})_{t+1} &= (A_{II1})_t + (\Delta A_{II1})_t \\ (A_{II2})_{t+1} &= (A_{II2})_t + (\Delta A_{II2})_t \\ &\vdots &&\vdots \\ &\vdots &&\vdots \\ (A_{IIl})_{t+1} &= (A_{IIl})_t + (\Delta A_{IIl})_t \end{aligned} \quad (4.20)$$

The Convergence can be decided by either of the two following criteria, namely (1) the parameter error minimization and (2) the fringe order error minimization.

In the parameter error minimization the iterations are stopped when the values of  $(\Delta A_{11})_t$ ,  $(\Delta A_{12})_t$ , ...,  $(\Delta A_{1k})_t$ ,  $(\Delta A_{21})_t$ ,  $(\Delta A_{22})_t$ , ...,  $(\Delta A_{2k})_t$  become reasonably small ( say of the order of  $10^{-6}$ ). In the fringe order error minimization, using the newly calculated values of  $(A_{11})_{t+1}$ ,  $(A_{12})_{t+1}$ , ...,  $(A_{1k})_{t+1}$ ,  $(A_{21})_{t+1}$ ,  $(A_{22})_{t+1}$ , ...,  $(A_{2k})_{t+1}$  the fringe orders corresponding to the selected data points are calculated theoretically during every iteration step and are compared with the experimentally obtained fringe orders. The convergence criteria is satisfied if ,

$$|(N_{\text{theory}} - N_{\text{exp}})| \leq \text{Convergence error.} \quad (4.21)$$

The convergence error is usually of the order of 0.05 to 0.1.

A software has been implemented on the PC-386 environment in Turbo Pascal for the least square analysis and the theoretical reconstruction using upto 13 terms each of model I and mode II of the Atluri and Kobayashi[2] form of the stress field equations. The software requires the data file containing the X,Y coordinates and the fringe order, Converts the data in real world coordinates, using the data preprocessor, then the least square procedure is invoked and the results are written to another data file. Using these parameters the program recalculates  $(\sigma_1 - \sigma_2)$  values and hence the fringe order for every point in the data field. The fringes are then plotted using the graphics utilities of the Pascal environment.

#### 4.8. Performance for a mode I crack problem

Figure 4.3 shows the isochromatics observed in an annular ring subjected to internal pressure with cracks emanating radially from the outer boundary.

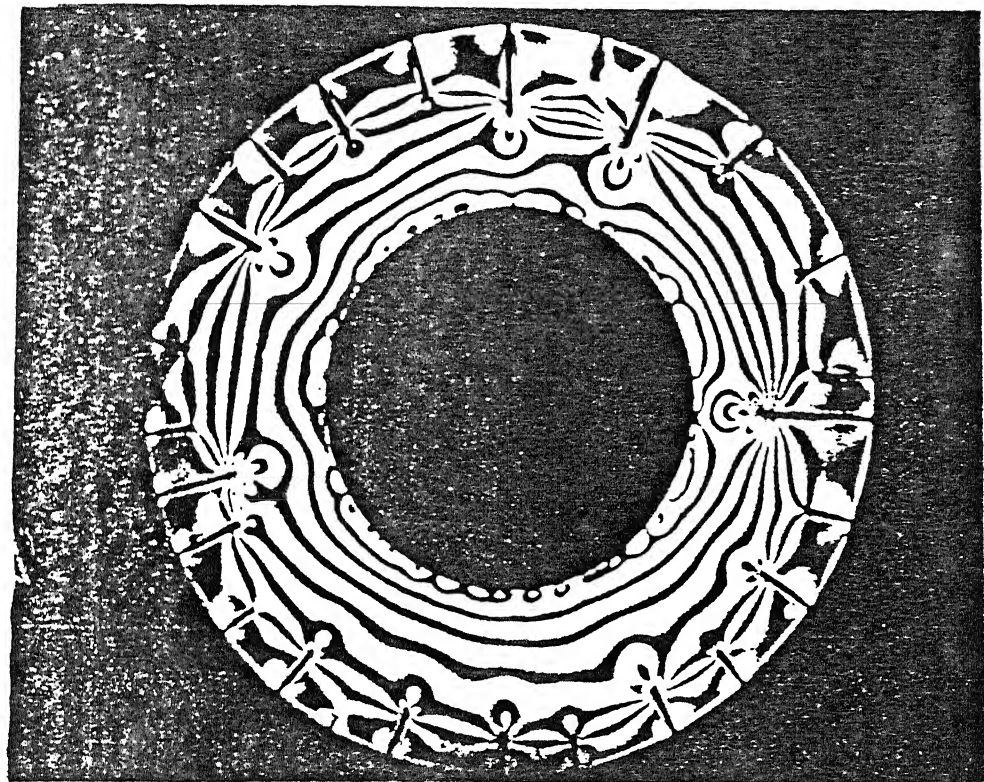


Fig. 4.3 Isochromatic fringe pattern obtained for an annular ring subjected to internal pressure with cracks emanating from the outer boundary.

The fringe patterns observed close to the crack-tip are similar to the one observed in MCT specimen for large crack lengths. This example shows that this feature is due to a combination of two aspects namely the finite dimensions of the specimen and also due to the fact that the crack is lying in a zone of stress gradient.

A least square analysis is carried out to determine the minimum number of terms required to model the stress field accurately.

The minimum number of data points required for the least square algorithm to work satisfactorily [32] is given by

$$M = 2(k + \ell) + 2$$

where  $k$  and  $\ell$  are the number of Mode I and Mode II terms and  $M$  is the number of data points. Sixty five data points were collected from the sketetonized fringe pattern using the inhouse developed software. The points were selected so as to represent the full characteristics of the data field, i.e. Depending on the size of the fringe, equally spaced data points were collected from the field. The points selected are also skewed with reference to the X axis. This ensures that the least square equations do not become ill conditioned.

The convergence criteria selected is the fringe order error minimization. The parameter values are resubstituted in the equations and the isochromatic fringe pattern is theoretically reconstructed. This is compared with the actual fringe pattern by echoing back the data points collected for the analysis. The analysis is performed using upto 8 terms of the series solution and the results are as shown in Fig.4.4.

Figure 4.5. shows the graph of the cumulative percentage error in fringe order with the number of terms of the least square solution.

The percentage error for the 2 term and the 3 term solution is about 24%.

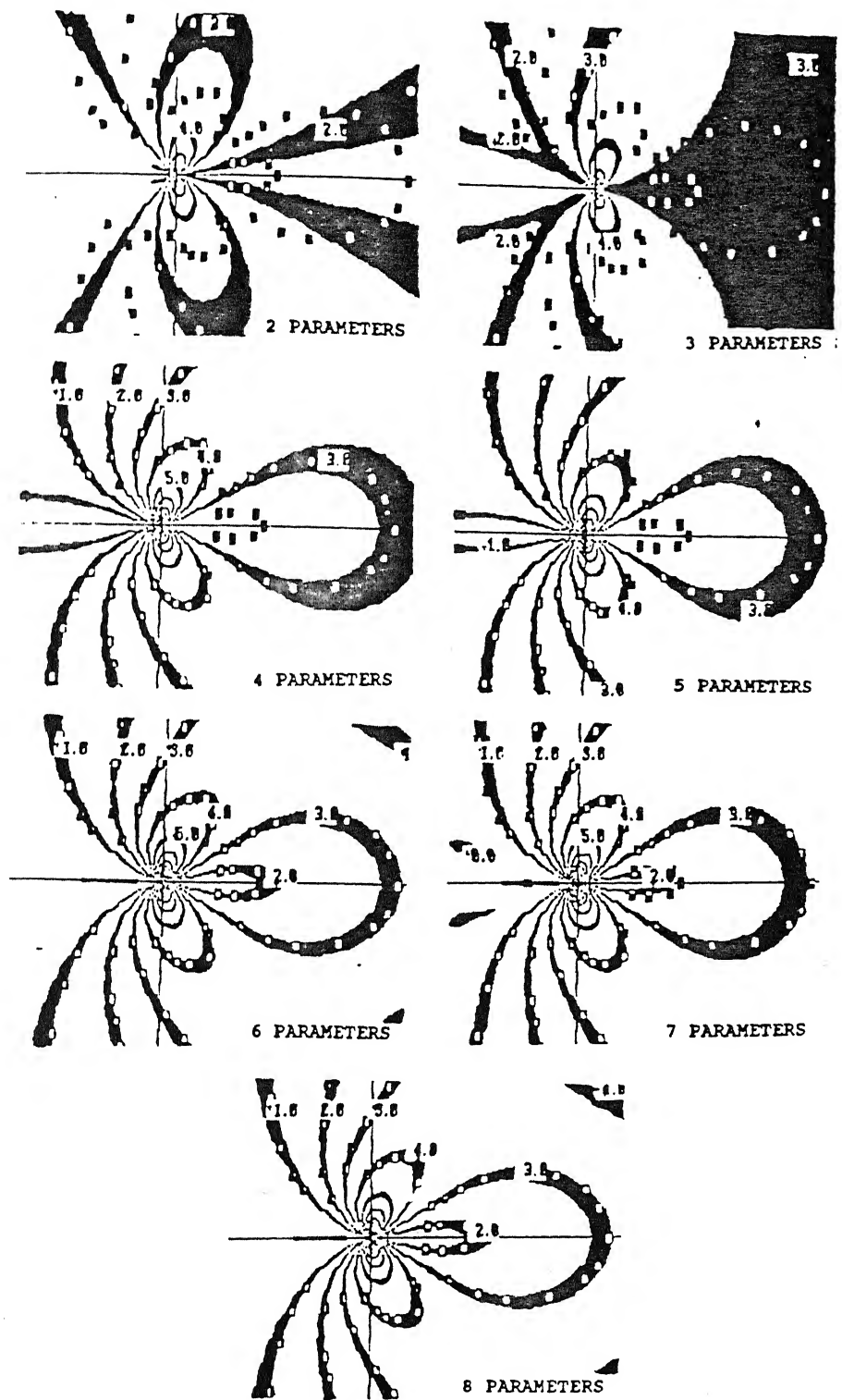


Fig. 4.4 Reconstructed fringe pattern for the mode I problem using different number of terms of the Atluri's stress field series solution.

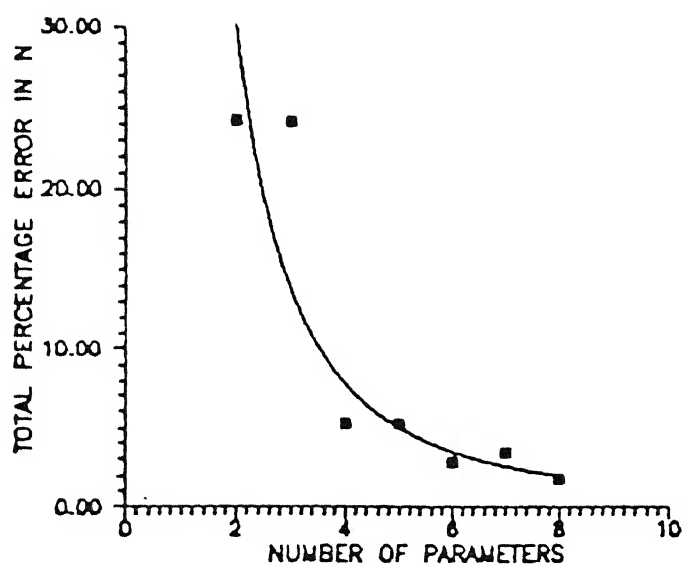


Fig. 4.5 Graph of cumulative percentage error v/s number of terms of the series solution.

The parameter values are not able to simulate the general stress field. This is obvious, since the first 2 terms are valid only for the singularity region and not for the general stress field.

With the inclusion of the fourth and the fifth term, the accuracy of the solution improves drastically. The total percentage error in the fringe order comes down to about 6%. The series solution is able to model the general stress field with a better accuracy, however it is still not able to model the inner frontal loop.

The solution stabilizes for 6 or more terms in the series solution. The percentage error in the fringe order drops to about 2 percentage. The stress field is modelled accurately. Beyond 6 terms the accuracy improves only slightly. The 8 term solution is the best one for this class of fringe pattern. The computational effort required for a least square solution increases in the order of the square of the number of parameters used. Hence the computational time required increases drastically as the number of terms increases.

Figure 4.6. shows that the KI value stabilizes with the increasing number of terms used. Figure 4.6 also shows the variation of the other coefficients of the stress field equations as a function of the number of parameters.

#### 4.9. Closure :

In this chapter the use of the equations proposed by Atluri and Kobayashi [2] for evaluating the stress field parameters in Fracture Mechanics problems is discussed. An overdeterministic method for evaluating stress field parameters in a mixed mode situation is then presented. The result obtained shows that the program is validated for solving a Mode I situation. In the next chapter the use of the above methodology for evaluating stress field parameters for a mixed-mode situation is discussed.

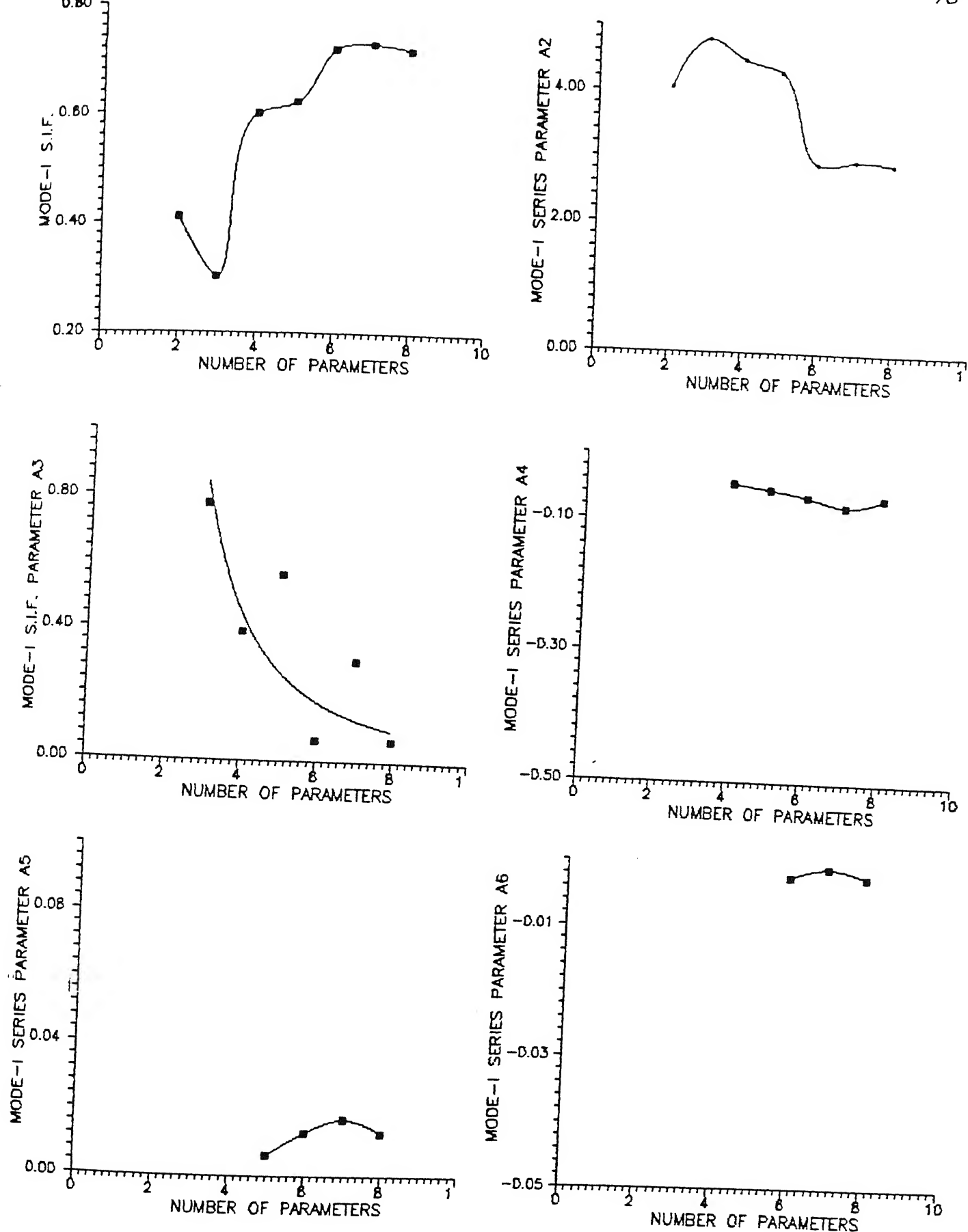


Fig. 4.6 Graph showing variation of mode I parameters for series solution using different number of terms.

## CHAPTER 5

### EVALUATION OF STRESS FIELD PARAMETERS IN THE NEIGHBORHOOD OF A CRACK LOCATED IN THE TENSILE FILLET OF A SPUR GEAR.

#### 5.1 Introduction

Gear is one of the most important and most widely used machine element. The gear tooth failure commonly occurs due to fracture initiated due to a fatigue crack at the tooth fillet. There could be several microscopic flaws during manufacturing or developed during the actual service conditions. They grow in size during the operation and can reach critical size, leading to failure. The effect of the flaw on the overall strength of the machine element has to be evaluated. If the stress field around the crack is known then using the principles of fracture mechanics one can evaluate the residual life of the gear or the reduced load to prevent crack propagation.

There has been only a limited study in the literature in analysing the stress field in the neighborhood of a crack at a tensile fillet of a spur gear. Honda and Conway [33] attempted to study this problem using the Finite Element Technique. They modelled only one gear tooth, assuming that it is rigidly fixed to the gear hub. They observed that the stress field is a combination of both mode I and mode II loadings. They evaluated the S.I.F for various positions of load application points from the addendum side to the dedendum side.

There has been no experimental verification of the results reported by Honda and Conway [33]. They basically analysed only one gear tooth since modelling the entire gear is difficult from the memory requirement point of view unless the concept such as cyclic symmetry is invoked. The analysis can be considered realistic only if it incorporates the loading due to assembly and the interaction of adjacent gear teeth. Photoelastic analysis has certain advantages in terms of the accuracy in simulation of the actual loads occurring on the model, like the clamping load, the hub stiffness etc.

In the previous chapter the use of the equations proposed by Atluri and Kobayashi [2] for evaluating the stress field parameters in Fracture Mechanics problems were discussed. In this chapter the application of these equations to the mixed mode crack problem is presented.

## 5.2 Experimental details

Photograph in Fig.5.1.a shows a view of the loading fixture as mounted on the loading frame of the polariscope during the experiment. Figure 5.1.b shows the closeup view of the loading arrangement. The gear loading frame comprises of two shafts with a variable center to center distance. The top shaft is set by means of the protractor scale attached on it and rigidly clamped at the required position. The alignment of the shafts is adjusted by means of the spherical washers and the locating strip [34]. The prime objective of the alignment is to maintain the loaded gears in the same plane every time they are loaded. When the axes of the two gears are exactly parallel, then the locating strip moves freely in the guide block. The gears are keyed to the shaft and clamped by means of lock nuts. The bottom shaft is free to rotate in its housing. To the other end of the bottom shaft is keyed a pulley. A wire rope is wound over it and to the other end of the wire rope is attached a pan. Suitable load is applied using this arrangement.

A pair of spur gears made from a precast sheet of Araldite sheet of thickness 6.26 mm having the following properties is used :

Modulus of Elasticity,  $E$  = 2.6 GPa

Poisson ratio,  $\nu$  = 0.33

Spur gears are cut with the following specifications :

Pressure Angle =  $14.5^\circ$

Diametral Pitch = 6

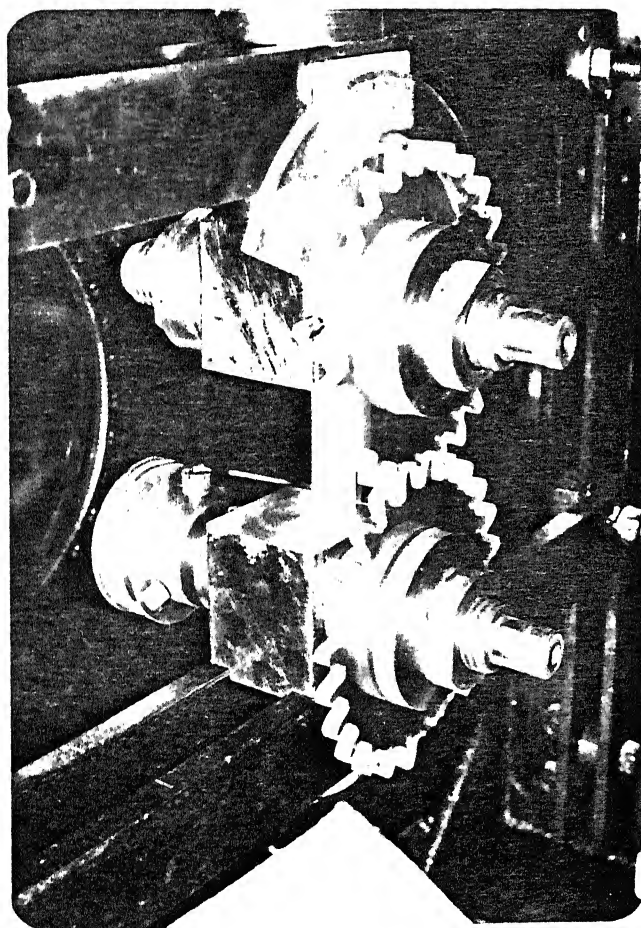
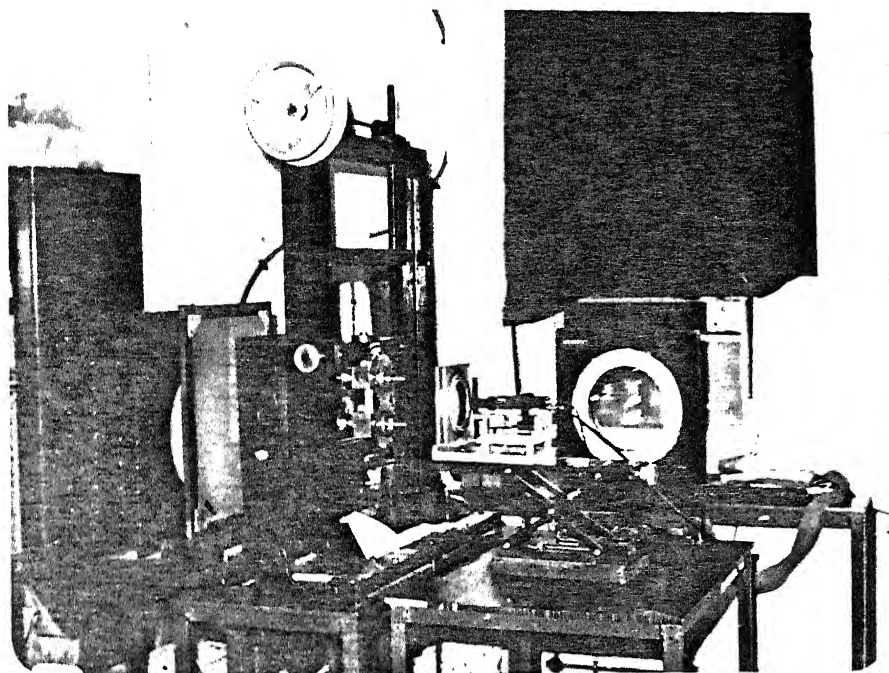


Fig. 5.1.b Closeup view of the gear loading frame.

(Module	= 4.3333 mm)
Gear Ratio	= 1
Number of teeth	= 24
Axial face width	= 6.26 mm

### 5.3 Selection of the crack location

In the S.I.F. analysis of the crack at the tensile fillet of the gear tooth using Finite Element Method, Honda and Conway[33] reported that the crack tip had been selected at the highest stressed point in the tensile fillet region of the gear tooth. To identify this point they obtained the stress field in the fillet area initially. Following a similar approach isochromatics are recorded for the gear tooth fillet using photoelasticity. It can be seen clearly from photograph in Fig. 5.2 that the isochromatics faithfully follow the fillet contour. In other words, the value of the maximum shear stress is almost a constant along the entire fillet. Thus there is no specific point along the fillet, where there is maximum stress. In a sense spur gear is designed with a contoured fillet which is good from service point of view. The mid point of the fillet is chosen as a probable location for a crack. A thin slot of 1.26 mm long, and 0.1 mm thick is cut simulating a crack at this point normal to the surface.

### 5.4 Fringe ordering

The fringe ordering is a difficult procedure in this case because of the complexity of the stress field. The time derivative of the load and the colour code are used as criteria for the fringe ordering (section 3.2.2). The fringe patterns are recorded and the direction of the motion of the fringes is studied as the load is increased to determine the fringe ordering. Figure 5.3 shows the photograph of the fringe patterns for different loads under monochromatic and white light sources.

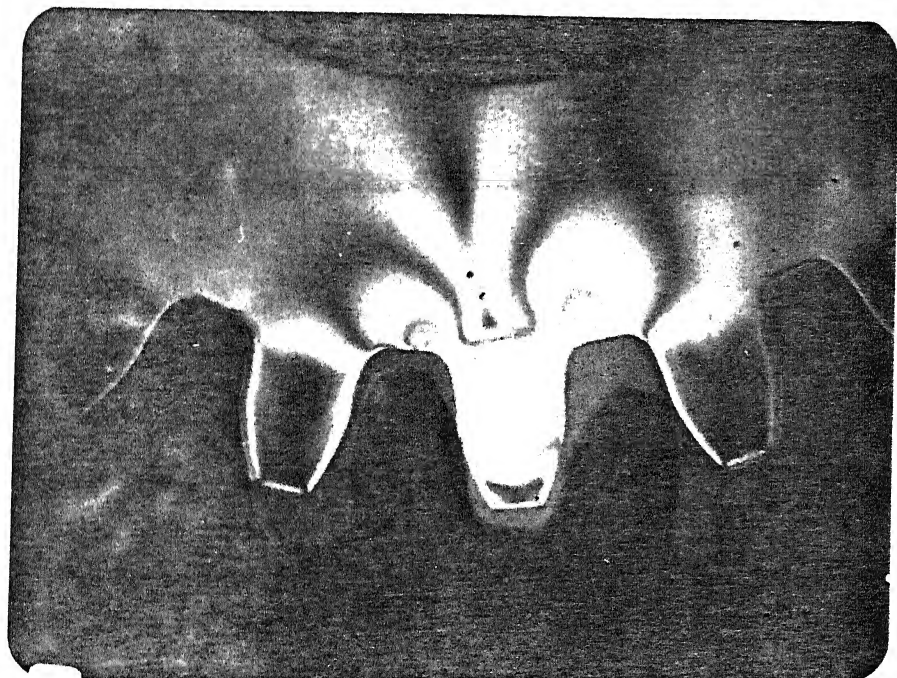
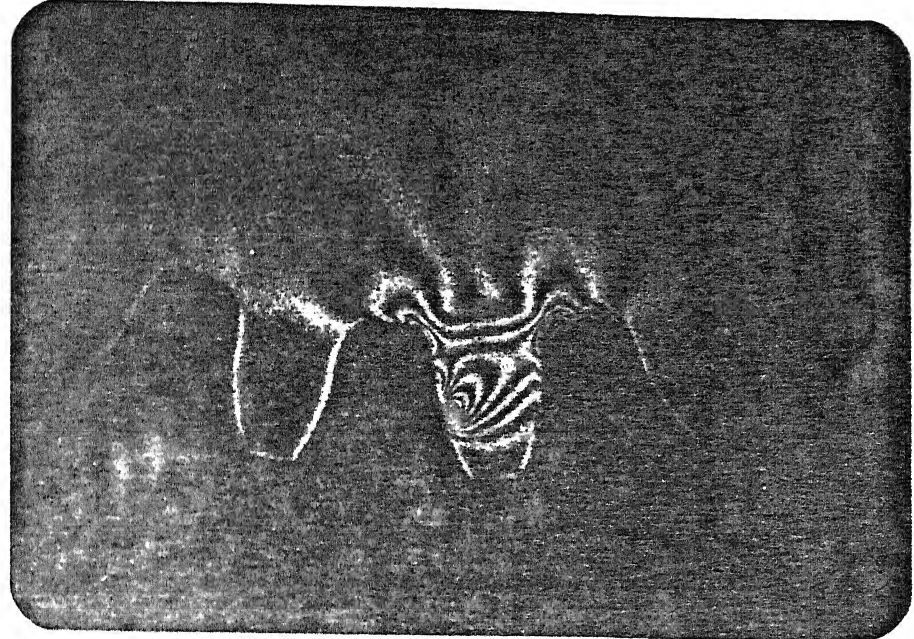


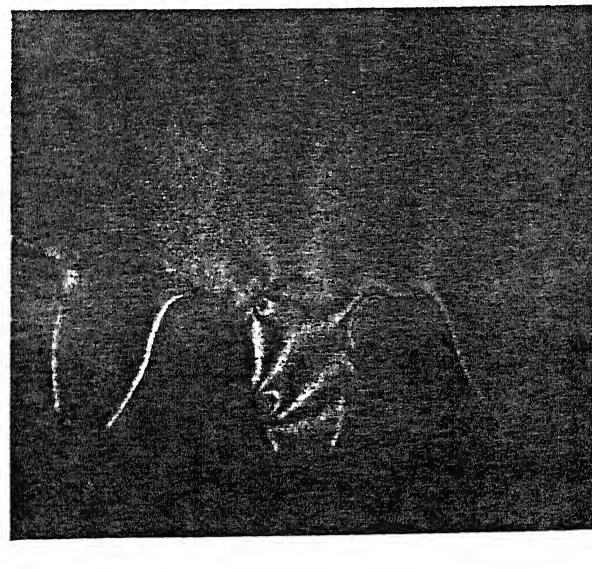
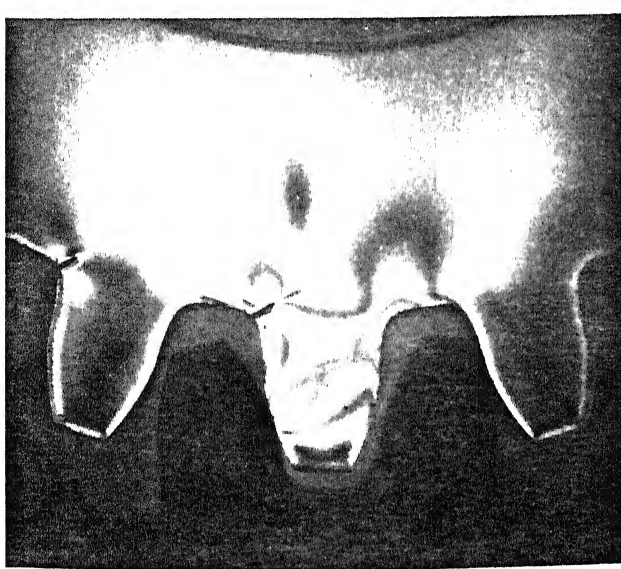
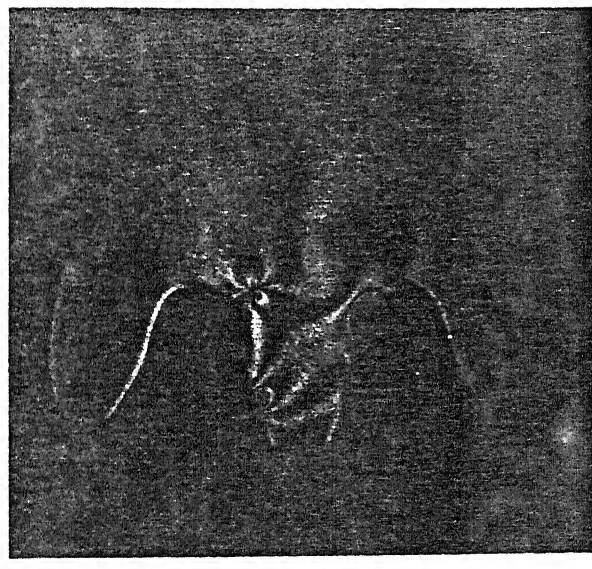
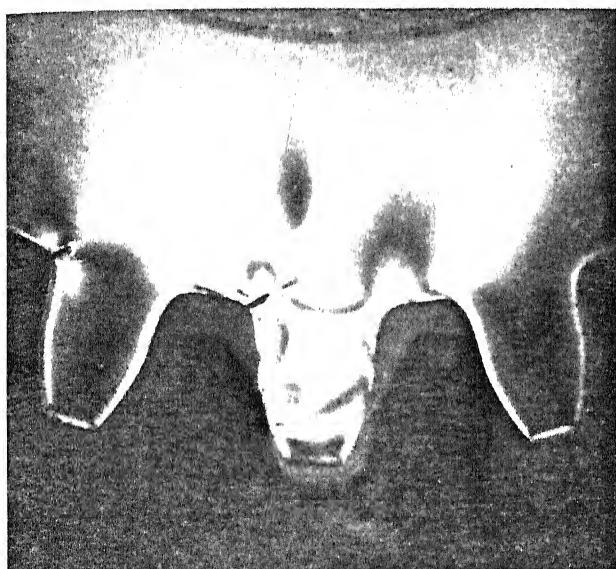
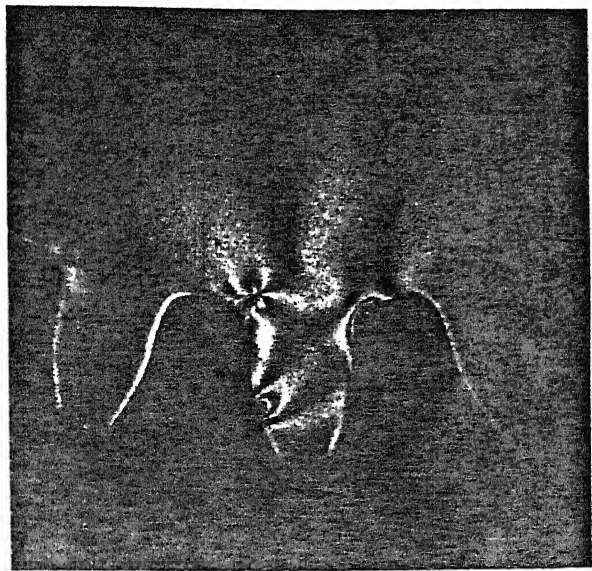
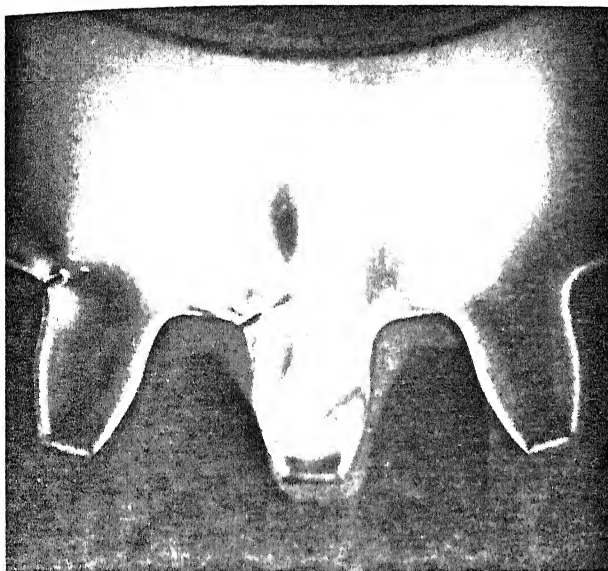
Fig. 5.2 Isochromatic Fringe pattern of a gear tooth under monochromatic and white light.

The colour code specifies that the fringe that is black is a zeroth order fringe. Fringe orders 1, 2 etc are identified as red-blue and red-green transitions. The second order is identified by pinkish red and the third order is identified by orange red. These colours are easily identifiable when the isochromatic fringe field is recorded using white light. The corresponding pictures taken using a monochromatic source ( Sodium Vapour ) shows the fringes as black along the red-blue and the red-green transition zone.

The gear tooth is subjected to cantilever loading, hence the lower end, beyond the loading point remains unstressed i.e. the fringe at the outer boundary of the gear tooth is a zeroth fringe order. As we move towards the base of the tooth, a source exists at the loading point. The stress value increases hence the fringes are ordered in a successively increasing order. As we move further down the loading point, the stress value decreases. The crack-tip acts as a source and in its neighborhood the fringes have to be ordered appropriately.

The fringes around the crack tip present some unique features. When observed in a monochromatic light source, a fringe is seen just ahead of the crack tip, along the crack direction (Fig. 5.3). The time derivative photographs are taken at loads of 10 Kg, 12 Kg, 15 Kg, 18 Kg, 20 Kg and 30 Kg respectively. The fringe ahead of the crack initially has a fringe order zero which is corroborated by the colour code (Fig.5.3). As the load is increased, the fringe becomes shorter in length. In the photograph obtained using a monochromatic light source, the end of the fringe becomes progressively brighter and finally merges with the background (Fig.5.3). In the white light image, it can be seen that the fringe has red-blue transition as in fringe order one and gradually changes its colour.

At the crack-tip due to the high stress gradient it is difficult to see whether the fringe has red-blue transition or it is black. Hence, there is ambiguity in ordering this particular fringe. This ambiguity is appropriately taken care of in the analysis. Except, this fringe, all other fringes are uniquely ordered.



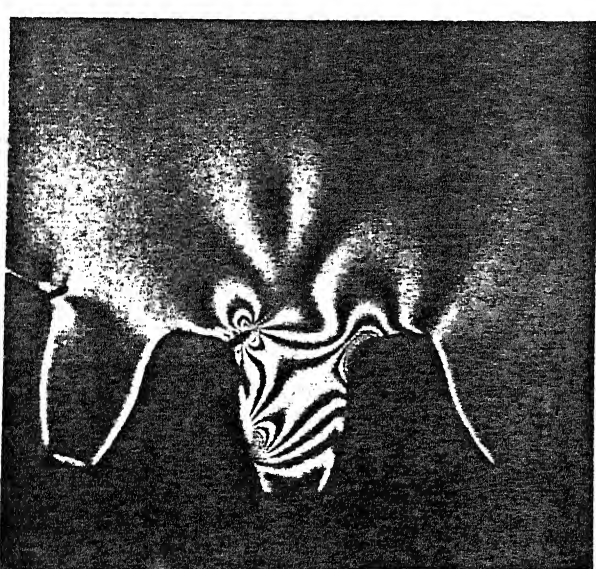
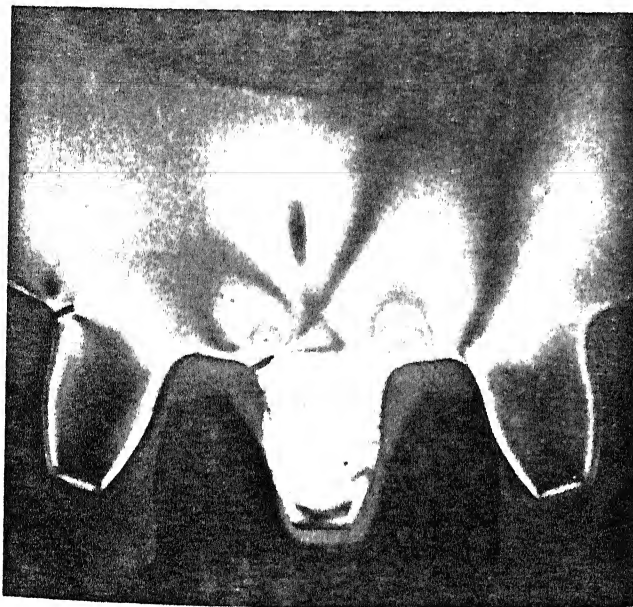
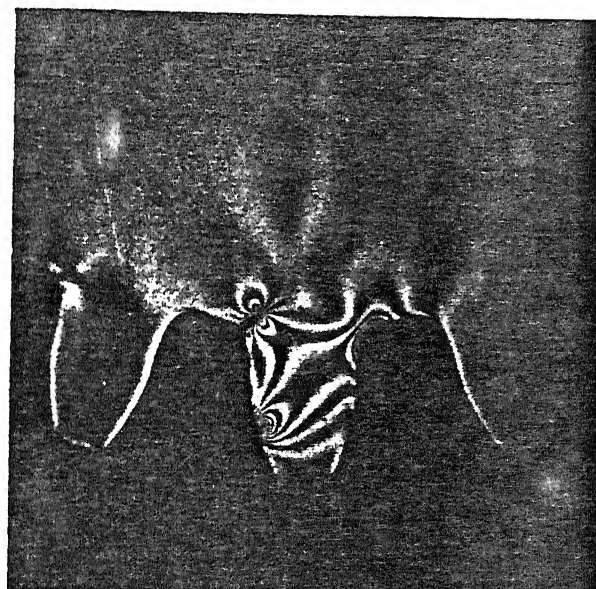
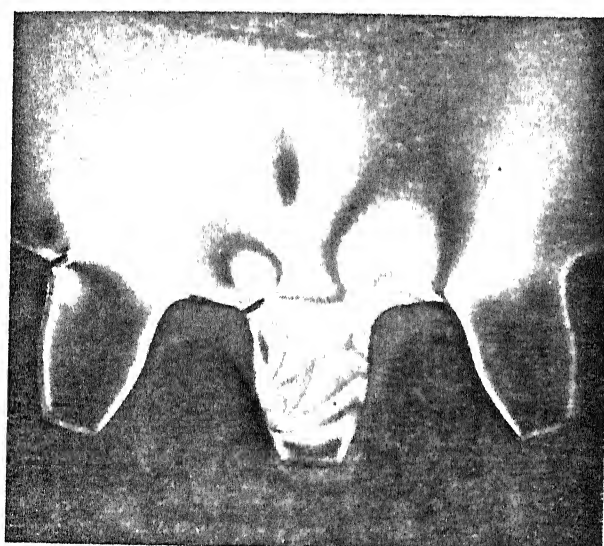
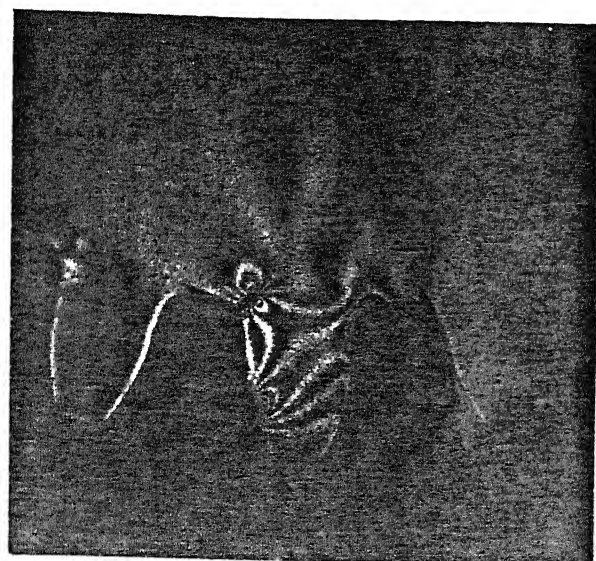
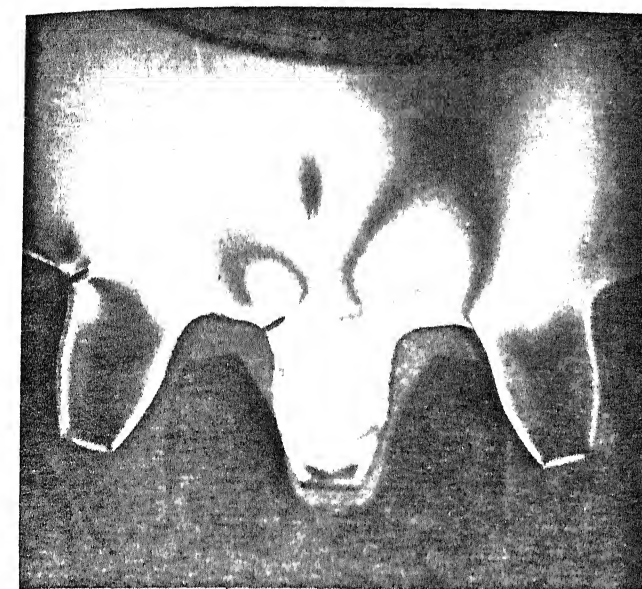


Fig. 5.3 Isochromatic fringe patterns of the spur gear tooth with a crack at its tensile fillet, for increasing load, under monochromatic and white light source.

The fringe ordering at the crack-tip is difficult because of two reasons. For cracks in structures of finite geometry, a "sink" is observed ahead of the crack (Fig.3.5). In the present example, apart from this, while going from tensile to compressive fillet the fringe order have to go through zero. These two features interact in a complex way as the loading is gradually increased.

### 5.5 S.I.F evaluation for the crack

The first step in any photoelastic analysis is calibration of the material fringe constant. Using the completely automated procedure developed for calibration of a photoelastic material using a circular disk under diametral compression, as described in section 3.7 the analysis was performed and the material fringe constant was found to be 14.735 N/mm/fringe.

Referring figure 5.3 it can be seen that the isochromatic loops of same order above and below the crack have different sizes, which is a distinguishing feature that the loading at the crack is of mixed mode in nature. Several factors like the tooth geometry, the position of the contact point relative to the crack also affect the isochromatic fringe pattern around the crack. The S.I.F analysis is carried out for the gear problem for load value of 30 kg using the Atluri and Kobayashi[2] stress field equations as discussed in the previous chapter.

Seventy five data points were selected, equally distributed to represent every geometric feature of the fringe pattern.

#### 5.5.1 Data processing

The raw data provided by the data collection software has to be processed to transform it from the screen coordinates to real world coordinates. This is achieved using the following procedure

The aspect ratio of the MVP-AT screen has to be determined initially since the horizontal and vertical pixel scaling is not the same. Using the calibration images of a vernier caliper, the magnification in terms of pixels/mm is determined for both the X and the Y direction. It should be noted that this magnification is not the scaling factor of the real world model but scaling factor with respect to the pixel size of the screen. For the current settings of the monitor the aspect ratio is 0.6818.

For the purpose of analysis, the positional coordinates of various points have to be determined with the crack axis as X axis and the crack-tip as the origin.

1. Translation : Depending on the location of the crack tip on the screen, the origin has to be shifted from the current screen origin ( left hand top corner ) to the crack tip. In order to change the orientation of the Y axis, the Y coordinates are multiplied by (-1).

$$\begin{aligned}x_1 &= x - x_o \\y_1 &= -(y - y_o)\end{aligned}$$

2. Scaling : After the origin is shifted to the crack-tip position, the Y coordinates have to be multiplied by the aspect ratio in order to obtain the real world distances.

$$y_2 = 0.6818 y_1$$

Also the image is a magnified one depending on the type of lens used. The crack tip image is recorder using the macro lens. This lens has a high magnification and 30 pixels in the X direction represent 1 mm.

The X and Y coordinates have to be scaled to find the real world coordinates.

3. Rotation : The crack tip is not located along the positive X axis.

The stress field equations assume the crack tip to be along the X direction. Hence the data points have to be rotated to align the crack tip with the X direction. The angle of rotation is determined by the data collection software. In this case the angle was found to be  $28.777^{\circ}$ .

The transformed data available from these transformations is written to a data file. This file contains the real world X and Y coordinates and the fringe order N corresponding to each of the selected points. This data is used by the least square software to determine the S.I.F parameters.

### 5.6 Experimental Results

The accuracy of any experimental analysis depends upon the accuracy of the measurement of the variables. In this case these variables are the exact positional coordinates of the data point, the location of the origin i.e. the crack-tip, the value of the angle of orientation of the crack and the magnification. The accuracy in the positional coordinates of the data points and the origin is taken care of by the fringe thinning algorithm. A software has been developed to measure the angle accurately. It uses human judgment for the purpose of locating the crack direction. Two points, the base and the tip of the crack are selected interactively, and the line joining the 2 points and extending beyond, is displayed and the  $\theta$  value is calculated.

The least square analysis is then performed on the data collected from the processed fringe pattern. The convergence criteria selected is the fringe order error minimization. The parameter values are resubstituted in the equations and the isochromatic fringe pattern is theoretically reconstructed. This is compared with the actual fringe pattern by echoing back the data points collected for the analysis. The analysis is performed using upto 6 terms of mode I and 6 terms of mode II series solution and the results are as shown in Fig.5.4.a

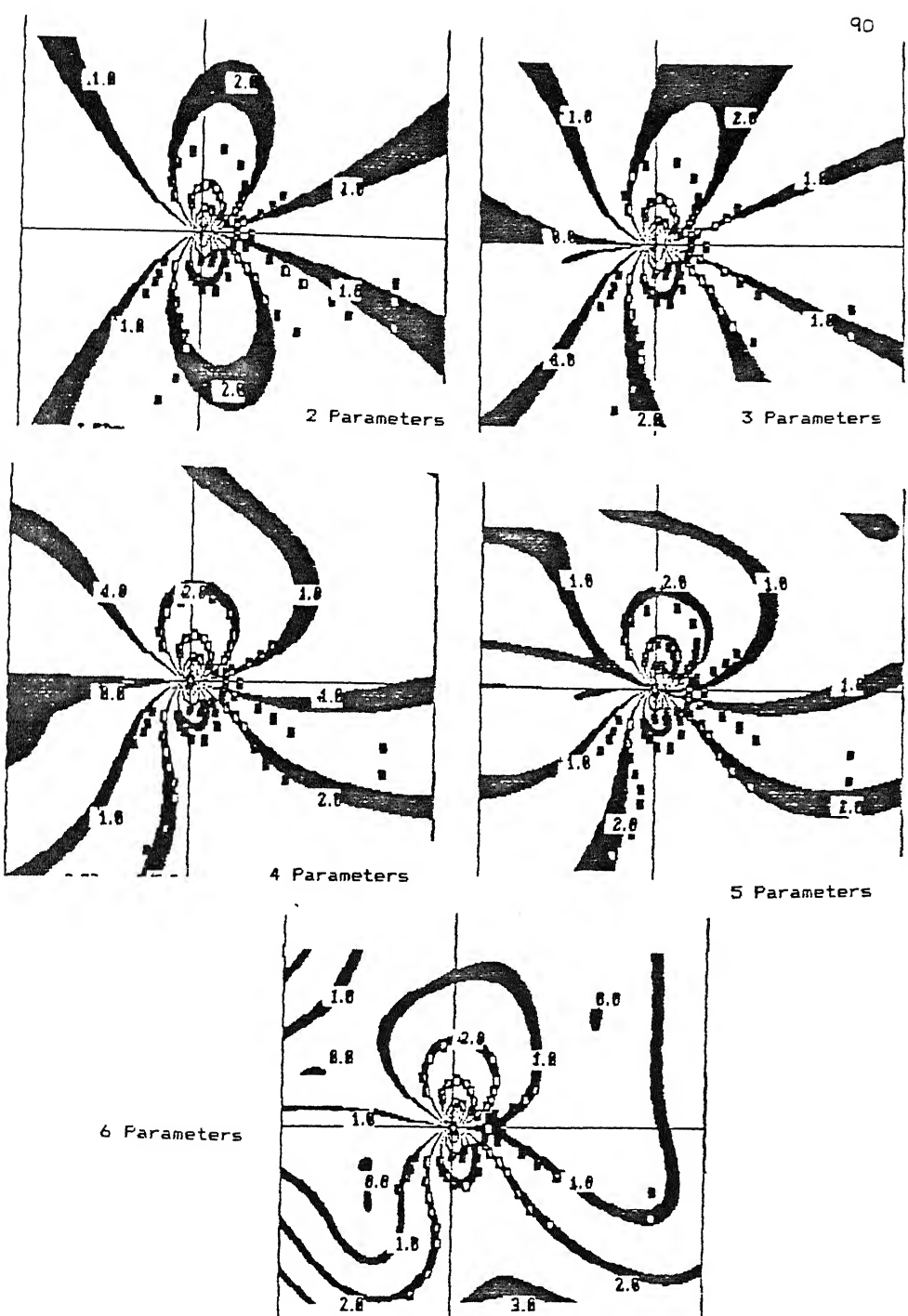
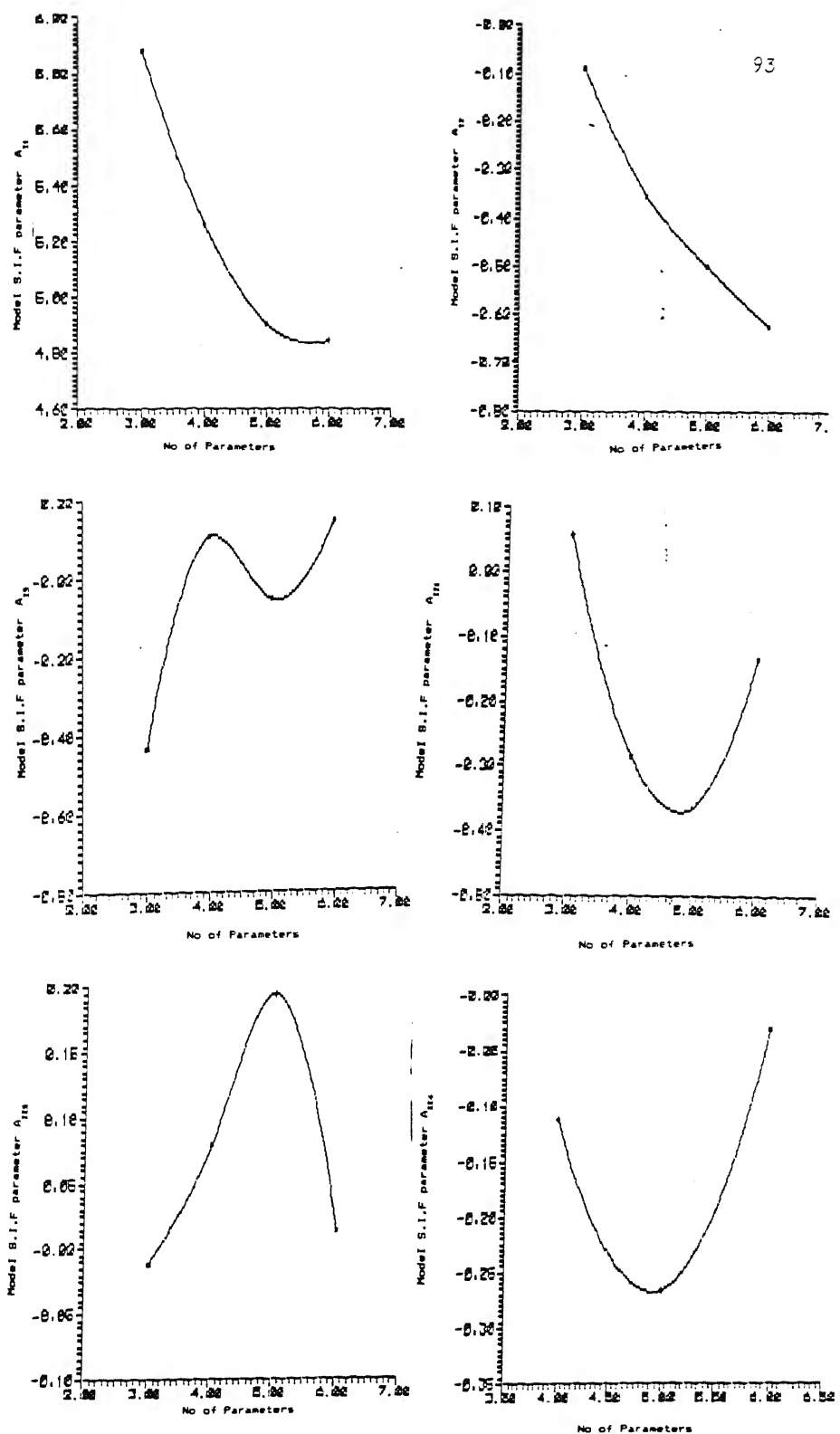


Fig. 5.4 Reconstructed fringe pattern with the data points echoed back for the leastsquare analysis using increasing number of terms of the series solution.

A sample least square analysis output file is shown in appendix 3. The accuracy of the series solution is clearly brought out in the appropriately scaled view of the actual fringe field and the reconstructed fringe pattern as shown in Fig. 5.4.b. The cumulative percentage error in the fringe orders v/s the number of terms of the series solution is shown in graph in Fig.5.4.c.

### 5.7 Closure

Analysis was carried out for addendum side contact of the gear tooth, to find out the optimum number of terms for convergence. The criteria for selection of the data points was also discussed. The results show that, an higher order solution can faithfully model the stress field in this case if appropriate number of terms are used. The success of the analysis of the present example provides enough confidence to apply photoelasticity to evaluate fracture parameters for complex real-life problems.



## CONCLUSIONS AND SUGGESTIONS FOR FURTHER WORK

Optical methods in stress analysis have the advantage of providing the whole field information of the entire field. A wealth of information is provided in the form of fringes. The fringes appear in general as bands and the first step in analysis is the identification of exact fringe location. With the development of Digital Image Processing (D.I.P) techniques, sophisticated algorithms are available to extract the fringe skeleton. Quantitative information can be obtained only if the positional coordinates of various points along with their corresponding fringe orders are known. The critical problem of the ordering of the fringes and the data collection effectively remained a manual one. An attempt has been made in this thesis to overcome this bottleneck and have complete automation for the photoelastic experimental analysis.

Fringe skeletons are extracted using the algorithm of Ramesh and Pramod. The software that was implemented in the PIP environment by Ramesh and Pramod was converted to MVP-AT environment in the course of this thesis. The fringe thinning algorithm scans the image along particular directions and marks all the fringe points. However it cannot recognize a particular fringe as a continuous one since, in the computer representation, the fringes are just a group of points without any particular ordering. The first step towards automatic fringe ordering lies in the fringe recognition algorithm.

This is achieved by developing appropriate fringe tracing algorithm. Three fringe tracing algorithms are developed, they are Simple fringe tracing algorithm, Fringe tracing algorithm with directional scan and the complex fringe tracing algorithm. The fringe tracing algorithm performs the task of identifying pixels forming a particular fringe. The basic methodology is, if a fringe point is selected, the algorithm must be in a position to identify all contiguous points forming a fringe. The complex fringe tracing

algorithm has been found to work the best for tracing out the fringe patterns for test images as well as fringes recorded by actual experiments.

Fringe tracing algorithm helps to identify and order complete fringes if the fringe order of one of the points in the fringe is known. To completely order the fringe field, one needs to know the fringe order for one point each, on different fringes. This was made possible by identifying the fringe gradient direction.

The use of intensity information to identify the fringe gradient is established in this thesis. The two dimensional and the three dimensional plots revealed that the intensity variation is not trivial. Further work is needed to fully utilise this data for fringe ordering.

In the present work collection of data from a the circular disk under diametral compression has been automated. This assumes significance since, most laboratories use the circular disk under diametral compression as a model to evaluate the material fringe constant. A semi automatic procedure has been implemented for the mixed mode S.I.F analysis for a crack problem. These were made possible since the nature of the fringe field is known apriori and suitable scan paths were selected for fringe ordering. However, for a general class of problems, identification of suitable scan paths will be a difficult task. It should be stressed that the problem of automation of fringe ordering is very difficult to fit in a standard "if-then-else" type of computer algorithm, and one needs "intelligent program" to solve it. The future work can be in the form of developing an expert system for fringe recognition and ordering.

Fringe ordering is only an intermediate step and one needs methodologies to extract field parameters using the fringe data. The methodology to extract the stress field parameters in the neighborhood of a crack tip from the information of the fringe order

and positional coordinates of various points was implemented and tested for the mode I as well as the mixed mode problems.

The use of equations proposed by Atluri and Kobayashi[2] for evaluating these stress field parameters has been presented. Various typographical errors in the reported equations of Atluri and Kobayashi[2] is corrected in this thesis.

Gear is one of the most important and most widely used machine element. The gear tooth failure commonly occurs due to fracture initiated due to a fatigue crack at the tooth fillet. The gear tooth with a crack has been analysed using photoelasticity. The crack tip stress field in the case of a spur gear presents one of the most complex fringe patterns for the analysis. Apart from the finite geometry of the structure the crack is located in a complex stress gradient zone. A semi automatic methodology for ordering the fringes around the crack tip.

The use of Atluri and Kobayashi's series solution for the evaluation of the fracture parameters was discussed. Convergence of the series solution depends on a number of factors including the choice of the data points, the initial estimates for various parameters and the zone of data collection. Analysis was carried out for addendum side contact of the gear tooth, to find out the optimum number of terms for convergence. The criteria for selection of the data points was also discussed. The results show that, an higher order solution can faithfully model the stress field in this case if appropriate number of terms are used. The success of the analysis of the present example provides enough confidence to apply photoelasticity to evaluate fracture parameters for complex real-life problems. Further work in the form of analysis of the fringe patterns for various gear position to investigate the change in the mode I and mode II parameters over the complete contact length can be taken up for complete analysis.

## APPENDIX-1

### MODIFICATIONS REQUIRED TO CONVERT SOFTWARE FROM PIP TO MVP-AT

One of the major tasks completed in the course of the present investigation is the conversion of various software modules developed around Professional Image Processing ( PIP ) system over the last four years to the newly acquired MVP-AT system. Though, both PIP and MVP-AT were supplied by the same manufacturer, they have not provided appropriate software to convert the programs developed from one system to the another. PIP is basically a monochrome system on the other hand MVP-AT can support colour image processing. In view of the enhanced capabilities of the MVP-AT, even the basic structure of the software has to be modified.

In the following paragraphs, the basic system configuration of PIP and MVP-AT are discussed initially. The command structure necessary to replace the commands of PIP are summarised in the following categories. They are initialisation commands, Input Output commands, Point to Point commands, Graphics commands, Statistical functions and look up table operations. Finally for various software modules, the sequence of quadrants used by it in MVP-AT for intermediate operations is summarised. This information is essential if one writes a software involving these modules to perform various tasks.

#### **A.1. System Configuration**

##### **(i) PIP**

It is a plugin black and white video frame grabber-digitizer board for the IBM-PC which supports the PIP software. This software has libraries for frame buffer I/O, Look Up Table manipulations, graphics and imaging functions. The system has a 1Mb frame buffer on a PC-8088 machine. The computer languages supported by the PIP library are Microsoft-C ( version 4.00 ) and Microsoft FORTRAN (version 3.31).

##### **Description of system parameters :**

###### **1. Frame Buffer :**

An area of PIP memory where related pixel data, which comprises of one pixel frame, is stored. The video RAM of the PIP can be configured in the following manner:

a. 4 X 512 X 512 X 8-bit frame buffers. This configuration is used for a black and white image with the grey values defined by 8 bits for every pixel. (quadrant 0 to 3, x and y coordinates 0 to 511 ).

b. 1 X 1024 X 0124 X 8-bit frame buffer. ( 0 to 1023 )

## (ii) MVP

The MVP-AT hardware can be programmed through the IMAGER-AT software library. The software contains primitives that provide control over the frame buffer IO, Look Up Table, Graphics and the Imaging functions. The system has a 1Mb frame buffer on a PC-386 machine. The computer language directly supported by IMAGER-AT is Microsoft-C (Version 4.00).

## Description of the system parameters :

## 1. Frame Buffer :

The video RAM of the MVP can be configured in the following manner:

- a. 4 X 512 X 512 X 8-bit frame buffers. This configuration is used for a black and white image with the grey values defined by 8 bits for every pixel. ( FB0 to FB3, 0 to 511 each).
- b. 3 X 512 X 512 X 8-bit frame buffers. This configuration is used to store coloured images. RED in FB0, GREEN in FB1, BLUE in FB3. The frame buffer FB2 is not used. ( FB6, 0 to 511 ).
- c. 2 X 512 X 512 X 16-bit frame buffers.( FB5 and FB6,0 to 511 each)
- d. 1 X 1024 X 0124 X 8-bit frame buffer. ( FB7, 0 to 1023 )

## A.2. Modifications necessary to transfer software from PIP to the MVP-AT system.

The PIP software has absolute coordinates referred i.e. (0,0)-(1023,1023). Whereas the MVP-AT system is required to be configured as 4 X 512 X 512 X 8-bit quadrants. Hence the coordinates of a point in any quadrant correspond to the local coordinates i.e. (0,0)-(511,511). as shown in Fig.A.1.

## A.2.1. Initialization commands

## PIP :

```
fg_inifmt(baseaddr,mode,speed,class,vid-type,zoom);
fg_chan(2);
fg_quadm(1);
fg_pan(0);
fg_scroll(0);
fg_zoom(0);
fg_iniluts();
fg_setwin(0,0,511,511);
```

The suffix "fg\_" is required for every PIP library command to distinguish it from the C library commands.

The command "fg\_inifmt" initializes the PIP board to a known state.

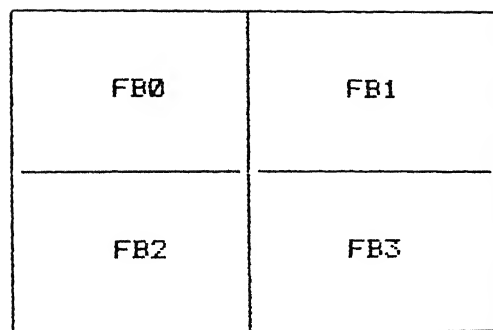


Fig.A.1 shows the quadrant position for the MVP-AT system.

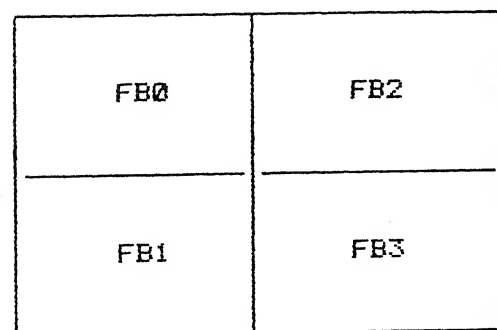


Fig.A.1 shows the quadrant position for the PIP system.

baseaddr : This parameter specifies the offset of the IO address used. Value for the current configuration : 620.

mode : Specifies whether the PIP card is configured to allow for zoom resolution. Value for the current configuration : 1 (allowed).

speed : Clock speed determining the type of PIP board installed. Value for the current configuration : 0 (PIP-1024 installed).

class : Specifies the video format.

Value for the current system configuration : 0 (512 X 512 EUROPEAN).

vidtype : Selection between European or American video format.

Value for the current system configuration : 1 (EUROPEAN).

zoom : Specifies the resolution.

Value for the current system configuration : 0 (full resolution).  
The current settings are : fg\_inifmt(620,1,0,0,1,0);

The command "fg\_chan(chan)" is used to select the input channel.

where "chan" is :

0 : Channel 0, i.e. top camera IP on the PIP card.

1 : Channel 1, i.e. middle camera IP on the PIP card.

2 : Channel 2, i.e. bottom camera IP on the PIP card.

Value for the current system configuration : 2 (bottom card).

The command "fg\_quadm(p)" is used to select the quadrant mode.

where "p" is :

0 : 1024 X 1024 mode.

1 : 512 X 512 X 4 mode.

Value for the current system configuration : 1 (4 quadrants).

The command "fg\_pan(x) and fg\_scroll(y)" is used to set the absolute origin position, where (x,y) is the new screen origin.

Value for the current system configuration : 0,0 (Top-Left corner is the origin).

The command "fg\_zoom(r)" is used to select the zoom resolution.

where "r" is :

0 (std resolution).

1 (compressed image).

The command "fg\_iniluts" loads all look up tables with grey scale maps.

The command "fg\_setwin" specifies the lower left and upper right corners of the working space in all quadrants.

Value for the current system configuration : 0,0,511,511 (full quad).

MVP-AT :

```
if (init(MEMBASE, IOBASE) != OK) {
    exit(INIT_ERR);
}
opmode(PROC, FB0);
```

```
disformat(FREQ20, INTLACE, EUROPEAN);
```

```
outpath(0,-1,0,0);
sync(INTERN, NONE);
video(ENABLE, FBUF);
inmode(MONO);
```

MVF-AT is provided with a file "im2to3.h" which recognizes the MVP library functions and prefixes them with "im\_".

The command "init" initialises the board to a default state. This command must be used at the begining of the program before any calls to the MVP library.

The parameter MEMBASE specifies the 64K memory segment of the board with respect to the PC memory space. The 64K direct access window is located in the lower 1Mb of the PC-386 memory space. This MVP-AT reserved memory is fully supported by the IMAGER-AT library and the IBM DOS. This allows all the MVP frame buffers to be accessable by the bus 64Kb at a time.

The parameter IOBASE specifies location of board in the PC-Bus I/O space.

The command "opmode(mode,quad)" selects the operating mode. Every command in the IMAGER-AT has to be called from its respective operating mode.

There are four opmodes, IO, GRAPH, PROC, CGRAB for input output, graphics routines, imaging procedures and for functions in the continuous grab modes. In the MVP-AT environment, proper opmodes need to be set before any library command is used otherwise the system behaves unpredictably and may even hang.

The PIP system does not have any opmodes and once initialized, the system can perform any operation.

The command "disformat(f,i,t)" customizes the display format.  
where f: frequency, i : interlacing parameter, t : format.  
FREQ20 : Selects the frequency of the pixel clock as 10MHz. (Defined in the header files )  
INTLACE : Selects the interlaced monitor.  
EUROPEAN : Selects the european format.

In PIP this is set by the "fg\_inifmt" command itself.

The command "outpath(backbuf,winbuf,overlaybuf,source)" is used to select the output display quadrant. Where :  
backbuf : It selects the background frame buffer.  
winbuf : The window frame buffer.  
overlaybuf : Overlay source frame buffer. ( Ignored when winbuf negative )  
source : Selects the nibble in overlaybuf. ( Ignored when winbuf negative )

This command besides displaying the working quadrant can thus be used for generating overlays and other window operations.

The command "sync(source)" is used to select the source of the sync signal.

The source has to be changed to "external" when grabbing an image from the camera and changed back when the operation is over. PIP has "fg\_sync(source)" command for the same purpose and works in a similar manner.

PIP command "video(display,source)" is used to select the output of the frame buffers or the camera on the display.  
 display : 1 Enable, 0 Disable.  
 source : 0 Camera, 1 Frame Buffer.

The command "inmode(mode)" is used to select the input data path. The MVP system accepts input from cameras of various video standards including the separate RGB input and the NTSC.  
 MONO: 0 disable, 1 B/W, 2 RGB, 3 NTSC. The PIP does not have such a command as it does not support colour images.

PIP command for changing quadrant :  
`fg_dquad(quad);` This displays the quadrant specified by the "quad".

In MVP-AT one has to use the outpath command.

`outpath(0,-1,0,0);` This selects the quadrant 0 as the display quadrant.

### A.2.2. I/O commands

#### 1. To load the image file from disk to the frame buffer.

PIP :  
`fg_frdisk(bsize,quad,fname,wbuf,seg);`  
 bsize: Intermediate buffer size, required by DOS, common value 4096  
 quad : quadrant.  
 fname: filename string.  
 wbuf : The PIP working buffer address, common value 5200.  
 seg : Portion of work buffer in use, value -1.

MVP-AT :  
`opmode(IO,quad);`  
`fromdisk(fname);`  
 The opmode has to be set to IO in the required quadrant.  
 fname : filename string.

#### 2. To save the image file to the disk.

PIP :  
`fg_todisk(bsize,quad,fname,wbuf,seg);`  
 bsize: Intermediate buffer size, required by DOS, common value 4096  
 quad : quadrant.  
 fname: filename string.  
 wbuf : The PIP working buffer address, common value 5200.  
 seg : Portion of work buffer in use, value -1.

```
MVF-AT :
opmode(10,quad);
todisk(fname);
```

The opmode has to be set to 10 in the required quadrant.  
 fname : filename string.

### 3. Pixel Read/Write :

```
PIP :
fg_pixr(x,y);
fg_pixw(x,y, index);
x , y: They are the x and y coordinates of the pixel to be read from
the frame buffer ( 0 to 1023 ).  

index : It is the intensity value, an integer variable from 0 to 255
```

```
MVP-AT :
opmode(10,quad);
pixr(x,y);
pixw(x,y,pix);
```

x , y: They are the x and y coordinates of the pixel to be read from  
 the frame buffer ( 0 to 511 ).

pix : An unsigned long variable which accepts the value as red byte  
 green byte and last (MSB) blue byte for the colour mode and as the  
 lowest byte/bytes for the other modes.

### 4. Window to/from buffer [array] command.

```
PIP :
fg_winx(wbuf,seg);
fg_winx(wbuf,seg);
```

These commands are used to copy the contents of the current display  
 window to a buffer or from a buffer. These commands are used for  
 storing the window area when it is overlapped by the pop-up window  
 and copying back from the buffer to erase the window.

MVF-AT :  
 These commands are not available in the MVP-AT, however these have  
 been defined in the header file "curutil1.h" as follows.

```
void Winr(int x1,int y1,int x2,int y2)
{ int i1,t,p1;
  opmode(10,quad);
  t=0;
  for(i=y1;i<= y2;i++){
    rowr(x1,i1,abs(x2-x1),atemp);
    for( p1=0; p1 <= abs(x2-x1);++p1){
      abuf[t][p1]=atemp[p1];
    }
    t +=1; }
```

```
void Winw(int xi,int y1,int x2,int y2)
{
```

```

int i1 , t , p1;
opemode(10,quad);
t=0;

for(i1= y1;i1<= y2;i1++){
    for(p1=0; p1 <= abs(x2-x1);++p1){
        atemp[p1]=abuf[t][p1];
        t +=1;
        roww(x1,i1,(x2-x1),atemp);
    }
}

```

where "abuf" is an array of long unsigned 250 X 250 elements, the largest array size supported by the compiler and atemp is array of unsigned long of 250 elements. It can be seen that this will be able to operate with a window size of 250 X 250 of the 512 X 512 quadrant space.

However the MVP-AT provides a much more efficient command for generating the pop-up menu and such other functions.

This can be done by using the "drawmode" command. It sets the pixel replacement policy for the subsequent graphics commands.

```

opemode(GRAPH,quad);
drawmode(2);

```

This then XOR's the pixel locations to be overwritten with the new values, displays the image when the back ground has to be restored, it again XOR writes the pixel locations, erasing the current window. This is a standard practice used for generating fast displays and animations.

PIP also has a quadrant to quadrant window copy command.

In MVP-AT one has to use the command "pixblt" to achieve an equivalence of "cpws". "cpws" is used in various software modules repeatedly. The identification of pixblt to do this operation took considerable time as there is no semblance of comparison between the command names. This command can thus be used directly in place of "cpws(quadi,quad2)" the copy workspace command in PIP, quadi is the source quadrant and quad2 is the destination quadrant.

```

opemode(PROC,quad);
pixblt(sbuf,x1,y1,x2,y2,dbuf,x3,y3,sdir,ddir);
sbuf , dbuf : Source and destination quadrants.
(x1,y1) , (x2,y2) : Source window coordinates.

```

(x3,y3) : Target window starting coordinates.  
sdir , ddir : Source and destination scan direction. Values 0,1.  
Selecting different source and destination scan directions can enable quick rotation of the image through 90, 180, 270 degrees.

#### A.2.3. Point to point commands

## 5. Logical operators for the image :

PIP :

It does not have any direct logical operators and the corresponding pixels have to be read from the two quadrants and then operated upon using the functions in Microsoft-C.

e.g. If two windows have to be logically ANDed then following function is required :

```
for (i=winxy[0];i<winxy[2]+1;++i) {
    for (j=winxy[1];j<winxy[3]+1;++j) {
        c1=fg_pixr(512+i,j);
        c2=fg_pixr(512+i,512+j);
        if ((c1 != 0) && (c2 != 0))
            fg_pixw(i,j,250);
    }
}
```

This is replaced by a single command in the MVP-AT system.

The "interimage" command performs specified operations between two images.

opmode(PROC,quad);

interimage(sbuf1,sbuf2,dbuf,fn);

sbuf1, sbuf2 : The source frame buffers.

dbuf : The frame buffer in which the resultant image is to be stored

fn : Specifies the logical operation to be performed.

0 : ADD

1 : SUB

2 : MIN

3 : MAX

6 : AND

7 : XOR

8 : OR

This command is very fast and operates at 1/4 the real time rate.

## A.2.4. Graphics commands

### 6. Text output on the screen.

PIP :

fg\_text(string,size);

fg\_tchar(char,size);

string : The text to be output is stored in this string.

size : Specifies the size on the screen.

char : A single character.

Writes the string using the current drawing index at the current pen location. e.g.

```
void frn_func()
{
```

```

int i;
char c;
    for (i=0;i<3;++i)
        frn_buf[i]=0;
    fg_setind(255);
    fg_rectf(0+qd2.x, 491+qd2.y, 182+qd2.x, 511+qd2.y);

    fg_setind(0);
    fg_moveto(2+qd2.x, 510+qd2.y);
    fg_text("FRINGE:",2);
    i=0;
    do {
        c=getch();
        if ( ((c>='0' && c<='9') || (c=='.')) &&
            i < 3) {
            frn_buf[i]=c;
            fg_tchar(c,2); /* This function directly
outputs the number as a character */
            i++;
        }
    } while (c!=crlf && i< 3);
    frn_flag =0;
    fflush(stdin);
}

```

This function is used to print FRINGE on the screen, then read the fringe value, display it on the screen and erase it when comming out of the loop.

**MVP-AT :**  
opmode(GRAPH,quad);  
gtext(size,cnt,string);  
size : 1 Normal, 2 Large.  
cnt : Number of bytes to be output.  
string : The text string to be output.  
The character size in case of the MVP-AT is different than the character size in PIP. This command also needs the number of bytes in the string, this therefore requires predetermined maximum size of the character array to be output. e.g.

```

void frn_func()
{
int i,c1;
char c,frn_temp[10];
    for (i=0;i<3;++i) frn_buf[i]=0;
    opmode(GRAPH,0);
    drawmode(2);
    move(10,440 );
    gtext(1,7,"FRINGE ");

    i=0;
    do {
        c=getch();
        c1=toascii(c);
        if ( ((c>='0' && c<='9') || (c=='.')) && i < 3)
    {
        frn_buf[i]=c1;
    }
    }
}

```

```

/* Since tchar function is not available following operations
have to be performed : */
    gcvt((c1-48),2,frn_temp);
/* This function is used to convert the integer variable to a string
array whose max size is 3 bytes */
    gtext(1,3,frn_temp);
/* Then this string is displayed */
    i++;
}

} while (c!=crlf && i< 3);
move(10,440 );
gtext(1,7,"FRINGE ");
gtext(1,3,frn_temp);
drawmode(0);
frn_flag =0;
fflush(stdin);
}

```

#### A.2.5. Statistical functions and look up table operations

The contrast stretching procedure :

PIP :

from the interpreter :

```

average 0 0 /* SPATIAL AVERAGING */
histo 5200 /* HISTOGRAM */
dq 1
setindex 0
cl 0 7
setindex 255
dhisto %1 10 962 400 255 255 5200 /* Draw the histogram */
pause
dq 0
modhist 0 %1 %2 0 5200 5200 /* Modify the histogram to new range */
*/
dq 0
map 0 0 5200 /* Use that histogram function to map the pixel to new
intensity values */

```

MVP-AT :

from the interpreter :

```

opmode 2 0
outpath 0 -1 0 0

scaling 20 0 200 255 200
/* This command recomputes the intensity vaules between 20 to 200
and maps then as 0 to 255 linearly. Thus we "stretch" the intensity
range to the zone of interest only. The inormation contained in
pixels having intensity values upto 20 and beyond 200 is ignored. */

cwb 200 200 -1 15
/* This command is used to convert the newly computed values in the
required format. */

```

```
/* these two commands are repeated with different intensity limits
   depending upon the individual image */

olutJav 0 200 200 200 0 0 0
/* This command actually maps the intensity values of all the pixels
on the screen to the new range */
```

### A.3. Information stored in different quadrants for various functions / software modules.

1. window\_cursor(); /\* Used to select the working window space  
Source file : curutil.h \*/

Input : Original image in quad 0.

Steps :  
1. Copy original image to quad 2.

2. Select window and show the clipped part in quad 0.  
3. If it is not satisfactory then copy original image  
from quad 2 to quad 0 and repeat.

Output : 1. The window portion of the image in quad 0.  
2. Original image quad 2.

2. global\_threshold(); /\* Used for thresholding the image.  
Source file : thresh.h \*/

Input : Original image in quad 0.

Steps :  
1. Copy original image to quad 1.  
2. Threshold the image in quad 0.  
3. If it is not satisfactory then copy original image  
from quad 1 to quad 0 and repeat.

Output : 1. The thresholded image in quad 0.  
2. Original image quad 1.

3. hybrid\_thin(); /\* For fringe skeleton extraction.  
Source file : ortho1.h. \*/

Input : Thresholded image in quad 0 and Original image in quad 1.

Steps : 1. Row Scan : Scan the image rowwise from quad 0 and write  
the output to quad 2.  
  
2. Col Scan : Scan the image columnwise from quad 0 and  
write the output to quad 2.  
  
3. Diag\_down\_thin : Scan the image at 135 deg. from quad 0  
and write the output to quad 3.

4. Drag\_up\_thin : Scan the image at 45 deg. from quad 0 and write the output to quad 3.
5. AND quadrants 2 and 3 and write the output to quad 2.
6. OR quadrants 2 and 1 and write the output to quad 0.

**Output :** Original image in quad 1 and fringe skeleton superimposed on the original image in quadrant 0.

#### PROGRAM CALIB1.C

**Steps :** 1. Load the image in quad 0.

2. Window\_cursor();
 

**Input :** Original image in quad 0.  
**Output :** 1. The window portion of the image in quad 0.
3. Global\_threshold();
 

**Input :** Original image in quad 0.  
**Output :** 1. The thresholded image in quad 0.  
 2. Original image quad 1( window ).
4. cpws(2,1); /\* copy quad 2 to 1 \*/
5. hybrid\_thin();
 

**Input :** Thresholded image in quad 0 and Original image in quad 1.  
**Output :** Original image in quad 1 and fringe skeleton superimposed on the original image in quadrant 0.

#### PROGRAM TILE :

1. Load the image in quad 0 and save to disk as skn.img.
2. Load skn.img from disk in quad 0.
3. Window\_cursor();
 

**Input :** Original image in quad 0.  
**Output :** 1. The window portion of the image in quad 0.  
 2. Original image quad 2.
4. Global\_threshold();
 

**Input :** Original image in quad 0.  
**Output :** 1. The thresholded image in quad 0.  
 2. Original image quad 1( window ).
5. cpws(2,1); /\* copy quad 2 to 1 \*/
6. hybrid\_thin();
 

**Input :** Thresholded image in quad 0 and Original image in quad 1.  
**Output :** Original image in quad 1 and fringe skeleton superimposed on the original image in quadrant 0.

7. If satisfactory then save to disk as skn.img otherwise repeat from step 2.

Note on converting an image from the TIF to the MVP-AT format :

After converting the image, it is necessary to set the window size by the iowin command before loading the image in the MVP-AT (Flat) format.

## ZOOM FUNCTION

The image obtained from the CCD camera is 512 X 512 pixels in size. Zooming function is implemented in the present work to highlight the zone of importance at the expence of the other area.

1. The image is loaded in quadrant zero and a window is selected to mark the portion of the image to be zoomed.

2. The user is asked to input the factor by which the image has to be zoomed. This factor has to be selected depending on the window size. If the size of the zoomed window exceeds the quadrant dimensions ( 512 X 512 ) then the image gets distorted.

3. The pixels are then read rowwise and corresponding to each pixel, n X n pixels having the same intensity value are drawn in quadrant 1.

4. The coordinate values are then advanced by the factor n. This continues till all the rows are scanned.

Depending on the mask selected the image portion can be zoomed by any factor or repeated zooming operations can be performed on the image to have a high magnification. The factor of magnification can be independent along each axis. However a different factor along x and y results in distortion of the picture.

This function is particularly useful in debugging the automatic fringe tracing algorithms. Note that the image contains no new information, it only shows a visual magnification by the factor.

## APPENDIX-3

Least square output file.

Convergence Error : 0.11000000

set#	itrns	parameter values			
1	1	4.820687	-0.637504	0.184755	0.051670
		-0.080121	0.011736	-0.131800	0.011350
		-0.029168	-0.017154	0.004268	
2	1	4.849699	-0.621264	0.152001	0.050772
		-0.078510	0.011293	-0.131517	0.011323
		-0.029386	-0.016845	0.003889	
3	1	4.843923	-0.620714	0.143154	0.051264
		-0.078678	0.011212	-0.133837	0.013461
		-0.032331	-0.016353	0.003672	
4	1	4.846506	-0.618379	0.135602	0.051343
		-0.078545	0.011131	-0.134098	0.013818
		-0.032861	-0.016220	0.003569	
5	1	4.846382	-0.617720	0.132626	0.051415
		-0.078525	0.011099	-0.134505	0.014208
		-0.033399	-0.016120	0.003516	
6	1	4.846701	-0.617242	0.130846	0.051447
		-0.078504	0.011080	-0.134632	0.014347
		-0.033598	-0.016078	0.003489	

Average Values \_\_\_\_\_

```
par[1] = 4.842316
par[2] = -0.622137
par[3] = 0.146497
```

par[4] = 0.051318

par[5] = -0.078814

par[6] = 0.011258

par[7] = -0.133400

par[8] = 0.000000

par[9] = 0.013085

par[10] = -0.031791

par[11] = -0.016462

par[12] = 0.003734

#### E R R O R   T A B L E

x	y	N_data	N_cal	% error
-0.58	0.68	2.00	1.90	5.23
-0.64	0.98	2.00	1.93	3.69
-0.52	1.35	2.00	2.01	-0.26
-0.21	1.56	2.00	2.06	-2.75
0.44	1.63	2.00	1.97	1.54
0.76	1.32	2.00	1.97	1.71
0.84	0.91	2.00	2.01	-0.67
0.81	0.72	2.00	2.03	-1.69
0.74	0.52	2.00	2.03	-1.65
0.68	0.41	2.00	2.01	-0.58
0.51	0.24	2.00	2.04	-2.21
0.36	0.32	3.00	3.02	-0.72
0.40	0.53	3.00	3.03	-0.85
0.35	0.71	3.00	3.03	-0.95
0.27	0.84	3.00	2.99	0.21
0.04	0.91	3.00	2.98	0.59
-0.12	0.82	3.00	3.01	-0.34
-0.23	0.62	3.00	3.02	-0.67
-0.23	0.54	3.00	3.06	-1.96
0.03	0.47	4.00	4.05	-1.22
0.20	0.43	4.00	3.89	2.86

-0.75	-0.60	1.00	1.18	-18.37
-0.84	-0.84	1.00	1.23	-23.23
-0.93	-0.99	1.00	1.14	-14.44
-1.10	-1.24	1.00	0.90	9.55
-0.53	-0.69	2.00	1.92	4.12
-0.55	-1.07	2.00	1.94	3.15
-0.48	-1.37	2.00	1.97	1.31
-0.40	-1.70	2.00	1.98	1.00
-0.28	-1.97	2.00	2.05	-2.72
-0.29	-2.25	2.00	2.01	-0.75
-0.47	-2.86	2.00	1.97	1.64
-0.83	-3.31	2.00	2.02	-0.89
1.99	-1.92	2.00	1.95	2.57
1.59	-1.60	2.00	2.03	-1.28
1.34	-1.30	2.00	2.06	-2.82
1.12	-0.87	2.00	1.95	2.49
0.95	-0.70	2.00	2.00	-0.07
0.73	-0.48	2.00	2.05	-2.60
0.64	-0.35	2.00	1.94	2.78
0.46	-0.41	3.00	2.71	9.70
0.51	-0.59	3.00	2.81	6.37
0.55	-0.87	3.00	2.83	5.53
0.31	-1.16	3.00	2.93	2.48
0.03	-1.13	3.00	2.87	4.17
-0.12	-0.97	3.00	2.88	4.01
-0.21	-0.87	3.00	2.81	6.21
-0.25	-0.67	3.00	2.89	3.69
-0.02	-0.59	4.00	3.68	8.03
0.20	-0.60	4.00	3.60	9.90
0.26	-0.43	4.00	3.64	9.09
0.66	-0.18	1.00	1.33	-32.93
0.91	-0.29	1.00	1.31	-30.63
1.39	-0.51	1.00	1.18	-18.47
1.73	-0.72	1.00	1.15	-14.92
2.09	-0.97	1.00	1.12	-11.52

1.02	-0.01	1.00	0.89	10.74
0.71	-0.03	1.00	0.98	2.07
0.85	0.23	1.00	1.31	-30.64
0.74	0.17	1.00	1.29	-28.62
1.20	0.38	1.00	1.15	-15.42
1.45	0.55	1.00	1.07	-7.38
1.66	0.75	1.00	0.98	1.88
4.00	-1.78	1.00	0.97	3.15
4.02	-1.27	1.00	0.76	23.72
4.02	-0.91	1.00	0.72	27.66
1.76	-0.74	1.00	1.14	-14.29
2.12	-0.98	1.00	1.11	-10.84
2.71	-1.30	1.00	1.00	0.40
3.06	-1.55	1.00	1.00	-0.19
3.47	-1.72	1.00	0.98	2.15
2.91	-2.53	2.00	1.86	6.78

The absolute average % error = 6.83

## REFERENCES

1. K. Ramesh and B. R. Pramod, "Digital Image Processing of Fringe Patterns in Photomechanics", Opt. Engg. Vol. 31 (7), pp. 1487-1498, (1992).
2. S.N.Atluri, and A.S.Kobayashi, Mechanical Response of Materials, in Handbook on Experimental Mechanics, (Ed.) A.S. Kobayashi, Prentice-Hall, Inc., 1987 , pp. 1-37.
3. R.J.Sanford, "Application of least square method to Photoelastic Analysis", Expt. Mech., Vol 11, 1979 , pp. 621-633.
4. K.Ramesh, "Comparative performance of image processing algorithms in Photomechanics". Proceedings of VII international conference on Experimental Mechanics, Las Vegas. June 8-11, pp 713-718, 1992.
5. R. K. Müller and L. R. Saackel, "Complete automatic analysis of Photoelastic fringes," Expt. Mech. 19, 245-252 (1979).
6. Y. Seguchi, T. Tomita and M. Watanabe,"Computer aided fringe pattern analyser - A case of photoelastic fringe," Expt. Mech. 19, 362-370 (1979).
7. T. Y. Chen and C. E. Taylor, "Computerised fringe analysis in photomechanics," Expt. Mech. 29, 323-329 (1989).
8. T. Yatagai, S. Nakadate, M. Idesawa and H. Saito, "Automatic fringe analysis using digital image processing techniques," Opt. Engg. 21, 432-435 (1982).
9. A. C. Gillies,"Image processing approach to fringe patterns," Opt.Engg. 27(10), 861-866 (1988).
10. E. Umezaki, T. Tamaki and S. Takahashi, "Automatic Stress Analysis of Photoelastic Experiment by Use of Image Processing and Numerical Analysis", Proc. of VI Int. Conf. on Exp. Mech.,Oregon, USA, pp 1227-1232, June 6-10 (1988).
11. K. Ramesh, V. R. Ganesan and S. K. Mullick, "Digital image processing of photoelastic fringes - A new approach," Experimental Techniques, 15, 5, 41-46 (1991).
12. K.Ramesh and Rajeev.K.Singh, "Comparative Performance evaluation of various fringe thinning Algorithms in Photomechanics". Technical report: IITK / ME / SMD -93028.
13. A. J. Durelli and A. Shukla, "Identification of Isochromatic Fringes", Experimental Mechanics ,pp 111-118, (March 1983).
14. G.Fredric, "Calibration of equidensity lines", Strain, pp 142-143, Oct 1976.
15. G.R. Irwin., "Discussion of paper by A . Wells and D. Post., The Dynamic Stress Distribution Surrounding a running Crack - A Photoelastic Analysis" Proc. of SESA, Vol.16(1), 1958 , pp. 93-95.

16. H.M.Westergaard, "Bearing Pressures and Cracks", J. Applied Mechanics, June 1939, pp. 449-453.
17. G.R.Irwin, "Analysis of stress and strains near the end of a crack traversing a plate." J. Applied Mechanics, Sept. 1957, pp.361-364.
18. A.A.Wells, and D.Post, "The Dynamic stress distribution surrounding a running crack - A photoelastic analysis," SESA proceedings, Vol. XVI no. 1 1958, pp. 69-92.
19. G.C.Sih, "On the Westergaard method of crack analysis," Int. J. Fract. Mech., 2, 1966 , pp. 628-631.
20. J.Eftis, and H.Liebowitz, "On the modified Westergaard equations for certain crack problems." Int. J. Fract. Mech., 8, 1972, pp. 383-391.
21. H.Tada, P.Paris, and G.Irwin, The stress analysis of cracks handbook, p 1.27, Del Research Corporation, Hellertown, PA, 1973.
22. R.J.Sanford, "A critical re-examination of the Westergaard method for solving opening mode crack problems," Mech. Research communication, 6(5), 1979 , pp. 189-294.
23. W.B.Bradley, and A.S.Kobayashi, "An investigation of propagating cracks by dynamic photoelasticity,"EXPERIMENTAL MECHANICS, Vol.10(3), 1970, pp. 106-113.
24. J.M.Etheridge, and J.W.Dally, "A critial review of methods for determining stress-intensity factors from isochromatic fringes," EXPERIMENTAL MECHANICS.,Vol. 17, 1977 , pp. 248-254.
25. K.Ramesh, and B.R.Pramod, "Automated Evaluation of stress intensity factors by photoelasticity," Proc. of ICSTAD, Tata McGraw Hill, DELHI, 1990 , pp. 1203-1208.
26. K.Ramesh, "Experimental determination of stress intensity factors in isotropic model materials by the technique of photoelasticity," ARDB Report No.: ARDB-STR-TR-91-540-02, 1991.
27. R.J.Sanford, and J.W.Dally, "A general method for determining mixed mode stress intensity factors," Eng. Fract. Mech., 4,1972, pp. 357-366.
28. M.A.Schroedl, and C.W.Smith, " A study of near and far field effects in photoelastic stress intensity determination,' Eng. Fract. Mech., 7, 1975 , pp. 341-355.
29. A.J.Rosakis, and K.Ravi-Chandar, "On crack tip stress state : An Experimental evaluation of three dimensional effects," Int. J. Solids and Structure, 22(2), 1986 , pp. 121-134.
30. R.Chona, G.R.Irwin, and R.J.Sanford, "Influence of specimen size and shape on the singularity dominated zone",ASTM STP 791,1983,pp.I.3-I.23.

31. P.S.Theocaris, and J.G.Michopoulos, "A closed form solution of a slant crack under biaxial loading", Engg. Fract. Mech., V17, 1983, pp.97-123.
32. R.Chona, and R.J.Sanford, "Analysing crack-tip isochromatic fringe patterns", Proc. of VI International conference in Experimental Mechanics., 1988, pp 751-760.
33. H.Honda, and J.C.Conway, " An analysis by finite element techniques of the effects of a crack in the Gear Tooth Fillet and its Applicability to Evaluationsg Strength of Flawed Gears", Bulletin of JSME, Vol 22, No 174, Dec 1979, pp 1848-1855.
34. V.Pankhawala, "Experimental and Numerical investigation of high stress Gradient problems with an emphasis on contact stress analysis", M.Tech Thesis, IIT Kanpur, Nov 1991.